The copyright of this thesis rests with the University of Cape Town. No quotation from it or information derived from it is to be published without full acknowledgement of the source. The thesis is to be used for private study or non-commercial research purposes only.

University of Cape Town

Hall Effect in Printed Nanoparticulate Silicon Networks

Girma Goro Gonfa

University Of Cape Town

Thesis Presented for the Degree of
DOCTOR OF PHILOSOPHY
in the Department of Physics
UNIVERSITY OF CAPE TOWN

February 2010

Abstract

Silicon nanoparticles for the application of printed electronics were successfully synthesised and characterised. High energy milling has been proven to yield uncontaminated powder of median particle size 150 nm satisfying a lognormal distribution. Single crystalline P- and N-type silicon wafers, and metallurgical grade silicon were used as starting materials. The structural characterisation of all milled powders using X-ray diffraction (XRD), Small Angle X-ray Scattering (SAXS) and electron diffraction proved that the silicon nanoparticles are polycrystalline with a crystallite size of about 40 nm.

For the first time, we have formulated printable semiconducting inks from nanoparticulate silicon. Silicon nanoparticles were mixed with organic binders, such as linseed oil and acrylic, to produce printable inks. Similarly nanoparticulate silicon ink, doped with inorganic salts, which is a different procedure to conventional impurity doping of the silicon structure, was produced with linseed oil. A home-built Hall measurement system was used to characterise layers of doped ink, for which a complete carrier type reversal was observed. Based on the result of elemental mapping, two possible models were suggested to explain the doping effect.

A state-of-the-art Hall measurement system was used to perform field dependent analysis of screen printed silicon inks in van der Pauw geometry. A magnetoconductivity tensor model was developed to extract the carrier properties. All the layers were demonstrated to have at least two carrier types. Inks produced from P-type silicon maintained their carrier type, but reversal was observed for the N-type layers. The mobility of the carriers is better or comparable to similar classes of semiconducting materials.

University of Cape Town

More information on the interparticle connections were obtained from IV and impedance spectroscopy measurements which demonstrated the capacitive effects present in the printed layers. The capacitors originate at the interfaces between the metal and the layers and between the particles.

University Of Cape Town

"Ati kana waan gooteef, ani yeroo hundumaa galateeffachaa sin jajadha, namoota siif of kennan durattis maqaa kee isaa gaarii abdii dhaan nan waammadha."

Far. 52:9

"I will praise you forever for what you have done; in your name I will hope, for your name is good. I will praise you in the presence of your saints."

Psalms:52:9

Acknowledgements

First of all I thank the Almighty God for everything He has done in my life. I would like to take this opportunity to thank Prof. D.T. Britton and Prof. M. Härting for their guidance and assistance throughout this work. It was an opportunity and privilege to be supervised by them. Thanks for all the opportunities you have given me to visit world class laboratories such as the Brazilian Synchrotron Facility at Campinas, Brazil and The Advanced Light Source, Berkeley Labs, USA. I am also thankful for your generous support of my trip to local and international conferences.

The encouragement and friendship from fellow compatriot students at UCT was so great. I thank Abiy Getachew, a student converted friend, Kende Mekonnen (was student at my institute when I was lecturing, but will never admit that I was his instructor), Kamil Hussein, Solomon Sertse, our first year was uniquely memorable. My thanks also extend to Nebiha Bedru, Minilik and Kaleb Nigussie, Betsegaw Taddese, Fasil Nigussie, Dawit Worku for the constructive advices and support you have been providing me. I thank my friends, Dr. Tesfaye Taddese (UWC), Dr. Yoseph Assefa. Dr. Getachew Abebe, Dr. Abi Taddese, Dr. Idris Ahmed, Dr. Hussein Hamda, Dr. Jema Haji, Dr. Sylvain Halindintwali (UWC) who were always there for me when ever I knocked at their door. Dr. Kittessa Roro, thank you for your support and encouragement throughout my work. My thanks

University Of Cape Town

goes to Efrem Kebede and Prof. Francis D. Berhanu for their friendship and useful tips about South Africa. During my short visit to Bloemfontein, I enjoyed the hospitality of my friends Dr. Namara Galata, Dr. Yali Edessa, Dr. Zerihun Gudeta, Dr. Amha Kebede and Dr. Kinde Tesfaye, thanks folks you made my brief stay pleasant.

My brother Asfaw Goro is a wonderful man, whom I trusted so much. I always call him like a small boy and order to do this and that. He never let me down and never complained. I always thank God about you, it is a blessing to have a humble brother like you, thank you for everything. I wish you a happy life you have started with Kiya. All my siblings are extremely good to me and to my family. My elder brother Shiferaw Goro is like a father looking after and supporting my family. I salute you both, Shiferaw and Belaynesh, for all you have done for me from my school age to now. Dear Chief (Shiferaw), I know the sacrifices you made to shape the future of your juniors. Because of you, we became who we are today and the credit is all yours. Sisay Goro and family, thank you guys for all the support. My dear sister Birke Goro, I thank you for your love and encouragement. Your "cuukkoo" was never forgettable. It was always in my emergency stock and kept me going when ever I felt lazy to cook.

Waaqayyo guddaan Umrii keessan dheeressee badhaadhina kana akka waliin agarru fedha isaa waan ta'eef ulfinniif galatni bara baraan Isaaf haa ta'u. Eebbi keessan utubaa naaf ta'e gargaarsa Waaqayyoo wajjin sadarkaa kana gaheera, egaa ani gammadee isinis gammadaa. Malqaa hamma dargaggummaatti qarqaarsaa naaf gootaniif hunda kanin isin galateeffadhu abbaa koo Obbo Gooroo Gonfaa Boonsaa, Aadde Araggaash Dabalaa Waaqjiraa, Aadde Shaashii, Obbolaawwan koo Obbo Istadaaruu Gooroo, Aadde Adaanuu Gooroo, Obbo Dajanee Tsaggayee, hunda-isaanii maatii isaanii waliini. Abbaan koo ilaalchi fi kabajni ati baruumsaaf qabdu, firoottan kanneeniif fakkeenya guddaa kan ta'uudha.

I would like to thank Almaz Geremew, Ashenafi Gutema, Taddelech Taddese, Tigist, Samuel, Musie and Kenna Ashenafi, for your hospitality and generosity during my visit to the US. You are my dearest and supportive family through the years back from the time of my undergraduate studies. Taddu, thanks for the tuxedo. Tigist thanks for the dinner at Maaza Restaurant and the entertaining

University of Cape Town

evening. My little niece Kenna you are so sweet, your uncle GG loves you so much.

Dear daddy (my father-in-law Eng. Makonnen Rumicho), I know my name is in your daily prayer list. You are more than a father to me. I have no word to thank you for you have been always there for me and my family. Your encouraging emails and text messages were vital to keep me going. Solomon Tekalign with family and Martha with family, I thank you for your prayer and support to my family. With out you folks it would be difficult for my family to be there for such long time. Because of people of God I was always in peace. May the heavenly father bless you all abundantly.

Dr. S. Nsengyumva, Dr. S. Wyngaardt, Dr. E. Minani, Ayodele Odo, N. Mathe, B. Magunje, Wole Solana, E. Jonah, Sara Abbas, Hind Ahmed, D. Unuigbe, S. Walton, S. Jones, M. Scriba, T. Ntsoane, you have been wonderful friends and colleagues. Thank you so much for all the assistance and your contribution during our formal and informal discussion sessions. My special thanks to Prof. D. Knoesen of UWC, for his door was always open for me. I appreciate the time you spent to assist me during my visits and for your inspirational words. I would like to thank the academic and administrative staff of the Physics Department (UCT) for their help and willingness to help.

My home-base institution Haramaya University (HU) deserves to be thanked for giving me the opportunity to pursue my study. My thanks go to Prof. Belay Kassa, President of Haramaya University, for his continuous assistance, from the very start to now. Dr. Brook Lemma, then my boss and colleague, who in person flew with my application forms to the Ministry of Education to beat the deadline, otherwise this would not be possible. Thank you so much. Dr. Tena Alamirew, Dr. Belayneh Leggese, Dr. Tesfahun Kebede, Dr. Fikadu Lemessa , thanks for all your assistance and understanding. My guarantor, Admasu Bogale, deserves

University of Cape Town

thanks for he trusted me. All colleagues and friends, whose name is not mentioned unintentionally, thank you all for you were always supportive and ready for any help I demanded from you.

The financial support from Haramaya University, ANSTI-UNU, PGFO-UCT, DST-Innovation Fund (South Africa) is duly acknowledged.

Last but definitely not least, my wife Meti Mekonnen, you are so special to me. Your encouragement and love kept me going. If it was not for your consistent encouragement, it would be more difficult to be at this stage. I know how difficult it was to be alone and taking care of all the responsibility of the family. But you are strong. Thank you for always you were beside me and supportive. You were like a shock absorber; just take all the suffering to keep me comfortable. It was beyond dedication, my debt to you is beyond measure. With the help of God now is time to reunite and once again restore our happy family life. My kids, Jalanne Girma and Nuhili Girma, you are my Angels, thank you for the understanding and love. You were so considerate who never complained about your limited supplies. Thank you for taking care of your mom and being such sweet kids. You are the best daughters one ever wishes to have and I always thank God for that.

“When I called, you answered me.........” Psalms: 138:3

University of Cape Town

Contents

Abstract 1

Acknowledgements 3

Chapter 1 Introduction 11

Chapter 2 Physics of Semiconductors 13

2.1 Classification of materials 13

2.2 Silicon and its properties 17

2.2.1 Crystalline silicon 18

2.2.2 The band structure for crystalline silicon 18

2.2.3 Density of states, statistics of charge carriers 20

2.2.4 Amorphous silicon 26

2.2.5 Nanocrystalline silicon 28

2.3 Doping 29

2.3.1 Introduction 29

2.3.2 N-type semiconductor 31

2.3.3 P-type semiconductor 33

2.3.4 Compensated semiconductors 34

2.4 The PN junction 36

Chapter 3 Carrier Transport and the Hall Effect 42

3.1 Electrical conductivity in crystalline semiconductors 42

3.2 Electrical conductivity in non-crystalline semiconductors 45

3.3 The Hall Effect 50

3.3.1 Description of the Hall effect 51

3.3.2 Factors affecting the Hall measurement 55

3.3.3 Resistivity measurements in van der Pauw geometry…………………………………………… 66

3.3.4 Hall effect measurement in van der Pauw geometry…………………………………………… 69

3.4 Multi carriers and the magnetoconductivity tensor 70

3.5 Hall effect in disordered systems 78

University of Cape Town

3.6 Hall effect in polycrystalline materials 79
3.7 Hall effect in a particle network 82
3.8 Hall effect in composite system 83
3.9 Impedance spectroscopy 84

Chapter 4 Powder and Layer Production 89
4.1 Powder and layer production 89
4.2 Printing methods 95
4.2.1 Hand printing 95
4.2.2 Screen printing 97
4.3 Ink Properties 99
4.3.1 Rheological properties of ink 99
4.3.2 Requirements for hand printing 101
4.3.3 Requirement for screen printing 101
4.4 Ink formulation and mixing 102
4.4.1 Oil based inks for manual printing 103
4.4.2 Acrylic inks for screen printing 103
4.5 Printing procedures 104
4.5.1 Manual printing 104
4.5.2 Screen printing 105
4.6 Sample production and description 106
Chapter 5 Experimental Techniques 112
5.1 X-ray diffraction 112
5.2 Small angle X-ray scattering (SAXS) 115
5.2.1 Scattering theory 115
5.2.2 Scattering from fractal structures 118
5.2.3 Beaucage's global scattering function 119
5.2.4 SAXS experiment 120
5.3 Scanning electron microscopy (SEM) 123
5.4 Transmission electron microscope (TEM) 125

University of Cape Town

5.5 Raman spectroscopy 126
5.6 Electrical measurements 130
5.6.1 The software 131
5.6.2 The IV measurement 133
5.6.3 Home-built Hall measurement system 136
5.7 Impedance analysis 138
Chapter 6 Results 139
6.1 Powder characterization 139
6.1.1 X-ray diffraction 139
6.1.2 Transmission electron microscopy 142
6.1.3 Raman spectroscopy 146
6.1.3.1 Zirconia ball milled silicon powder 147
6.1.3.2 Steel ball milled silicon powder 149
6.1.3.3 High energy milled powder 150
6.2 Layer structural characterization 151
6.2.1 Scanning electron microscopy 151
6.2.2 Result from SAXS 152
6.3 Preliminary electrical characterization of silver ink 160
6.4 Hand printed oil based inks 164
6.4.1 Hall effect studies of hand printed layers 165
6.4.2 Layers in hetero- and sandwich structures 171
6.4.3 Impedance measurement 173
6.5 Field dependent characterization of bulk material and powders 177
6.5.1 Test of model – InAs 177
6.5.2 Wafers and metal grade silicon 180
6.5.3 Compressed powders 184
6.6 Field dependent studies of screen printed layers 185
Chapter 7 Discussion 187
Chapter 8 Conclusion 197

University of Cape Town

References 199
Appendices 211

University Of Cape Town

1 Introduction

The advances made in semiconductor technology during the past sixty years have changed the lifestyle of modern society. In this regard silicon has been, and continues to be, the most important material. The application of silicon in device form ranges from simple hand held consumer electronics to highly sophisticated space technology. The demand for cleaner and sustainable energy source has driven the innovation of silicon for photovoltaic applications. Silicon is widely used in its different phases: as crystalline, amorphous and nanocrystalline material. This thesis will present new class of semiconductor material, based on nanostructured silicon, with new techniques for device production which address issues of cost and scalability.

Materials with structural elements such as crystallites, particles or clusters with dimensions of the order of 100 nm or less are classified as nanostructured materials. Recently nanostructured materials have received much attention because of their unique electrical and optical properties. Their application areas are diverse, including solar energy, sensors, and electronics [1-3]. To this end nanoparticulate silicon was produced applying high energy milling of bulk silicon. This is a cheap and simple method of synthesis of large quantities of material with a potential for wide areas of application such as solar cells and display switch transistors [4, 5]. Nanoparticulate silicon powder was used to produce inks using organic binders such as linseed oil and acrylic. Although printing is an economically viable and easy technique for complete device fabrication, this thesis focuses on the electrical and structural properties of the printed layer as a nanoparticulate silicon composite.

The thesis is divided into eight chapters, with this first chapter introducing the thesis. The second chapter focuses on the general physics of semiconductors,

University of Cape Town

and particularly silicon as the material of interest. Its properties when it occurs in different structural phases are discussed.

Chapter three gives an overview of the transport properties of semiconductors with a focus on the Hall effect. Carrier transport theory is presented in general and for semiconductors in particular. Factors affecting the Hall measurement are presented in a concise manner, and the Hall effect for different classes of materials is discussed. The basis for the single and multi carrier model treatment is discussed with the application of magnetoconductivity tensor. The principles of impedance spectroscopy are also presented under this chapter. The fourth chapter discuses material synthesis and sample preparation techniques. The milling procedure is presented along with the method of ink formulation. The relation between the ink type and the appropriate printing techniques are presented, with references to manual and screen printing.

In chapter five the experimental techniques employed to characterize the layers are discussed. Techniques for structural studies such as transmission electron microscopy (TEM), scanning electron microscopy (SEM), X-ray diffraction (XRD), small angle X-ray scattering (SAXS), and Raman scattering are presented. The Hall measurement system and impedance measurement system are also briefly discussed. Chapter six covers results obtained from all the techniques. Its presentation is divided into two major parts covering electrical and structural results. Chapter Seven presents a unified discussion of all results, relating the outcomes from different techniques. The last chapter, chapter eight concludes the thesis.

University of Cape Town

2 Physics of Semiconductors

2.1 Classification of Materials

Materials can be classified according to their electrical property as insulators, semiconductors and conductors. Conductors of electricity are typically metals, in pure elemental form or as an alloy, with the exception of only a few non-metallic materials that are able to conduct electricity. Conducting polymers are a case in point [1]. However, most non-metallic materials fall under the category of insulators. For example polymers and ceramics are used industrially for insulation of current carrying wires.

a) Increasing

	10^{-10}	10^{-8}	10^{-4}	10^{0}	3.7×10^{5}	5.96×10^{5}	6.3×10^{5}	Conductivity $(\Omega cm)^{-1}$

b) Decreasing

	=	8500	1500	3900	14	32	52	Mobility (cm^2/V-s)

c) Increasing

	0	10^{6}	10^{10}	10^{13}	16.7×10^{22}	6.3×10^{22}	6.1×10^{22}	Carrier concentration (cm^{-3})

	Glass	GaAs	Si	Ge	Al	Cu	Ag	

Fig. 2.1 The room temperature properties of materials according to their a) electrical conductivity , b) carrier mobility, and c) carrier concentration.

University Of Cape Town

The third group of materials, the semiconductors, falls somewhere midway between conductors and insulators in terms of electrical conductivity [2]. As described in the subsequent sections, the conductivity of a material depends on both its free charge carrier concentration and their mobility. The degree of their influence depends on the material type and measurement condition. Figure 2.1 shows the classification of materials based on their electrical properties and their interdependence. Fig. 2.1 a) shows the increase of conductivity as traversed from the insulating to the metallic region. Over the metallic region, Fig. 2.1 b), the mobility is increasing as traversed from left to right, which may be regarded as the cause for the increase in the corresponding conductivity. But in the larger picture, the mobility decreases in moving from insulators to metals. From Fig. 2.1 c), the general trend of free carrier concentration is seen to increase traversing from the insulator to the metal region, but closer inspection of the metallic region shows a decrease of carrier concentration. The electrical conductivity of materials further depends on temperature. For metals the conductivity increases with decreasing temperature. Decreasing temperature is tantamount to say that there is less lattice vibration, which is the cause of the scattering of electrons. As a result conductivity increases [3]. On the other hands increasing the temperature of an intrinsic crystalline semiconductor increases both the number of charge carriers and the lattice vibrations. The temperature dependence of free charge carriers is exponential [4]. Hence the contribution of the charge carriers dominates, and the conductivity increases with temperature.

University of Cape Town

The basis for the electrical properties manifested by a solid, can be well illustrated using the energy band model, which describes the energy of electrons as a function of their wave vector, $E = E(k)$, which is commonly known as a dispersion relation [5]. In solids where a large number of atoms aggregate together, the individual energy levels of each atom tend to merge and form an energy band [6]. Within the energy band an electron can take virtually any

energy. The structure of the energy band determines the electrical properties of the solid.

There are different models to describe the mechanics of electrons in solids. The simplest is the free electron theory for metals, which assumes the electrons to be like a free gas [7]. Basically, this model can successfully address the physics of electronic transport in metallic solids, but fails to explain the differences between a metal, semiconductor and an insulator. Specifically it cannot show the origin of the energy band gap. However, the semiclassical nearly-free electron model, which considers a weak perturbation in a periodic crystal lattice, explains the origin of the band gap [8]. According to this model an electron wave is reflected at the Brillouin zone boundary setting up a standing wave satisfying the Bragg reflection condition [9]. The energy splitting caused by the weak potential between the two standing wave solutions is the band gap at the boundary of the Brillouin zone.

University Of Cape Town

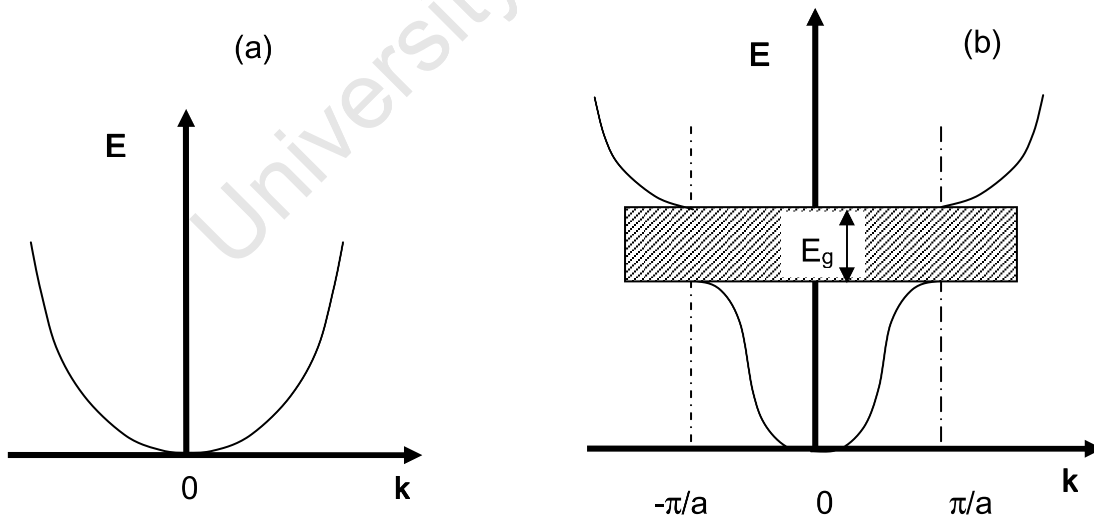

Fig.2.2: Energy band diagram for a) free electron model and b) nearly-free electron model.

In Fig. 2.2 b) there is a region between the bands representing the energy band gap. The lower band is the valence band, whereas the upper band is the conduction band. Only electrons in the conduction band can take part in electrical conduction. The band representation is generally much more complex than what is presented here, as the dispersion curves are different for different crystallographic directions.

Looking at the energy gap it is possible to categorize solids according to their response to an applied electric field as shown in Fig. 2.3.

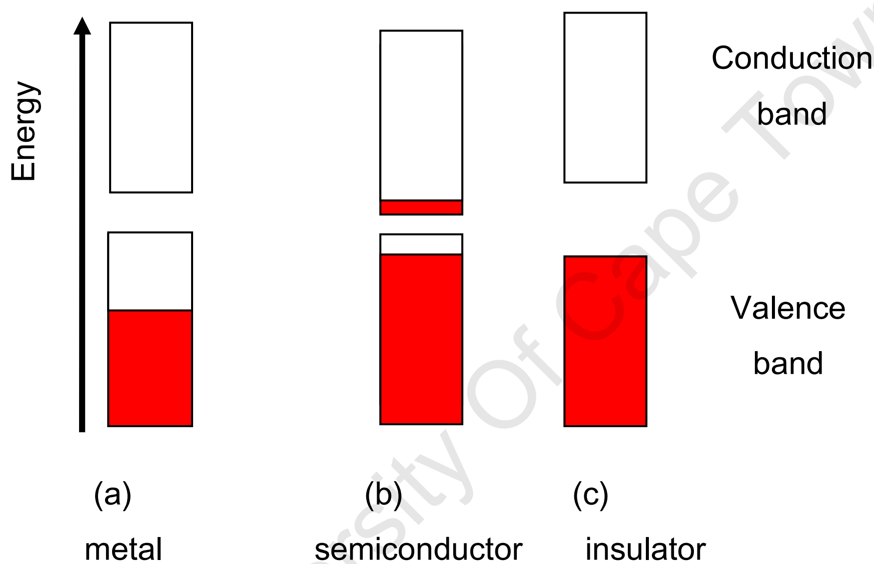

University Of Cape Town

Fig.2.3: Energy Band structure for solids

For metals the band is half filled [10] which give electrons the freedom to move easily in the crystal lattice. The difference between semiconductors and insulators is only the magnitude of the energy gap. For insulators the valence band is fully occupied and the energy gap is large, whereas for semiconductors the gap is small so that electrons near to valence band edge can be thermally excited into the conduction band. Semiconductors fall somewhere between metals and insulators. There are various kinds of semiconductors, known as elemental and compound semiconductors. Elemental semiconductors are

members of group IVA of the periodic table: silicon (Si), germanium (Ge), and certain crystallographic phases of tin (Sn) [11]. silicon and germanium are the most widely used semiconductors. The other class of semiconductors consists of compounds from neighbouring groups of the periodic table, such as GaAs, InAs *etc*. The following discussion focuses on silicon and its properties.

2.2 Silicon and its properties

Silicon is the second most abundant element in the Earth's crust next to oxygen. [12]. It is part and parcel of our everyday life, in the sense it is in every hand held electronic device to the application of space technology. It is widely used to produce solar cells and, integrated circuits. Its stability with temperature and native oxide makes it the material of choice in the semiconductor industry for most device applications. Naturally it exists in the form of oxides and silicates. Different industrial methods are employed to produce pure silicon, such as: heating silica with carbon at an elevated temperature [13], chemical vapour deposition (CVD) [14], czochralski crystal growth [15], molecular beam epitaxy (MBE) [16] casting from the melt [17], gas phase pyrolysis [18], *etc.* The processing technique used determines the phase of the silicon. Czochralski and MBE growth are well known for the processing of monocrystalline silicon with the orientation predefined by the seed crystal and substrate respectively. Casting from melt is famous for the processing of polycrystalline silicon, whereas CVD techniques primarily yield silicon in an amorphous phase, although subsequent crystallisation can be obtained by post deposition thermal treatment. Moreover the CVD and MBE techniques are known for the growth of thin film silicon for various applications. The subsequent subsections dwell on the overall properties of silicon in its different phases.

University of Cape Town

2.2.1 Crystalline silicon

The crystalline state of a solid refers to the regular arrangement of its elementary entity. Ideally the positions of the atoms are expected to be exactly periodic. An ideal crystal possesses translational symmetry, with a finite unit cell which repeats itself infinitely in three dimensions [19]. Crystalline silicon is a covalently bonded solid with a diamond crystal structure, shown in Fig. 2.4. It has a lattice constant of 5.43 Å and energy band gap of 1.12 eV at room temperature. The energy band gap is uniquely attributed to its crystalline phase.

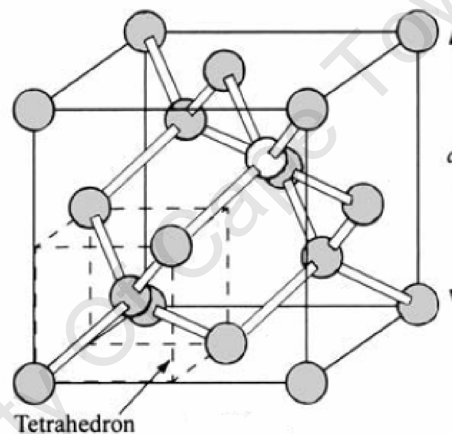

Fig.2.4: Silicon with Diamond structure [5]

University of Cape Town

In single crystalline silicon, because of its defect free structure, carriers have long life time. Crystalline silicon is the best example of a material with an indirect band gap, meaning that the minimum of the conduction band and the maximum of the valence band are not at the same k, as discussed in more detail below.

2.2.2 The band structure for crystalline silicon

Band structure is well described by plotting the possible energy states in reciprocal space. These are obtained by solving the Schrödinger equation for

single electron states [9]. The band structure diagram for silicon is given in Fig. 2.5 [20].

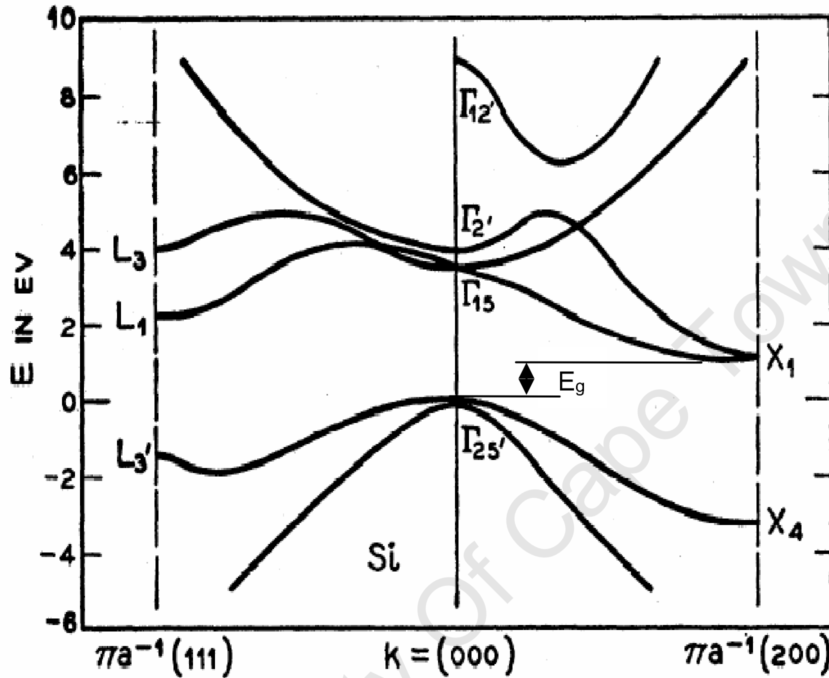

Fig.2.5: Silicon band structure [20]

If a minimum of the conduction band is directly above a maximum of the valence band, there is a direct band gap. From symmetry arguments, all crystals will have a direct band gap at the Γ point, which is the centre of the Brillouine zone. In silicon the direct band gap is 3.4 eV [21]. However, crystalline silicon has an indirect band gap in which the momentum of the state in the conduction band is displaced from that of valence band maximum, at a lower energy of 1.1 eV. Hence direct transition from the valence band to the conduction band is impossible unless assisted by phonons which carry the excess momentum.

University of Cape Town

For the material to conduct electricity there must be free charge carriers, which can be either electrons in the conduction band or holes in the valence band. The concentration of electrons as charge carriers is denoted as n whereas holes are denoted as p. Carriers may be generated by either thermal or optical processes. For intrinsic silicon at temperatures above absolute zero, some electrons can be thermally excited into the conduction band and become involved in the conduction process. The rate at which carriers are produced is known as the generation rate G. The recombination rate R describes the process through which electrons and holes annihilate each other. In thermal equilibrium, for an isolated system, the rate of generation is the same as the rate of recombination [6],

$$G = R .$$

If we denote n_o and p_o as the electron and hole carrier densities at room temperature,

$$n_o p_o = \text{constant} = n_i^2 \approx 10^{20} cm^{-3} .$$

This is referred to as the law of mass action. For an intrinsic semiconductor the concentrations of both carrier types are equal, which implies that both are $n_i \approx 10^{10} cm^{-3}$ [5].

Obviously there is a relation between the intrinsic carrier concentration n_i and temperature T. n_i is also a function of the energy required to excite an electron from the valence band to the conduction band. The minimum energy would be equal to the energy gap E_g.

2.2.3 Density of states, statistics of charge carriers

The number of states with energy E between E and $E + dE$ per unit crystal volume is called the density of states and denoted as $g(E)$. For a parabolic (nearly free) dispersion curve,

University of Cape Town

$$g(E)dE = \frac{m^* \sqrt{2m^* E}}{\pi^2 \hbar^3} dE, \tag{2.1}$$

where m^* is carrier's effective mass.

Rewriting this for the electron and hole states [22],

$$g_c(E) = \frac{m_n^* \sqrt{2m_n^*(E - E_c)}}{\pi^2 \hbar^3} \quad \text{for } E \geq E_c, \tag{2.2}$$

and

$$g_v(E) = \frac{m_h^* \sqrt{2m_h^*(E_v - E)}}{\pi^2 \hbar^3} \quad \text{for } E \leq E_v, \tag{2.3}$$

where m_h^* and m_n^* are the effective masses for the hole and electron respectively. The distribution of electrons or holes over the available energy states is governed by Fermi-Dirac statistics [5]. The probability for a state with energy E to be occupied is given by

$$f(E) = \frac{1}{\left[1 + \exp\left(\frac{E - E_F}{kT}\right)\right]}, \tag{2.4}$$

where k is Boltzmann's constant and T is absolute temperature of the system. The Fermi energy E_F, which is equal to the chemical potential, is the maximum energy of a state that can be occupied by an electron at absolute zero temperature. In Fig. 2.6 the temperature dependence of the Fermi Dirac distribution is given. At absolute zero the probability of occupancy for states with energy less than the Fermi energy is one, whereas for those with energy greater than the Fermi energy is zero with an abrupt change at Fermi energy. As the temperature increases, electrons near the Fermi level acquire enough thermal energy to occupy states with an energy greater than the Fermi energy, leaving behind empty states. As the temperature increases, more electrons are excited to higher levels. But for all temperatures the probability of occupancy of a state with energy equal to the Fermi energy is one half.

University Of Cape Town

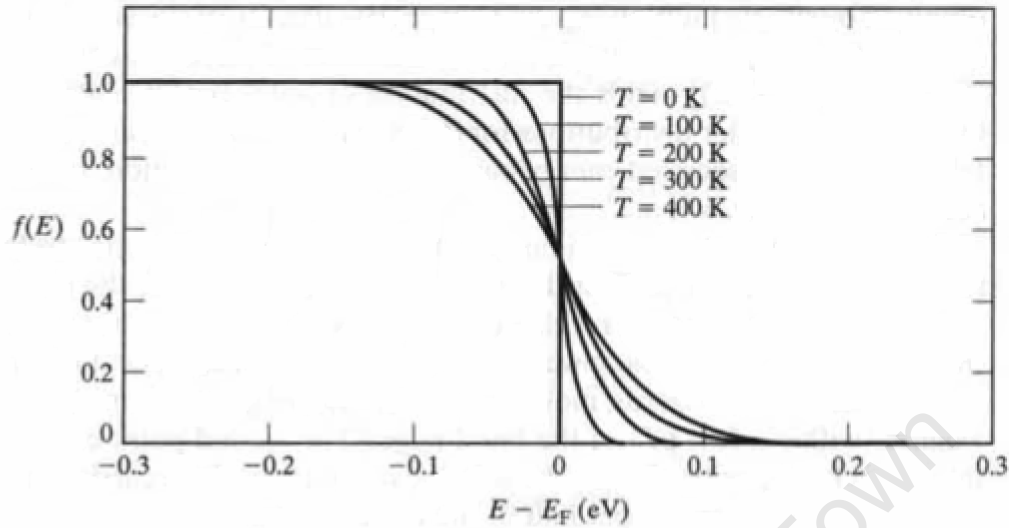

Fig.2.6: Fermi-Dirac distribution function for various temperature [6].

University Of Cape Town

Likewise, the probability for the hole to occupy the energy state E in the valence band is given by

$$f(E) = 1 - \frac{1}{\left[1 + \exp\left(\frac{E_F - E}{kT}\right)\right]}. \quad (2.5)$$

For non-degenerate semiconductors, for which the Fermi energy level is more than about $4kT$ (about 0.1 eV at room temperature) from both the conduction band or the valence band, the Fermi Dirac statistics can be approximated by Maxwell-Boltzmann's statistics, yielding approximate distribution functions

$f(E) \approx \exp\left(-\frac{E - E_F}{kT}\right)$ for $E > E_F$,corresponding to electrons, (2.6)

and

$f(E) \approx 1 - \exp\left(-\frac{E_F - E}{kT}\right)$ for $E < E_F$, corresponding to holes. (2.7)

Making use of Eqns. 2.6 and 2.7, it is possible to define the concentrations of electrons in the conduction band and holes in the valence band as

$$n = \int g_c(E) f(E) dE \,, \tag{2.8}$$

and

$$p = \int g_v(E)\left[1 - f(E)\right] dE \,. \tag{2.9}$$

Up on substitution for the densities of state we arrive at simplified expressions

$$n = N_c \exp\left(\frac{-(E_c - E_F)}{kT}\right), \tag{2.10}$$

and

$$p = N_v \exp\left(\frac{-(E_F - E_v)}{kT}\right), \tag{2.11}$$

where N_c and N_v are the effective densities of states in the conduction and valence bands respectively [22], and are given as

$$N_c = 2\left(\frac{2\pi m_n^* kT}{h^2}\right)^{3/2} \quad \text{and} \quad N_v = 2\left(\frac{2\pi m_h^* kT}{h^2}\right)^{3/2} \tag{2.12}$$

for a parabolic band.

In Figure 2.7 a) the parabolic dependence of density of state is demonstrated, which extends to both the conduction and valence bands. In Fig. 2.7b) and 2.7 c) for a temperature above absolute zero, the probability and number of carriers generated is shown. For an intrinsic material the electron density excited to the conduction band creates an equal density of holes in the valence band which is known as the intrinsic carrier concentration and can be given as

$$n = p = n_i \,. \tag{2.13}$$

University Of Cape Town

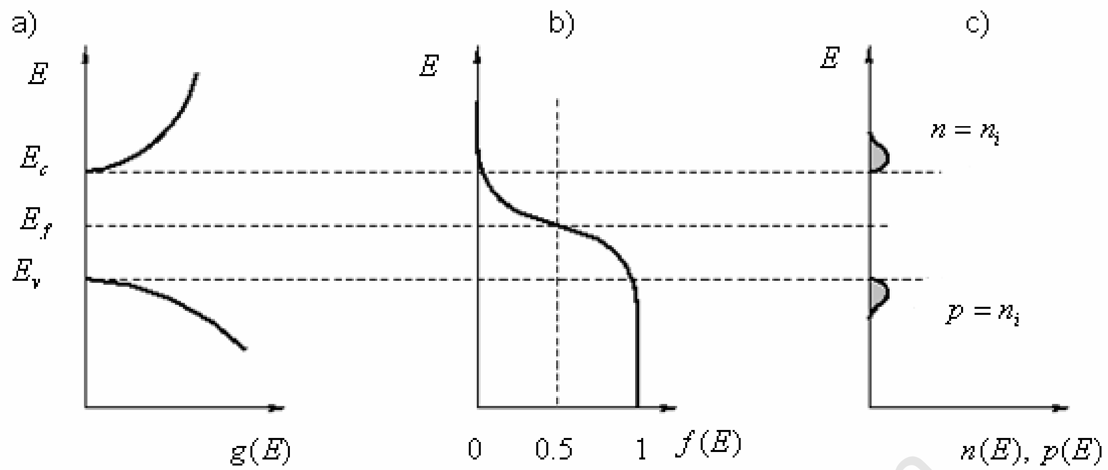

Fig.2.7: a) density of states, b) probability distribution, and c) carrier concentration of intrinsic semiconductor as a function of energy [23].

University Of Cape Town

Using equations 2.10 and 2.11 we arrive at the law of mass action mentioned earlier,

$$np = n_i^2 = N_v N_c \exp\left(\frac{E_v - E_c}{kT}\right). \tag{2.14}$$

But, $E_c - E_v = E_g$, so the expression for the intrinsic carrier concentration is

$$n_i = \sqrt{N_c N_v \exp\left(\frac{-E_g}{kT}\right)}. \tag{2.15}$$

From Eqn. 2.16, materials with lower energy gap have a higher intrinsic carrier density, as demonstrated in Fig. 2.8. In the lower temperature regime the effect is more pronounced than at higher temperatures.

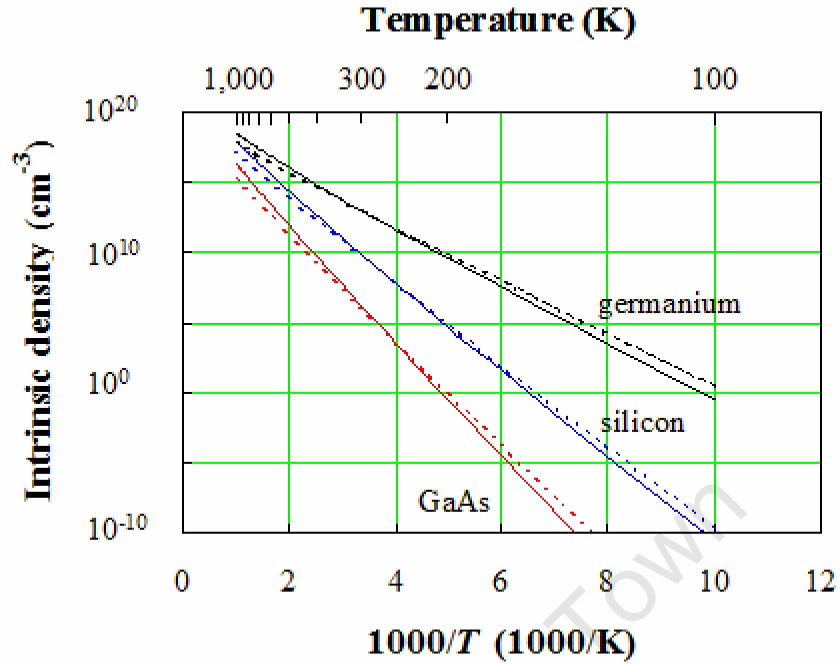

Fig.2.8: The intrinsic carrier concentration as a function temperature for different semiconducting materials with room temperature energy gaps of 0.66, 1.12 and 1.42 eV for Ge, Si and GaAs respectively [5, 24].

University Of Cape Town

The Fermi energy level in an intrinsic semiconductor can also be calculated from the condition $p = n$,

$$N_c \exp\left(\frac{-(E_c - E_F)}{kT}\right) = N_v \exp\left(\frac{-(E_F - E_v)}{kT}\right). \tag{2.16}$$

Rearranging,

$$E_F = \frac{E_c + E_v}{2} + \frac{kT}{2}\ln\left(\frac{N_c}{N_v}\right). \tag{2.17}$$

Upon substitution for N_c and N_v from Eqn. 2.12,

$$E_F = \frac{E_c + E_v}{2} + \frac{3kT}{4}\ln\left(\frac{m_h^*}{m_n^*}\right) \quad . \tag{2.18}$$

From Eqn. 2.18, the Fermi energy depends on both temperature and the effective masses of the carriers. At absolute zero the Fermi energy is midway in the energy gap. At higher temperature the second term of Eqn. 2.18 will not change appreciably and hence it can be said the Fermi energy for intrinsic material remains near the mid point of the band gap.

2.2.4 Amorphous silicon

Like its crystalline counterpart, amorphous silicon is also covalently bonded having the same average bond length and bond angle [25]. But the atoms are distributed randomly, and therefore the structure lacks the periodicity and symmetry observed in crystalline solids. The periodicity, which is the basis for the application of Bloch's theorem, cannot be applied to explain the origin of energy gap in amorphous materials. But there are alternative techniques to demonstrate the band structure of such materials, such as the chemical bond theory approach [26], which deals with the interaction between atomic orbitals. In tetrahedrally coordinated silicon, due to the intra-atomic interaction, the sp^3 hybridized orbitals are at a lower energy than the p orbital and higher than the s orbital. As shown in Fig. 2.9, in the process of interaction with the orbitals from neighbouring atoms, the molecular orbitals formed split into bonding and anti bonding states.

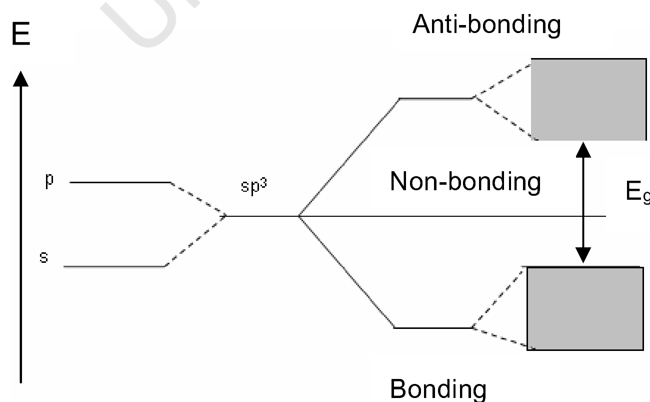

Fig.2.9: Band structure for tetrahedrally bonded semiconductor using chemical bonding theory.

University of Cape Town

In a solid, the bonding states form a band which is fully occupied by electrons whereas the anti-bonding states are empty. The bonding orbitals correspond to the valence band, whereas the anti-bonding states correspond to the conduction band. The energy difference between the lowest unoccupied molecular orbital (LUMO) and the highest occupied molecular orbital (HOMO) is the band gap. The chemical bonding theory is equally valid for crystalline and non crystalline materials, because it does not show the difference in electronic structure between the crystalline and amorphous states. However, the details of the electronic structure can be explained using the energy density of state distribution function $N(E)$ [27, 28] using a tight-binding theory. Tight-binding theory is the mathematical form required to represent the interaction between localized atomic wave functions. It considers that the electronic states can be assumed as a linear combination of atomic states [29]. According to [27, 30] the tight- binding Hamiltonian H acts on the hybridized atomic orbital, *eg*. sp^3, that can be given as a function $\left|\Phi_{ij}\right\rangle$, where the subscripts i and j refer to the atom to the bond respectively,

$$H = V_1 \sum_{j \neq j'} \left|\Phi_{ij}\right\rangle \left\langle \Phi_{ij'}\right| + V_2 \sum_{i \neq i'} \left|\Phi_{ij}\right\rangle \left\langle \Phi_{i'j}\right| . \tag{2.19}$$

V_1 is a measure of interaction strength between orbitals of the same atom but forming different bonds and V_2 is the interaction strength between orbitals contributing to the same bond but assigned to different atoms. The solution for Eqn. 2.19 confirms the existence of the energy gap in terms the density of states.

University Of Cape Town

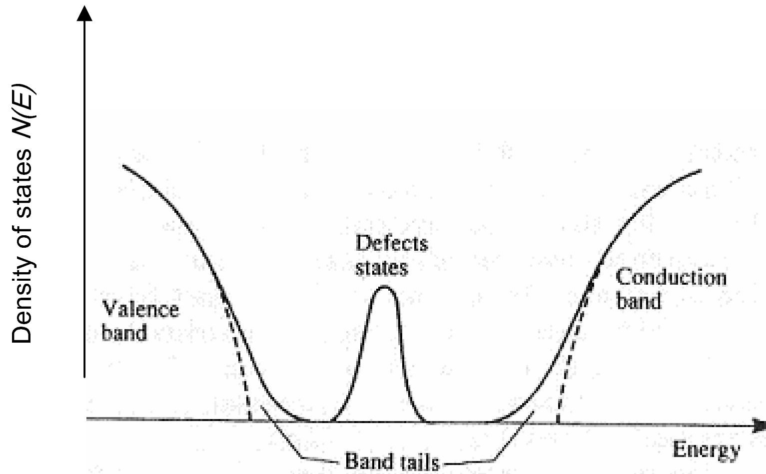

Fig. 2.10: Schematic density of states distribution for an amorphous semiconductor [25].

University Of Cape Town

Figure 2.10 shows the split of the band structure into conduction and valence bands, with the dotted line representing the density distribution for a crystalline semiconductor. The band tail which extends deep into the energy gap is attributed to the long range structural disorder in amorphous solids. The band tail states are localized states and the mobility edge separates them from extended states in the conduction band [31]. Localised states in the band gap are caused by defects such as dangling bonds, vacancies, *etc*. For amorphous silicon, because of its structural disorder, the uncertainty in momentum is comparable with the magnitude of the electron momentum [32]. Hence conservation of momentum is not a strict requirement in optical transitions. The probability of a direct transition is therefore higher than that of crystalline silicon, and hence amorphous silicon can be said to have a direct band gap [33].

2.2.5 Nanocrystalline silicon

Silicon is among those materials which show unique structural and electrical properties when in a nanostructured form [34, 35]. Nanophase silicon has the electro-optical properties of amorphous silicon, but with better stability. Light induced degradation [36], which is a common problem in amorphous silicon, is not significant in nanocrystalline silicon. The lower band gap of nanophase

silicon, compared to amorphous silicon, also enhances the absorption in the longer wavelength end of the visible spectrum. As a result nanocrystalline silicon is becoming the material of choice for the production of single or multijunction solar cells [37, 38]. Nanocrystalline silicon has further applications in thin film transistor (TFT) technology, because of its good carrier mobility [39], which is comparable to crystalline silicon.

Electronic states in a nanostructured material are said to be quantum confined if the structure size, at least in one direction, is reduced to below the Bohr radius of the exciton in the bulk material [40]. The effect of confinement is the quantization of carrier's motion in the direction of confinement [40]. One directional confinement results in a quantum well, and three dimensional confinement yields a quantum dot. In a quantum confined structure excitation requires more energy than in a large crystal the bulk, because quantization increases the optical absorption edge. The increase in energy for one directional confinement of dimension d is given as

$$\Delta E = \frac{\hbar^2 \pi^2}{2m^* d^2}, \qquad (2.20)$$

where m^* is the effective mass of the particle and $\hbar = \frac{h}{2\pi}$ is Planck's constant.

As indicated in Eqn. 2.20 the increment in energy is inversely proportional to the square of the size of the particle. By controlling the size, it is possible to tune silicon photoluminescence [41], and hence absorption over the entire range of the visible spectrum.

2.3 Doping

2.3.1 Introduction

In semiconductor and solid state physics, doping refers to a process where one intentionally adds impurities to a semiconducting material to alter its electrical

University Of Cape Town

properties. It can equivalently be described as intentionally introducing shallow level defects [42, 43]. Usually undoped semiconductors are referred to as intrinsic, whereas doped semiconductors are called extrinsic semiconductors. An extrinsic semiconductor may be N-type or P-type depending on the type of impurities added. If introducing impurities generates more electrons as free carriers, the semiconductor is said to be N-type. If the impurities introduce more holes to the semiconductor, the semiconductor is said to be P-type.

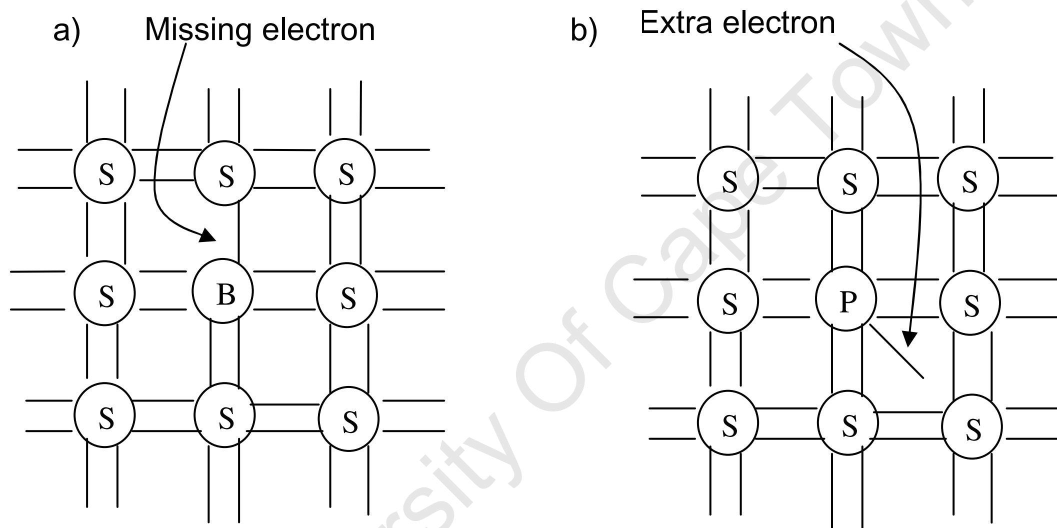

Fig.2.11: Examples of a) P-type (a) and b) N-type doping of a silicon crystal. S=silicon, B=Boron P=Phosphorous and the lines are representation of electrons.

University Of Cape Town

Silicon has four valance electrons, covalently bonded in a tetrahedral configuration with neighbouring silicon atoms producing its crystal structure. When a trivalent impurity, *e.g* boron, with three valence electrons is substituted into the crystal structure at a silicon site, it will share all its three electrons to form a bond with its neighbours. However there exists one unpaired, or unbonded, electron due to a neighbouring silicon. This literally means that the crystal is short of one electron, which is tantamount to say that there is an excess hole or unfilled state as indicated in Fig. 2.11 a). As a result doping with boron yields a

P-type semiconductor. Boron, in this example, or a trivalent dopant in general is known as an acceptor. When silicon is doped with pentavalent atom, such as phosphorous, four of the phosphorous valence electrons take part in forming covalent bonds with the four neighbouring silicon atoms, but one electron, the fifth, remains unbonded and loosely bound to the parent atom phosphorous (Fig. 2.11 b)). Such pentavalent dopants are known as donors. The electrons form weak hydrogen like states with a small binding energy of about 0.044 eV. At room temperature they can therefore be set free to take part in electrical conduction.

2.3.2 N-type semiconductor

The loosely bound electrons eventually fill up the donor states which are just below the conduction band. Only a small thermal excitation is enough to excite these electrons into the conduction band so that they are free to move through the crystal. A donor doped semiconductor is N type, with electrons constituting the majority charge carriers and holes the minority carriers. As shown in Fig. 2.12, the donor atoms will be positively ionized and the Fermi energy level shifts up to the conduction band to maintain charge neutrality.

University of Cape Town

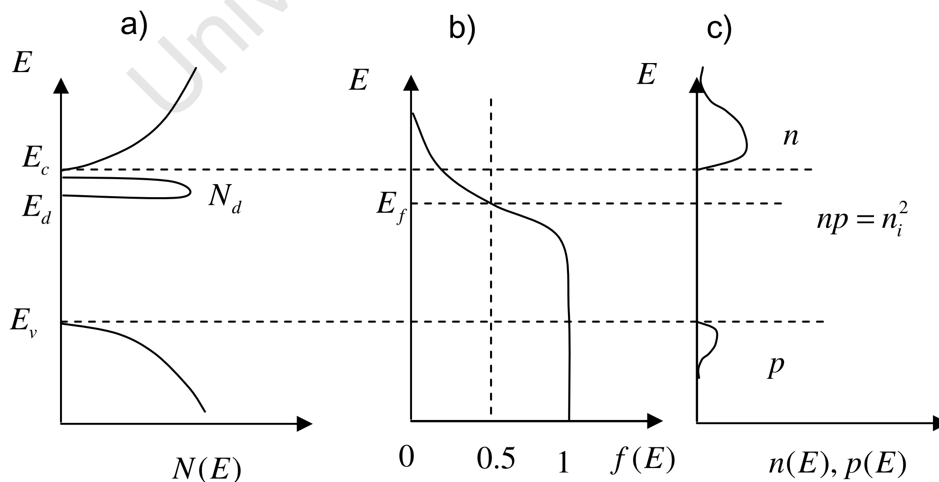

Fig.2.12: a) density of states b) probability distribution and carrier concentration in N-type semiconductor as a function of energy.

The process of doping does not cause charge unbalance, and the net charge will be zero after doping. Writing,

$\rho =$ charge density = 0 = (charge from electrons) + (charge from holes) + (charge from donors), the charge balance equation is

$$0 = (-qn_o) + (qp_o) + (qN_d)\,, \qquad (2.21)$$

where N_d = is the donor concentration (cm^{-3}) and q electronic charge.

But $n_o p_o = n_i^2$, and therefore $p_o = \frac{n_i^2}{n_o}$, so

upon substitution into equation 2.34

$$0 = -qn_o + \frac{qn_i^2}{n_o} + qN_d\,.$$

Solving the quadratic equation for n_o, we find the carrier density

$$n_o = \frac{N_d + \sqrt{N_d^2 + 4n_i^2}}{2} = \frac{N_d}{2} + \frac{N_d}{2}\sqrt{1 + \frac{4n_i^2}{N_d^2}}\,. \qquad (2.22)$$

For $N_d >> n_i$, the square root term will reduce to 1.Thus

$$n_o = N_d\,. \qquad (2.23)$$

The hole concentration is $p_o = \frac{n_i^2}{N_d}$, and is not significant. The displacement of the Fermi level from the conduction band edge can be determined by making use of Eqn. 2.23,

$$n_o = N_c \exp\left(\frac{-(E_c - E_F)}{kT}\right)\,.$$

Hence

$$N_d = N_c \exp\left(\frac{-(E_c - E_F)}{kT}\right),$$

and

$$E_c - E_F = kT \ln\left(\frac{N_c}{N_d}\right). \qquad (2.24)$$

University Of Cape Town

Equation 2.24 shows that as the donor density increases the energy difference $E_c - E_F$ decreases implying that the Fermi level is shifted towards the conduction band edge [44]. This is demonstrated in Fig. 2.13, where the Fermi level is shifted up from the mid gap position of an intrinsic semiconductor.

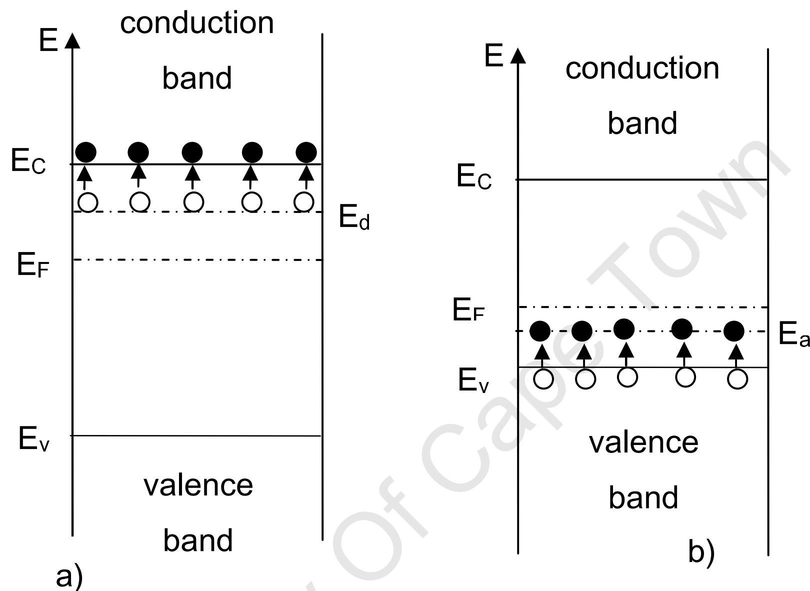

Fig.2.13: a) Donor states in the N-type semiconductor, and b) Acceptor states in a P-type semiconductor.

University Of Cape Town

2.3.3 P-type semiconductor

In a P type semiconductor a trivalent atom is covalently bonded with three neighboring silicon atoms leaving one electron unpaired. This unpaired site represents a missing bond, and at low temperature is localized around the acceptor atom. A small rise in temperature will drive electrons from another atom to fill the unpaired site thereby creating a mobile hole. In the process acceptors are ionized by receiving electrons from valence band.

For a given acceptor impurity concentration N_a the analysis will be identical with the case discussed above for the N-type semiconductor. Hence, for $N_a >> n_i$, $p_o = N_a$ and each acceptor contributes a single hole to the valence band. For thermal equilibrium the overall charge of the system is neutral and hence

$$n_o = \frac{n_i^2}{N_a},$$

and

$$N_a = N_v \exp\left(\frac{-(E_F - E_v)}{kT}\right). \tag{2.25}$$

Similarly, the position of the Fermi level is

$$E_F - E_v = kT \ln\left(\frac{N_v}{N_a}\right). \tag{2.26}$$

In Fig. 2.13 b), the Fermi level is shifted down towards the valence band edge. The acceptor states are near the valence band edge, and easily ionized at small thermal energy.

2.3.4 Compensated semiconductors

It is possible to have both types of impurities present at the same time. Such semiconductors are known as compensated semiconductors and their electrical property is dictated by the impurity with the higher density. Charge neutrality of the system is maintained and the Fermi level adjusts itself accordingly. For the charge to be neutral,

$$n_o + N_a = p_o + N_d \ . \tag{2.27}$$

We can determine the carrier concentration in a given type of semiconductor upon substituting the equilibrium condition in Eqn. 2.27.

University Of Cape Town

As a result the electron concentration in an N-type semiconductor n_{on} is given by

$$n_{on} = \frac{1}{2}\left[N_d - N_a + \sqrt{(N_d - N_a)^2 + 4n_i^2}\right], \text{ and} \tag{2.28}$$

The number of holes p_{on} by

$$p_{on} = \frac{n_i^2}{n_{on}}.$$

Similarly, the number of holes in a P-type semiconductor is

$$p_{op} = \frac{1}{2}\left[N_a - N_d + \sqrt{(N_d - N_a)^2 + 4n_i^2}\right], \tag{2.29}$$

whereas the number of electrons $n_{op} = \frac{n_i^2}{p_{op}}$.

At room temperature the magnitude of the net impurity concentration $N_d - N_a$ is much larger than the intrinsic carrier concentration n_i. Thus Eqns. 2.28 and 2.29 are simplified and given as

$$n_{on} = N_d - N_a \text{ if } N_d > N_a,$$

and

$$p_{op} = N_a - N_d \text{ if } N_a > N_d.$$

In the plot of carrier concentration as a function of temperature (Fig. 2.14) we note three distinct regions. The first is the freeze out for very low temperature, for which no impurity atoms are ionised. In this example the electrons do not have enough thermal energy to be excited into the conduction band, and the number of free electrons is less than the number of donor atoms. As the temperature increases, we reach a stage at which all the donor atoms are ionized, and hence $n_n = N_d$.

University of Cape Town

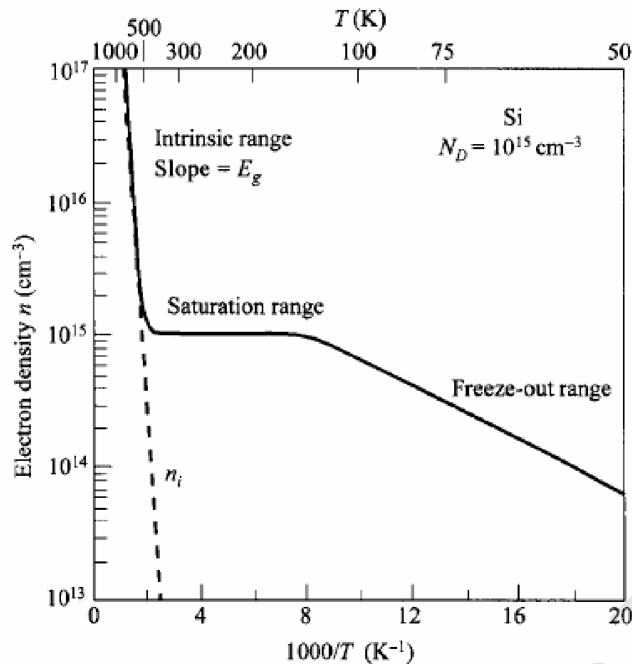

Fig.2.14: Carrier concentration as a function of temperature [44].

University of Cape Town

For a wide interval of increase in temperature, this number of electrons will be maintained. This interval is called extrinsic region. Further increase in temperature eventually results in a situation where the intrinsic carrier concentration is comparable to the donor concentration. Above this temperature the semiconductor becomes intrinsic.

2.4 The PN junction

As has been discussed above, the electrical properties of a semiconductor can be modified by doping. As a result, depending on the type of impurities, P-type or an N-type semiconductor can be produced. The purpose of changing the electrical properties of semiconductors in a controlled manner is to use them in wide range of electronic devices. The simplest example is the PN junction which forms a diode [45]. Diodes have very wide applications and are regarded as the building block of modern electronics. Diodes can be uniquely described as

devices favouring the flow of current in one direction. This property arises as a result of band structure modification at the junction. In the process of device formation, when the N-type semiconductor is brought into contact with the P-type semiconductor, the excess electrons in the N region migrate to the P region recombining with the holes. As a result free carriers in the junction region will be depleted. There will also be established a net electric field from the N region to the P region, blocking the further flow charge carriers at equilibrium. Figure 2.15 demonstrates the electric field created due to the PN junction.

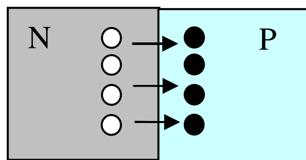

Fig.2.15: The movement of free carriers at PN junction.

Equivalently it can be said that a built in potential will develop between the two regions. Unless charge carriers are assisted by some means it is not possible for them to surmount the potential barrier. As indicated in the Fig. 2.16, for electrons to reach region p, they must overcome the barrier of energy qV_o.

University of Cape Town

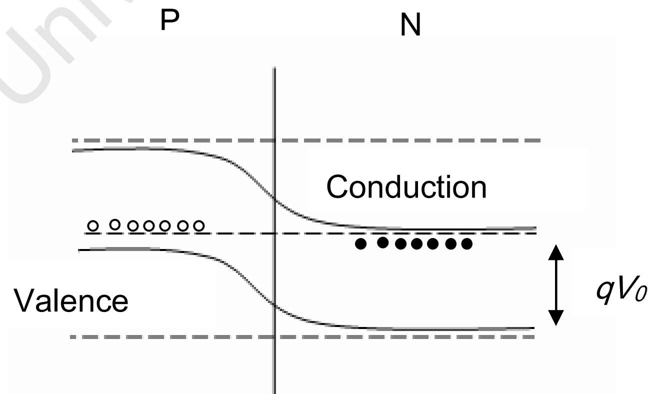

Fig.2.16: Unbiased diode energy band structure.

Under equilibrium conditions the conservation of charge can be given as

$$N_a x_p = N_d x_n \quad . \tag{2.30}$$

Poisson's equation for the P region will be

$$\frac{d^2V}{dx^2} = \frac{qN_a}{\varepsilon} .$$

Integration with the right boundary condition will yield the electric field

$$\vec{E} = \frac{qN_a}{\varepsilon}(x + x_p) . \tag{2.31}$$

Likewise for the N region,

$$\vec{E} = \frac{qN_d}{\varepsilon}(x - x_n) , \tag{2.32}$$

where V is the electric potential, $\vec{E}$ is the electric field, ε is the electric permittivity.

The electric field changes linearly in the depletion region to establish a built-in potential difference given as

$$V_o = \frac{q(N_a x_p^2 + N_d x_n^2)}{2\varepsilon} \quad . \tag{2.33}$$

The depletion length in each region is equivalent to

$$x_p = \left[\frac{2\varepsilon V_o N_d}{qN_a(N_d + N_a)} \right]^{\frac{1}{2}} , \tag{2.34}$$

and

$$x_n = \left[\frac{2\varepsilon V_o N_a}{qN_d(N_d + N_a)} \right]^{\frac{1}{2}} . \tag{2.35}$$

University of Cape Town

Combining Eqns. 2.34 and 2.35, the width of depletion w is given as

$$w = \left\{ \frac{2\varepsilon V_o}{q(N_a + N_d)} \right\}^{\frac{1}{2}} \left\{ \left(\frac{N_a}{N_d} \right)^{\frac{1}{2}} + \left(\frac{N_d}{N_a} \right)^{\frac{1}{2}} \right\}. \tag{2.36}$$

Under forward bias when the negative terminal of the bias voltage is connected to the N-type material and the positive terminal to the P-type, the built-in potential will be suppressed and hence flow of current is possible as shown in Fig. 2.17. But in reverse bias, when the negative terminal of the bias voltage is connected to the P side and positive the terminal is connected to the N side, the bias rather assists in blocking the further flow of charge.

If we let V_1 be the bias voltage, under reverse bias conditions, the depletion region is modified as

$$x_n = \left[\frac{2\varepsilon(V_o + V_1) N_a}{q N_d (N_d + N_a)} \right]^{\frac{1}{2}}, \tag{2.37}$$

with the total charge of

$$Q = q N_d x_n. \tag{2.38}$$

Therefore from Eqn. 2.38 it is possible to calculate the capacitance in this under reverse bias as [46]

$$C = \frac{\partial Q}{\partial V_1} = \left\{ \frac{q\varepsilon}{2(V_o + V_1)} \frac{N_a N_d}{N_a + N_d} \right\}^{\frac{1}{2}}. \tag{2.39}$$

University Of Cape Town

But since all electrons are not at the same energy, there is a probability for some to acquire sufficient energy so that they surmount the built-in potential and reach the other side. The resulting current is called saturation current.

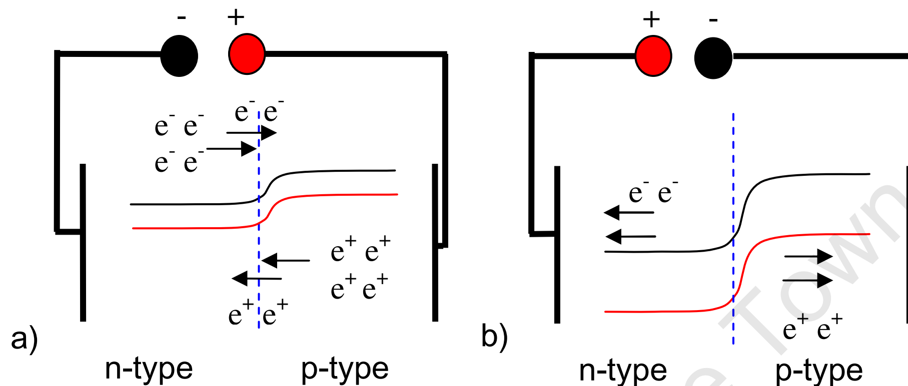

Fig.2.17: PN junction under a) forward and b) reverse bias.

University of Cape Town

Applying Boltzmann's statistics to quantify the energy shifts, the saturation current can be determined by making use of the following relations [47]

$$n = N_c \exp\left(-\left(\frac{E_c - E_f}{kT}\right)\right), \tag{2.40}$$

and

$$p = N_v \exp\left(-\left(\frac{E_f - E_v}{kT}\right)\right). \tag{2.41}$$

Combining Eqns. 2.40.and 2.41 with the condition $n = N_d$ for the N-type region and $p = N_a$ for the P-type region yields

$$E_c - E_f = kT \ln\left(\frac{N_c}{N_d}\right). \tag{2.42}$$

The inbuilt potential energy difference across the junction is

$$qV_o = E_g - (E_c - E_f) - (E_f - E_v)$$
$$= E_g - kT \ln\left(\frac{N_c N_v}{N_d N_a}\right) \quad . \qquad (2.43)$$

The bias voltage and current dependence in the diode is then given by the relation [47]

$$I = I_s \exp\left(\frac{qV_1}{kT} - 1\right). \qquad (2.44)$$

Equation 2.44 is known as the diode equation and is applicable to an ideal PN junction. For a real junction or device this is modified by the introduction of an ideality factor n to give

$$I = I_s \exp\left(\frac{qV_1}{nkT} - 1\right). \qquad (2.45)$$

University of Cape Town

3 Carrier Transport and the Hall Effect

In general terms, in any system there are different types of charge transport, which can be explained in terms of the material type and its crystallinity. As an external electric field is applied to a crystalline conductor or semiconductor, drift type charge transport is set up [1]. Apart from drift, there are other charge transport mechanisms which are more dependent on the temperature, as well as on the electric field. The following sections present an overview of the charge carrier transport in both crystalline and non-crystalline materials.

3.1 Electrical conductivity in crystalline semiconductors

If we consider a crystalline semiconductor at a temperature above absolute zero, electrons are continuously in collision with phonons [2]. As a result electrons undergo a Brownian type motion without a net displacement. When an external field is applied to the semiconductor, electrons tend to be drifted in the opposite direction to the field. As a result a drift current density, J, will be formed [3]. In terms of the carrier charge density, n and carrier drift velocity, v the current density is given as

$$J = nqv\,, \tag{3.1}$$

where q is the electric charge.

The current density assumes a positive value in the direction of the applied electric field $\vec{E}$. For electrons as charge carriers $q<0$, and hence v is in opposite direction to the current density J. For holes, for which $q>0$, v assumes the direction of the current density. Thus if we neglect the random thermal motion, the equation of motion can be given as [4].

University of Cape Town

$$\frac{d(mv)}{dt} + \frac{mv}{\tau} = qE, \tag{3.2}$$

where t is time, mv is the momentum, and τ is an average momentum relaxation time. The second term on the left hand side of Eqn. 3.2 results from scattering from lattice vibrations agitated by thermal energy. For a system in a steady state, the first term vanishes and Eqn. 3.2 will be reduced to

$$\frac{mv}{\tau} = qE, \tag{3.3}$$

from which the drift velocity can be obtained as

$$v = \frac{\tau qE}{m} = \mu E, \tag{3.4}$$

where $\mu = \frac{\tau q}{m}$ is the drift mobility [5].

Substituting Eqn. 3.4 in Eqn. 3.1 for v, yields

$$J = nq\mu E \quad . \tag{3.5}$$

From Eqn. 3.5 the conductivity σ can be defined as

$$\sigma = nq\mu \ . \tag{3.6}$$

Substituting Eqn. 3.4 in Eqn. 3.6 yields

$$\sigma = \frac{nq^2}{m}\tau . \tag{3.7}$$

The inverse of conductivity is the resistivity ρ, given as

University Of Cape Town

$$\rho = \frac{1}{\sigma} = \frac{1}{nq\mu}. \quad (3.8)$$

In most practical applications the numerical value of τ is the inverse of the vibration frequency of atoms in the crystal and is of the order of about 10^{-13} s at room temperature [5]. As can be seen from Eqn. 3.7, the ratio $\frac{q}{m}$ is an important parameter that helps to determine the mobility for a given type of carrier.

Semiconductor with mixed carriers

In general in a semiconductor, carriers of both types, holes (p) and electrons (n), co-exist. The conductivity of the material is therefore given by the contribution from each type [6]

$$\begin{aligned} \sigma &= q(p\mu_p + n\mu_n) \\ &= q(p+nb)\mu_p \end{aligned}, \quad (3.9)$$

where μ_p is hole mobility, μ_n is electron mobility, and b is the ratio $\frac{\mu_n}{\mu_p}$.

For an intrinsic semiconductor the carrier concentration $n = p = n_i$. Therefore the conductivity can be given as

$$\sigma = qn_i\mu_p(1+b). \quad (3.10)$$

The intrinsic carrier concentration n_i is temperature dependent and given as [3, 5]

$$n_i = \sqrt{N_v N_c}\exp(\frac{-E_g}{kT}), \quad (3.11)$$

where N_v and N_c are the densities of states in the valance and conduction bands respectively, and E_g is the band gap energy. Equation 3.11 shows that the intrinsic carrier density n_i increases with temperature. The plot of σ versus

University Of Cape Town

the inverse of temperature $\left(\frac{1}{T}\right)$, shown in Fig. 3.1 for an arbitrary doped semiconductor, shows an Arrhenius behaviour at high temperature when the conduction is dominated by intrinsic carriers. As the temperature decreases, σ enters the extrinsic region where the carrier concentration is nearly constant. As has been discussed in Chapter 2, over this region, the contribution of mobility to conductivity dominates. As the temperature decreases further, the carriers finally freeze out and the conduction approaches zero.

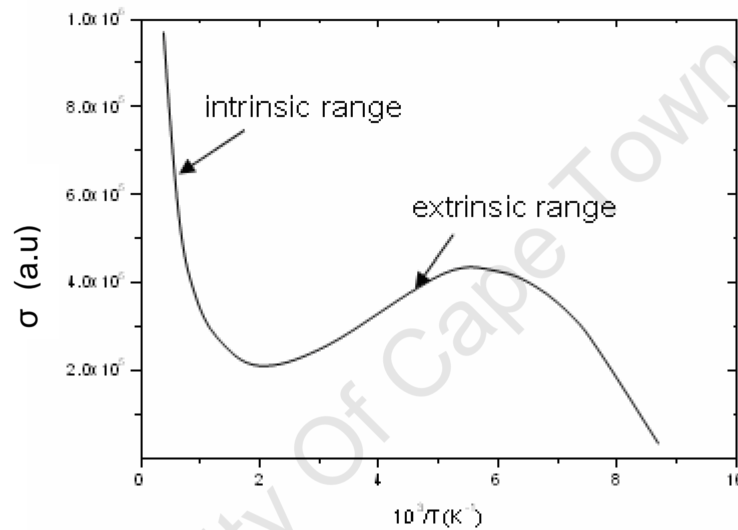

Fig.3.1: Schematic diagram of conductivity of doped crystalline semiconductor as a function of inverse temperature. Adapted from [7].

University Of Cape Town

3.2 Electrical conductivity in non-crystalline semiconductors

The energy band structure is the basis to understand and explain the different charge transport mechanisms. As has been discussed in Chapter 2, the Bloch theory which was used to show the origin of band gap for semiconducting materials is not applicable to non-crystalline materials. An alternative approach, which deals with the density of states, can be utilized to predict the energy band gap. The density of states shown schematically in Fig. 3.2 is based on

Anderson's [8] work which predicts the presence of an energy gap for non crystalline solids. Section two of chapter two above discussed how the energy gap is formed in non crystalline semiconductors.

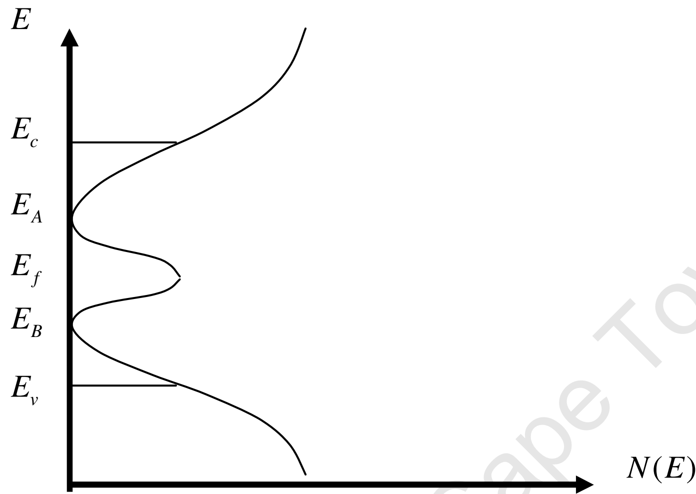

Fig.3.2: Density of states for non-crystalline materials [9].

University Of Cape Town

In Fig. 3.2 [9], E_c and E_v are boundaries between localized states and extended states. Equivalently, these are referred to as the mobility edges. In non-crystalline materials there are defects associated with the bond, and, overall, with the structure of the material, which are responsible for the localized band tail states [10]. The mid gap localized states are caused by defects with deep energy levels such as dangling bonds. At absolute zero the electrons in the localized states cannot contribute to conduction, but electrons in the delocalized states, which are the extended states, would be free to move and contribute to the conduction. Referring to Fig. 3.2, when $E_f < E_c$ the Fermi level is in the localized state region, at finite temperature two types of conduction are expected: thermally

activated conduction via the extended states, and hopping between the localized states [11]. The thermal excitation conductivity is given as

$$\sigma = \sigma_o \exp\left(\frac{-(E_c - E_f)}{kT}\right), \tag{3.12}$$

where σ_o is a constant conductivity prefactor.

Hopping describes direct transitions of charge carriers from occupied localized states to unoccupied states [12]. For randomly distributed localized states with a separation distance between two localized states R and an inverse of localization length α, the transition probability υ_{hop} in the presence of an external electric field $\vec{E}$ can be given as [13]

$$\upsilon_{hop} = \upsilon_{ph} \exp\left(-2\alpha R - \left(\frac{W \pm qER}{kT}\right)\right), \tag{3.13}$$

where W is the energy barrier between the two states, and υ_{ph} is the hop attempt per unit time, which is taken as a constant optical phonon frequency [14]. The first exponential term is the overlap wavefunction from the two states which is gives the probability of tunneling [15]. The second exponential term will be considered positive if the hop is in the direction of the applied electric field. Otherwise for a hop in opposite direction it assumes negative sign. This is a Boltzmann factor to indicate the probability for the electron to acquire sufficient energy to overcome the barrier and reach the second localized state. For a very small applied electric field such that $qER << kT$, the hopping conductivity is given as [13]

$$\sigma = 2q^2R^2\upsilon_{ph}N(E_f)\exp\left(-2\alpha R - \frac{W}{kT}\right), \tag{3.14}$$

University of Cape Town

where q is the electric charge and $N(E_f)$ the density of states at the Fermi level.

Strong localization is the condition for nearest neighbour hopping, for which $\alpha R_o >> 1$, where R_o is the distance to the nearest neighbour. For weak localization, when $\alpha R_o \leq 1$ (or in all cases at low temperature), variable range hopping dominates. The average hopping distance is not constant but decreases as the temperature increases. The conductivity follows the power law temperature dependence proposed by Mott [16]

$$\sigma(T) = \sigma_o \exp\left[\left(-\frac{T_o}{T}\right)^{\frac{1}{4}}\right], \quad (3.15)$$

where T_o is a characteristic temperature constant.
At constant temperature the AC conductivity can be expressed as

$$\sigma_{AC}(\omega) = \sigma_{DC} + A\omega^s \quad , \quad (3.16)$$

where A and s are temperature dependent parameters, and σ_{DC} is the limiting conductivity as $\omega \to 0$. Ping Sheng [17] proposed a model different to that of Mott, known as fluctuation induced tunneling. According to this model, the distribution of localized states is not random. There exists a matrix of large conducting regions separated by small insulating barriers. Within the conducting region electrons (carriers) can freely move, and tunneling to the next conducting region is assisted by phonons. The conductivity in the overall process is given by

$$\sigma = \sigma_o \exp\left[\left(\frac{T_o}{T + T_1}\right)\right], \quad (3.17)$$

where T_o and T_1 are characteristic temperatures. The shape, geometry, and dimension of the conducting region, and the insulating barrier helps to determine

University Of Cape Town

the values of σ_o, T_1 and T_o. It can be argued that the description given in this model fits the material this work is based on. The details of samples that have been used will be discussed in the next chapter, but to relate with description given above, our samples are made of silicon particles in a binding medium. Each particle represents a large conducting medium and the region between neighbouring particles can be considered as a thin insulating barrier.

Ballistic transport

Ballistic transport is a type of transport in which the carriers traverse a material without encountering collision or scattering. In simple terms it can be visualized in terms the motion of electrons from the electron gun in a cathode ray tube, but practically its description is more subtle. The following characteristic distances are of importance in defining ballistic transport: the mean free path L_m and the Fermi wavelength, $\lambda_F = \frac{2\pi}{k_F}$, which is the de Broglie wavelength of electron at the Fermi energy [18]. Consider Fig. 3.3 given below, ballistic transport is observed if L is less than L_m.

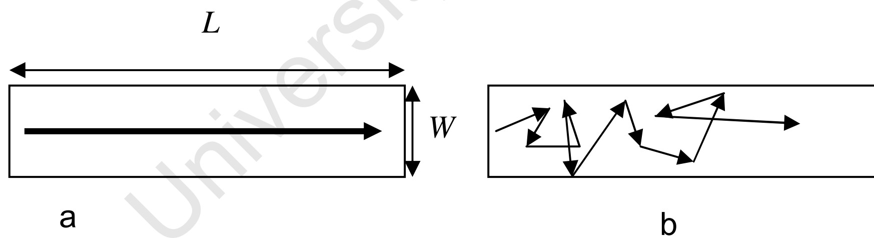

Fig.3.3: Electron in a thin conductor with a) ballistic and b) drift transport limited by Brownian motion.

University Of Cape Town

If the carrier travels without scattering, ideally there should be no resistance. But that is not the case, and in ballistic conduction there is a limiting conductance [19]. For mesoscopic systems this can be explained from a quantum mechanical point of view. In Fig. 3.3, for $W << L$, if there is a potential difference between the two ends, we can define the conductance G as

$$G = \sigma \frac{W}{L} \quad , \tag{3.18}$$

where σ is the conductivity of the material. This relation holds for macroscopic dimensions of the conductor and hence conductance is proportional to the width W. But if W is very small and comparable to the Fermi wavelength$\left(\lambda_f\right)$, conductance is independent of W. From the mathematical relation it appears that if W is kept small and the size of L is reduced, it appears the conductance would be infinite. But this is not the case and always there is a limiting conductance G_c when the length L becomes shorter than the mean free path [19]. The limiting conductance can be accounted for by the contact resistance and an intrinsic conductance G_o arising from quantum mechanical phenomena. This value of $G_o = 2\frac{e^2}{h}$ is the quantum conductance [20].

Nanostructured materials such as carbon based nanostructures show ballistic type transport [21]. These days intensive research is being carried out to come develop ballistic transport devices with immense technological advantages by the virtue of their high speed.

3.3 The Hall effect

The Hall effect is observed when a current carrying conductor or semiconductor in placed in a magnetic field. Due to the interaction between the charge carriers and the magnetic field, an electric field will set up in a direction perpendicular to both the magnetic field and the current. The effect is named after E. T. Hall who

University of Cape Town

observed the phenomena for the first time in 1879 [22]. These days the Hall effect is a standard technique to determine electrical parameters such as carrier density, carrier type and, carrier mobility of conductors or crystalline semiconductors.

3.3.1 Description of the Hall effect

When two points in a material are subject to a potential difference, and hence an electric field $\vec{E}$ is applied across the material, charge carriers will be drifted with an average velocity of $\vec{v}$. As the current carrying material is placed in a magnetic field $\vec{B}$, the carriers experience an average Lorentz force given by

$$\vec{F}_L = q(\vec{E} + \vec{v} \times \vec{B}) , \qquad (3.19)$$

where q is the charge of the carrier, $\vec{v}$ is the drift velocity of charge carriers, and $\vec{B}$ is the magnetic field.

Figure 3.4 shows a slab, of dimensions $l \times b \times d$, placed in a region of magnetic field, in the direction out of the page and perpendicular to the direction of current. Due to the Lorentz force, the carriers in the slab are drifted towards its bottom edge. As a result a Hall field is induced in the y direction setting up an electric force that opposes the further flow of carriers.

University of Cape Town

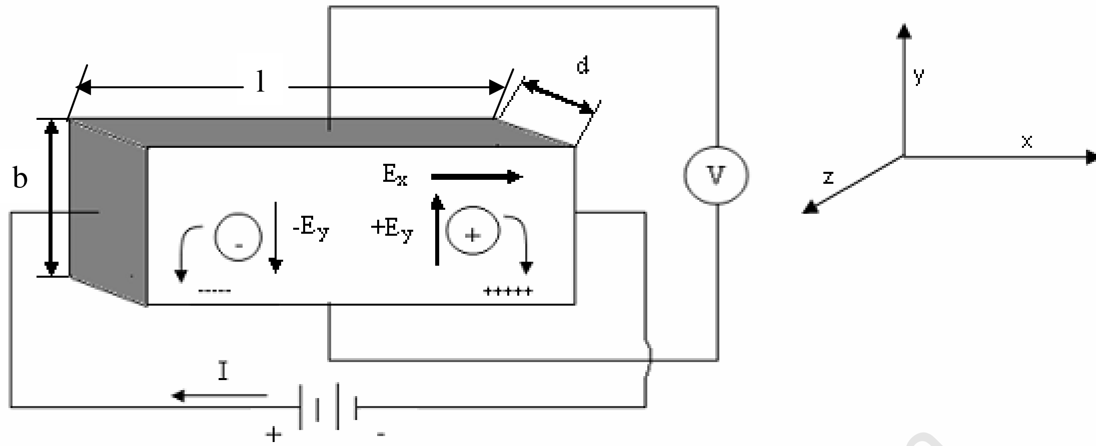

Fig. 3.4: Schematic of the Hall effect for the magnetic field direction (z) out of the page.

University of Cape Town

If we consider the presence of both carriers, the classical equations of motion can be given as

$$\frac{d\vec{v}_n}{dt} + \frac{\vec{v}_n}{\tau} = -\frac{q}{m}\left(\vec{E} + \vec{v}_n \times \vec{B}\right) \tag{3.20}$$

for electrons, and

$$\frac{d\vec{v}_p}{dt} + \frac{\vec{v}_p}{\tau} = -\frac{q}{m}\left(\vec{E} + \vec{v}_p \times \vec{B}\right) \tag{3.21}$$

for holes. For steady state the above equations will be reduced to

$$\vec{v}_n = -\frac{q\tau}{m}\left(\vec{E} + \vec{v}_n \times \vec{B}\right) = -\mu_n\left(\vec{E} + \vec{v}_n \times \vec{B}\right) \tag{3.22}$$

and

$$\vec{v}_p = -\frac{q\tau}{m}\left(\vec{E} + \vec{v}_p \times \vec{B}\right) = \mu_p\left(\vec{E} + \vec{v}_p \times \vec{B}\right). \tag{3.23}$$

The total current density is thus

$$\vec{J} = nq\mu_n\left(\vec{E} + \vec{v}_n \times \vec{B}\right) + pq\mu_p\left(\vec{E} + \vec{v}_p \times \vec{B}\right). \quad (3.24)$$

At equilibrium the net current density along the y direction is zero,

$$0 = J_y = \sigma E_y - qr_H(p\mu_p^2 - n\mu_n^2)E_x B_z, \quad (3.25)$$

but

$$E_y = R_H J_x B_z \approx R_H \sigma E_x B_z. \quad (3.26)$$

Substitution and solving for R_H yields

$$R_H = \frac{qr_H}{\sigma^2}(p\mu_p^2 - n\mu_n^2) = \frac{r_H}{q}\frac{p\mu_p^2 - n\mu_n^2}{(p\mu_p + n\mu_n)^2} = \frac{r_H}{q}\frac{p - nb^2}{(p + nb)^2}, \quad (3.27)$$

where $b = \frac{\mu_n}{\mu_p}$ is the ratio of mobilities, and r_H is the scattering factor which is a dimensionless constant of value between 1 and 2 [7].

Because of the difference in mobilities, the Hall coefficient changes sign when the conductivity, $\sigma = \sigma_i = n_i q(\mu_p + \mu_n)$ at $p = nb^2$, instead of at the intrinsic concentration $n = p$. At room temperature the ratio of mobilities b has magnitude of a few decades, implying that the Hall coefficient of intrinsic or lightly P-type doped material should be negative. Under such conditions electrons will be the dominant carrier type, and the material will appear to be N-type. If a single carrier type dominates in the material, the above equations will be reduced to

University Of Cape Town

$$R_H = -\frac{r_H}{qn} \text{ for electron dominated,}$$

and

$$R_H = \frac{r_H}{qp} \text{ , for hole dominated material.}$$

The Hall coefficient is negative if the carriers are electrons but positive for holes. In short, it is an indicator of the dominant carrier type and doping level of a material. If the drift velocity is assumed constant for all carriers, and the effects of magnetic field strength, impurity level, temperature *etc*. are ignored, the scattering factor takes a value equal to one. As a result for N-type material

$$R_H = \frac{1}{nq}. \tag{3.28}$$

To show the relation between the Hall coefficient and the Hall mobility, for a given single carrier type, making use of the above equations,

$$R_H \sigma = r_H \mu_d = \mu_H , \tag{3.29}$$

where μ_d is the drift mobility.

Thus, the Hall mobility μ_H may be defined as the product of conductivity σ and the Hall coefficient R_H. Although they have similar magnitude, the Hall mobility and drift mobility are only equal when the scattering factor assumes a value of 1.

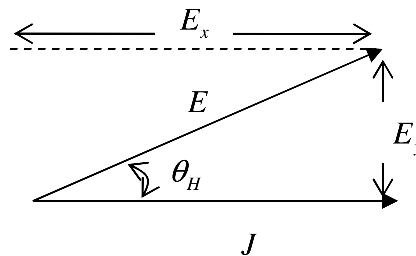

Fig.3.5: Sketch to describe the Hall angle.

University of Cape Town

The Hall angle θ_H is the angle between the net electric field in a conductor and the current density given by

$$\tan\theta_H = \frac{E_y}{E_x}, \qquad (3.30)$$

as indicated in Fig. 3.5, where E_x is the applied electric field and E_y is the induced Hall field.

Since $R_H = \frac{V_H d}{BI}$ and $\sigma = \frac{Il}{v_x bd}$, their product will be

$$R_H\sigma = \frac{V_H}{v_x} \times \frac{l}{b} \times \frac{1}{B}. \qquad (3.31)$$

Rearranging Eqn. (3.31) yields

$$R_H\sigma B = \frac{E_y}{E_x} = \tan\theta_H . \qquad (3.32)$$

But we have shown that $R_H\sigma = \mu_H$, so

$$\tan\theta_H = \mu_H B . \qquad (3.33)$$

This relation, whose significance is to define the mobility, signifies that in a real situation, the direction of the current and the electric field may not coincide, resulting in the planar Hall effect.

3.3.2 Factors affecting the Hall measurement

There are two possibilities for sources of error while measuring Hall Voltages: the sample geometry, and the intrinsic properties of the measurement [23].

University Of Cape Town

I Errors from sample geometry:

Generally there are two categories of sample geometries for the Hall effect measurement. The first category is called the Hall bar geometry. From the experimental description of Hall's article [22], it can be inferred that the sample had the geometry given in Fig. 3.6 a). Other geometries such as the type indicated in Fig. 3.6 b) were introduced to measure the resistivity in addition to the Hall voltage. This geometry has an advantage in minimizing the error in the Hall measurement with less risk of shorting the Hall voltage. Lakeshore Cryotronics who specialize in building Hall measurement systems, have adopted three similar geometries of this type that comply with their measurement system. The second category is known as the van der Pauw geometry [24]. In principle the van der Pauw technique is applicable to any arbitrary shape, but in practice symmetric shapes, like those shown in Fig. 3.7, are almost always used. The following subsections discuss the geometrical requirements and the potential errors introduced in the measurements. More elaborate discussion with respect to the error related to each type of geometry can be found in [24].

Hall bar geometry

Deviation from perfect symmetry in the hall bar geometry will cause uncertainty in the current and voltage measurements. The minimum requirement in terms of the aspect ratio is $\frac{l}{w} \geq 3$ [25]. Figure 3.6a represents a hall bar with finite contact size, which is also an important parameter in the sample preparation. The acceptable contact size in terms of the dimension of the sample is $\frac{c}{L} \simeq \frac{1}{6}$, which keeps the errors to a minimum. Violation of this requirement substantially affects the current density and electric potential around the contact, introducing large errors in the resistivity and Hall coefficient [23, 24]. When the contact is made into a fingerlike structure, as shown in Fig. 3.6 b), the size of the contact can be made smaller which improves the quality the measurement.

University of Cape Town

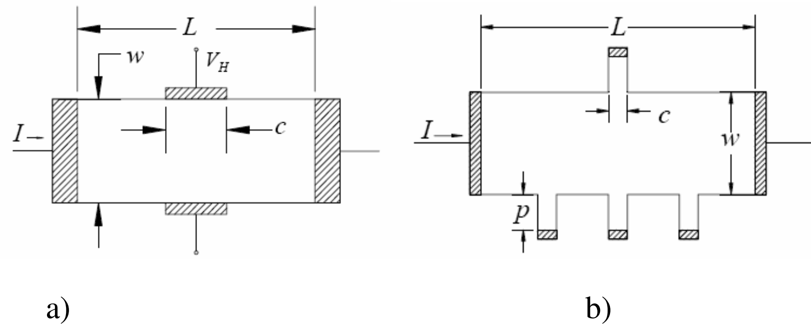

a) b)

Fig.3.6: a) Hall Geometry with finite contact, b) Reduced contact size with finger structure [23].

Van der Pauw geometry

The van der Pauw method is the most common because it makes it possible to handle samples with arbitrary shapes with as small a contact size as achievable as possible [26]. Using the same general principle, Look [24] proposed other geometries applying van der Pauw's condition to minimize the possible error in the Hall measurement. The most widely used geometries, shown in Fig. 3.7, are square, circular, Greek cross and clover leaf structures. In all cases the appropriate way to minimize the error is to maintain the ratio of the contact size to the sample size, c/L, to less than 1/6. The circular structure has been shown to introduce the least error [24].

a) b) c) d)

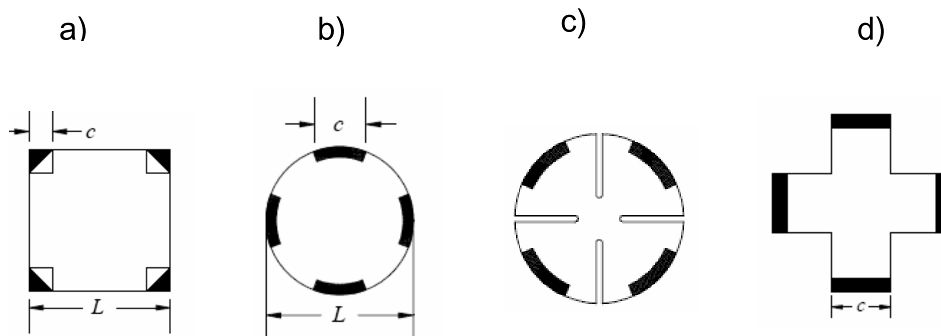

Fig.3.7: Van der Pauw geometries for Hall effect measurements: a) square, b) circular, c) cloverleaf, and d) Greek Cross [23].

University of Cape Town

II- Intrinsic sources of error

Intrinsic sources of error refer to unavoidable properties, which can be attributed to factors including the geometry of the sample, the condition in which the experiment is executed, and the instrumentation used for the experiment. The following description gives an insight to the possible sources of systematic errors in Hall voltage measurements [7, 23].

A voltmeter offset (V_O): This originates entirely from poor calibration of the voltmeter. It has nothing to do with either the direction of flow of current or to the direction of the external magnetic field. If the voltmeter is not properly zeroed, it always shows some offset voltage which adds to the measurement.

An ammeter offset (I_O): Likewise, poor calibration of ammeter contributes to the offset current reading by the ammeter which eventually affects the measurement. The offset current is independent of both the direction of the flow of charge and the direction of the external magnetic field.

Misalignment Voltage (V_M): This is attributed to the lack of symmetry in depositing the metal contacts. Experimentally it is difficult to attain a perfect alignment of the two contacts for the Hall voltage measurement. As a result even without applying a magnetic field it is possible to detect a potential difference between the two contacts which can be of the order of the Hall voltage itself. Fig. 3.8 demonstrates the misalignment between the Hall contacts numbered 2 and 4. The voltage recorded between points 2 and 4 appears as an additional value to the real Hall voltage.

University of Cape Town

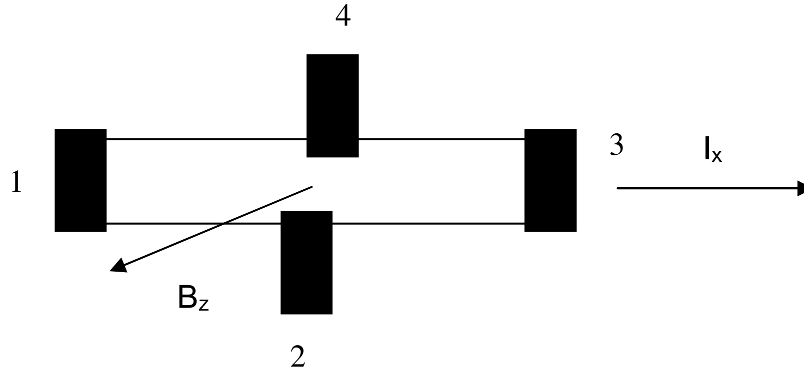

Fig.3.8: Misalignment of Hall voltage contacts causing an error in the Hall voltage.

For a sample with resistivity ρ and cross sectional area A and length between points ij of L_{ij}, for $i, j = 1, 2, 3$ and 4, the resistance of the sample (between points 1 and 3) can be given as

$$R = \frac{\rho}{A} L_{13}, \tag{3.34}$$

from which

$$\frac{\rho}{A} = \frac{R}{L_{13}}. \tag{3.35}$$

But for the applied potential difference V between points 1 and 2 of the sample in Fig. 3.8,

$$\frac{\rho}{A} = \frac{V}{I_x L_{13}} \quad , \tag{3.36}$$

or

$$I_x = \frac{A}{\rho} \frac{V}{L_{13}}. \tag{3.37}$$

If we let the potential difference between points 1 and 4 be V_{14} and the potential difference between points 1 and 2 be V_{12},

$$V_{14} = \frac{\rho}{A} I_x L_{14}, \tag{3.38}$$

University Of Cape Town

and

$$V_{12} = \frac{\rho}{A} I_x L_{12} . \tag{3.39}$$

The misalignment is in effect when $L_{14} \neq L_{12}$, resulting in a potential difference due to misalignment

$$V_M = V_{14} - V_{12} \tag{3.40}$$

$$= \frac{\rho}{A} I_x \left(L_{14} - L_{12} \right) \tag{3.41a}$$

$$= \frac{R}{L_{13}} \left(L_{14} - L_{12} \right) I_x . \tag{3.41b}$$

The Seebeck effect voltage (V_S): When there is a temperature gradient between two points of a metal or semiconductor, there will be a thermoelectric effect also known as the Seebeck effect [27]. If the temperature difference between the two points is given as ΔT, then an open circuit thermal emf is established between the points. Referring to Fig. 3.9, if there is a temperature gradient between the Hall voltage terminals, 2 and 4, it contributes a thermal emf to the Hall voltage measurement which is independent of the direction of the sample current and the magnetic field.

University of Cape Town

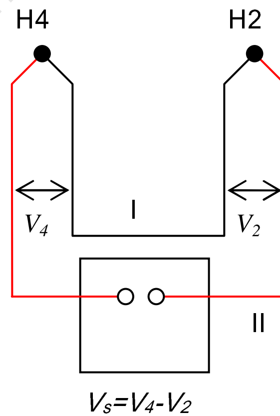

Fig. 3.9 The thermocouple circuit to detect the Seebeck voltage.

The Seebeck voltage can be measured only with the thermocouple circuit as indicated in Fig. 3.9. When the two tips of thermocouples H2 and H4 are connected to the Hall terminals, 2 and 4 of Fig. 3.10, thermal effect will be observed between the two different metals, I and II, of the thermocouples which can be expressed as a thermal emf. These thermal emfs, from Fig. 3.9, are V_4 and V_2 from which the relative potential difference between the two points is given as $V_s = V_4 - V_2$. The Seebeck voltage is linearly proportional to the temperature difference between the two points and can be given as

$$V_s = \alpha(\Delta T), \qquad (3.42)$$

where α is the Seebeck coefficient.

The Ettingshausen effect voltage (V_E): Not all charge carriers move at the same speed, which can be explained in terms of energy associated with each particle. Fast moving charge carriers are those with greater kinetic energy or thermal energy. The slower charge carriers are those with lower thermal energies, the deflection of slow carriers is higher than that of the fast carriers. As a result the Lorentz force sorts the fast and slow carriers towards the side of the sample. The net effect is that carriers with low internal energy deflect more and accumulate at one side of the sample. The side which is occupied by these carriers becomes colder than the opposite. This favours the build up of a transverse temperature gradient between the sides, which in turn causes a Seebeck effect.

University of Cape Town

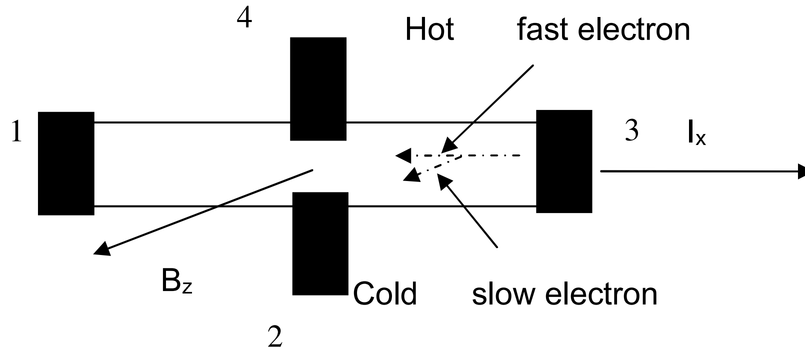

Fig.3.10: Slow electrons deflecting more than fast electrons.

The Ettingshausen effect is called isothermal if the longitudinal temperature gradient $\frac{\partial T}{\partial x} = 0$. As shown in Fig. 3.10, the slow moving electrons are deflected down to contact number 2 which results in a transverse temperature gradient between points 2 and 4. The temperature gradient is [28, 29]

$$\frac{\partial T}{\partial y} = P_E I_x B_z, \tag{3.43}$$

where P_E is the Ettingshausen coefficient, which has dimensions of volume per energy. Unlike the Seebeck voltage, V_E is proportional to both current and magnetic field.

The Nernst effect voltage (V_N): The Nernst effect is observed when, in the presence of magnetic field, there is a longitudinal temperature gradient across the sample. Figure 3.11 shows heat flow applied to the sample block instead of electric current. The electrons tend to diffuse from the hot end to the cold end of the sample in an attempt to attain thermal equilibrium. But these mobile charges experience a Lorentz force causing them to deflect towards the sides of the sample. The effect is the same as Hall effect, setting up a transverse electric field to balance the Lorenz force

University Of Cape Town

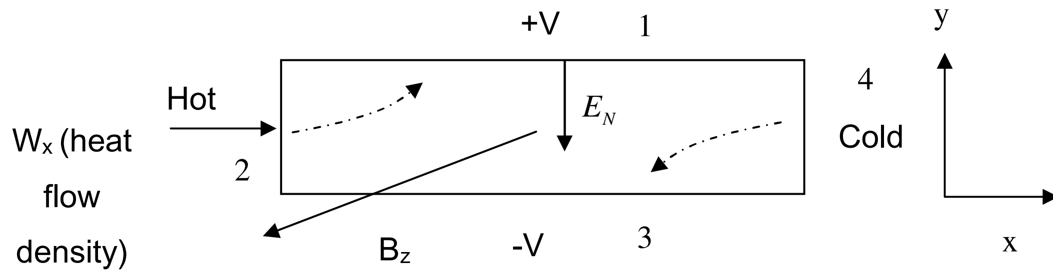

Fig.3.11: The Nernst Effect [29].

The intensity of the Nernst electric field E_N is given by [30]

$$E_N = Q_N \frac{\partial T}{\partial x} B_z , \tag{3.44}$$

where Q_N is the Nernst coefficient. The isothermal Nernst effect is subject to there being no transverse temperature gradient, $\frac{\partial T}{\partial y} = 0$. From Eqn. 3.44 above the resulting Nernst voltage V_N is proportional to the magnetic field. It is an intrinsic error source to the Hall voltage measurement which cannot be eliminated by current or field reversal.

University of Cape Town

The Righi-Leduc effect voltage (V_R): The Righi-Leduc effect is a type of chain effect which depends on all the effects discussed above. There is a possiblity for the diffusing electrons in the Nernst effect to acquire different values of velocity which is the condition for Ettingshausen effect to develop. The Ettingshausen effect then establishes a temperature gradient between the two sides of the sample. The resulting Seebeck voltage is known as the Righi-Leduc voltage V_R. The Righi-Leduc voltage is proportional to magnetic field and independent of the applied external current. The transverse temperature gradient due to the Righi-Leduc effect is [31]

$$\frac{\partial T}{\partial y} = S_{RL} \frac{\partial T}{\partial x} B_z \,, \tag{3.45}$$

where S_{RL} is the Righi-Leduc coefficient.

Combining all the effects discussed above the apparent Hall voltage V_{Ha} is therefore given as

$$V_{Ha} = V_H + V_o + V_M + V_S + V_E + V_N + V_{RL} \,. \tag{3.46}$$

With the exception of the Ettingshausen effect and the Hall voltage all the above errors can be eliminated by taking a series of measurements. For simplicity consider a sample with Van der Pauw geometry, shown in Fig. 3.12. The black dots represent the metal contact points. Numbering is in the anticlockwise direction.

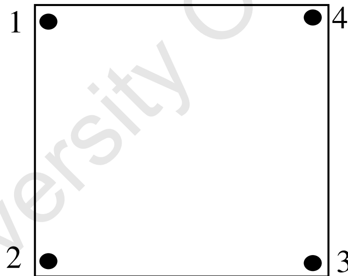

Fig.3.12: The van der Pauw geometry.

It is possible to perform eight measurements of potential differences V_{ij} between points $i\ j$ when a current I_{kl} is made to pass through contacts k and l where $i, j, k, l = 1, 2, 3\ \&\ 4$.

For forward magnetic field (+B), directed out of the page,

University Of Cape Town

$$I_{13};V_{24} = V_1 = V_H + V_o + V_M + V_S + V_E + V_N + V_R\,,$$
$$I_{31};V_{24} = V_2 = -V_H + V_o - V_M + V_S - V_E + V_N + V_R\,, \qquad (3.47)$$
$$I_{24};V_{13} = V_3 = V_H + V_o + V_M + V_S + V_E + V_N + V_R\,,$$

and

$$I_{42};V_{13} = V_4 = -V_H + V_o - V_M + V_S - V_E + V_N + V_R\,.$$

For the reverse magnetic field (-B)

$$I_{13};V_{24} = V_5 = -V_H + V_o + V_M + V_S - V_E - V_N - V_R\,,$$
$$I_{31};V_{24} = V_6 = V_H + V_o - V_M + V_S + V_E - V_N - V_R\,,$$
$$I_{24};V_{13} = V_7 = -V_H + V_o + V_M + V_S - V_E - V_N - V_R\,, \qquad (3.48)$$

and

$$I_{42};V_{13} = V_8 = V_H + V_o - V_M + V_S + V_E - V_N - V_R\,.$$

Rearranging identical potentials, the apparent Hall voltages V_{Ha}, between the same contact points, but for opposite magnetic field, are given by

$$2V_{Ha1} = V_1 - V_5 = 2V_H + 2V_E + 2V_M + 2V_N\,,$$
$$2V_{Ha2} = V_6 - V_2 = 2V_H + 2V_E - 2V_M - 2V_N\,,$$
$$2V_{Ha3} = V_3 - V_7 = 2V_H + 2V_E + 2V_M + 2V_N\,, \qquad (3.49)$$
$$2V_{Ha4} = V_8 - V_4 = 2V_H + 2V_E - 2V_M - 2V_N\,.$$

A simple arithmetic results in the experimental Hall voltage [26]

$$V_H + V_E = \frac{(V_{Ha1} + V_{Ha2} + V_{Ha3} + V_{Ha4})}{4}\,. \qquad (3.50)$$

As one can observe, most of the expressions that potentially contribute to the error in the Hall voltage measurement are eliminated in Eqn. 3.50. In the final expression, only the Ettingshausen effect remains as extra term appearing along

University of Cape Town

with Hall voltage. However, since its effect under normal circumstances is small it can be neglected.

3.3.3 Resistivity measurements in Van der Pauw geometry

As discussed above there are different options for the geometry to be used for Hall effect and resistivity measurements. In both cases, there are potential sources of both intrinsic and geometry related errors. The following discussion is based on the van der Pauw geometry shown in Fig. 3.10. For more accurate and reliable measurements, the general requirement is a homogeneous sample with small and symmetric metal contacts. It is also advisable the four contact points should be along the periphery, and the contact size should not exceed 10% of the shortest distance between metal contacts [23].

The following notations are used to calculate the sheet resistance or resistivity:

I_{ij} = positive dc current injected in at contact i and out at contact j; and

V_{kl} = dc voltage measured between positive terminal k and negative terminal l,

$$V_{kl} = V_k - V_l . \qquad (3.51)$$

Hence the resistance can be defined in terms of the measurement as

$$R_{12,34} = \frac{V_{34}}{I_{12}} \quad \text{or} \quad R_{21,43} = \frac{V_{43}}{I_{21}} ,$$

where the first two indices indicate the direction of the current and the second the potential difference. For good ohmic contacts the following conditions apply

$$R_{12,43} = R_{21,34} ,$$
$$R_{23,14} = R_{32,41} ,$$
$$R_{34,21} = R_{43,12} , \qquad (3.52)$$

and

University of Cape Town

$$R_{41,32} = R_{14,23}.$$

From the reciprocity condition we also have

$$R_{12,43} + R_{21,34} = R_{43,12} + R_{34,21} \ , \tag{3.53a}$$

and

$$R_{23,14} + R_{32,41} = R_{14,23} + R_{41,32} \,. \tag{3.53b}$$

To minimize the possible errors in the measurement the following geometry based definitions are used to define resistance and subsequently resistivity,

$$R_A = \frac{R_{12,43} + R_{21,34} + R_{43,12} + R_{34,21}}{4}, \tag{3.54a}$$

and

$$R_B = \frac{R_{23,14} + R_{32,41} + R_{14,23} + R_{41,32}}{4}. \tag{3.54b}$$

According to van der Pauw, the sheet resistivity R_s and resistivity ρ are defined by [32, 33]

$$\exp\left(\frac{-\pi R_A}{R_s}\right) + \exp\left(\frac{-\pi R_B}{R_s}\right) = 1, \tag{3.55}$$

and

$$\rho = \left(\frac{\pi d}{\ln 2}\left(\frac{R_{12,43} + R_{23,14}}{2}\right)\right) f \ , \tag{3.56}$$

where d is the sample thickness and f is the van der Pauw correction factor which is a function of the ratio $\frac{R_{12,43}}{R_{23,14}}$ [34],

University Of Cape Town

$$\frac{\left(R_{12,43}/R_{23,14}\right)-1}{\left(R_{12,43}/R_{23,14}\right)+1} = f \operatorname{arc}\cosh\left\{\frac{\exp\left(\ln 2/f\right)}{2}\right\}. \tag{3.57}$$

Denoting the ratios of resistances as $Q = \frac{R_{12,43}}{R_{23,14}}$, Eqn. 3.57 can be rewritten as

$$\frac{Q-1}{Q+1} = f \operatorname{arc}\cosh\left\{\frac{\exp\left(\ln 2/f\right)}{2}\right\}. \tag{3.58}$$

The van der Pauw correction factor f may be regarded as a measure of symmetry of the sample. For a perfectly symmetric sample $f = 1$ [35].

Under conditions where the possible parasitic effects should be taken into account, measurement for all permutations according to the geometry defined is necessary. Reversing the current for each contact and averaging for the geometries yield the expression for the resistivity as [23]

$$\rho = \frac{\pi d}{\ln 2}\left(\frac{1}{8}\right)\left[\left(R_{12,43} - R_{21,43} + R_{23,14} - R_{32,14}\right) f_A + \left(R_{34,21} - R_{43,21} + R_{43,12} - R_{34,12}\right) f_B\right]. \tag{3.59}$$

Equation 3.59 represents the average resistivity of the material. The functions f_A and f_B can be determined from Q_A and Q_B respectively using similar conditions to Eqn. 3.58, with

$$Q_A = \frac{R_{12,34} - R_{21,34}}{R_{23,14} - R_{32,14}}, \tag{3.60}$$

and

$$Q_B = \frac{R_{34,21} - R_{43,21}}{R_{43,12} - R_{34,12}}. \tag{3.61}$$

University of Cape Town

3.3.4 Hall effect measurement in van der Pauw geometry

Assuming an isotropic system, in the presence of a magnetic field but ignoring the contribution from the magnetoresistivity, the electric field is given by

$$\vec{E} = \rho \vec{J} + \rho \mu_H \left(\vec{J} \times \vec{B} \right). \tag{3.62}$$

For the van der Pauw geometry, shown in Fig. 3.10, the expression for the potential difference across the diagonal between contacts 4 and 2 is

$$\left(V_4 - V_2 \right) = \int_2^4 \vec{E} \cdot d\vec{r} . \tag{3.63}$$

This can be evaluated with and without an external magnetic field. In the absence of a magnetic field, it will be

$$\left(V_4 - V_2 \right)_{B=0} = \rho \int_{r_2}^{r_4} \vec{J} \cdot d\vec{r} . \tag{3.64}$$

Similarly, in the presence of a magnetic field it will be

$$\left(V_4 - V_2 \right)_B = \rho \int_{r_2}^{r_4} \vec{J}' \cdot d\vec{r} + \rho \mu_H \int_{r_2}^{r_4} \left(\vec{J}' \times \vec{B} \right) \cdot d\vec{r} . \tag{3.65}$$

For small point contacts, the current density, can be assumed to remain constant when the field is applied, *i.e* $\vec{J} = \vec{J}'$*,* and therefore, the Hall voltage is given as

University of Cape Town

$$V_{H42} = \left(V_4 - V_2\right)_B - \left(V_4 - V_2\right)_{B=0} = \rho\mu_H \int_{r_2}^{r_4} (\vec{J} \times \vec{B}) \cdot d\vec{r} \, . \quad (3.66)$$

Evaluating Eqn. 3.65 yields [36]

$$V_{H42} = \frac{\rho\mu_H BI}{d} . \quad (3.67)$$

Likewise the Hall voltage for the other diagonal, between contacts 3 and 1, can be obtained so that the average value for the Hall coefficient is

$$R_H = \frac{d}{B}\left[\frac{R_{31,42} + R_{42,13}}{2}\right]. \quad (3.68)$$

The expressions $R_{31,42}$ *etc.* maintain their definitions discussed earlier, for example $R_{31,42} = \frac{V_{H42}}{I_{31}}$. Equation 3.68 is the general expression for the Hall coefficient. As for the resistivity, the contribution from all parasitic effects should be dealt with by considering the average for all permutations by reversing the polarities of both current and magnetic field to get

$$\begin{aligned} R_H = \frac{d}{B}\left(\frac{1}{8}\right)[&R_{31,42}(+B) - R_{13,42}(+B) + R_{42,13}(+B) - R_{24,13(+B)} + \\ &R_{13,42}(-B) - R_{31,42}(-B) + R_{24,13}(-B) - R_{42,13}(-B)] \end{aligned} . \quad (3.69)$$

where $+B$ is the relative positive magnetic field and $-B$ is the magnetic field in opposite direction.

3.4 Multiple carrier types and the magnetoconductivity tensor

The descriptions of Hall effect theory given above represents an approximation to the real transport situation in materials. Since it deals with a single magnetic field

University of Cape Town

measurement to determine the Hall coefficient and, of course, resistivity at zero field, the parameters extracted are limited to the dominant, or majority, carrier type for which the conduction is assumed to take place in a single band of a spherical Fermi surface. Conduction in a single band is characterised by having single relaxation time and a single value of mobility representing a single carrier type. However, practical samples may behave differently with complex conduction band structures with a non spherical Fermi surface or non parabolic dispersion curve [37]. Under such conditions the relaxation time or the mobility is not unique. The corresponding band is referred to as a multiband structure with multicarrier type [38, 39]. For such a multicarrier system, the conventional Hall effect is not adequate for the analysis and even could be misleading [38].

Silicon is an example of a multicarrier system with degenerate heavy and light holes, and heavy and light electrons. For P-type silicon it is possible to observe both types of holes. Likewise it is possible to observe the two types of electron carriers for their corresponding excitation energy.

An alternative technique to analyse the Hall effect is determination of the magnetoconductivity tensor which helps to determine parameters such as carrier density and carrier mobility for a given materials or devices with multicarrier or multiband structures [38]. The field dependent conductivity tensor analysis is a powerful technique to study the electrical properties of materials. Consider a sample placed in a magnetic field with an applied current along x-axis.

University of Cape Town

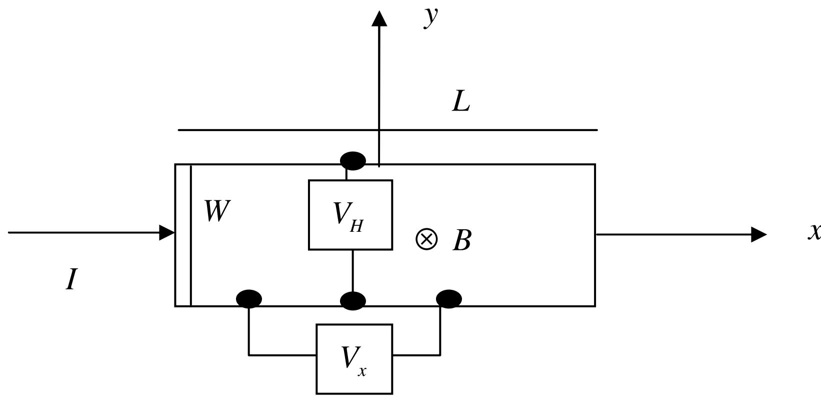

Fig.3.13: A simple sketch for the resistivity measurement.

From the sketch given in Fig. 3.13 the resistivity tensor components can be given as

$$\rho_{xx} = \frac{V_x}{I}\frac{W}{L} \tag{3.73}$$

and

$$\rho_{xy} = \frac{V_H}{I} \tag{3.74}$$

Ohm's law is thus given in tensor form as

$$J_i = \sigma_{ij}(B)E_j\,, \tag{7.75}$$

or equivalently in terms of the resistivity tensor

$$E_i = \rho_{ij}(B)J_j \tag{3.76}$$

where $i, j = x, y, z$. In the expanded form with Cartesian coordinates Eqn. 7.75 reads

$$\begin{bmatrix} J_x \\ J_y \\ J_z \end{bmatrix} = \begin{pmatrix} \sigma_{xx} & \sigma_{xy} & \sigma_{xz} \\ \sigma_{yx} & \sigma_{yy} & \sigma_{yz} \\ \sigma_{zx} & \sigma_{zy} & \sigma_{zz} \end{pmatrix} \begin{bmatrix} E_x \\ E_y \\ E_z \end{bmatrix}. \tag{3.77}$$

University Of Cape Town

The relation between the coefficients in Eqns. 3.75 and 3.76 is

$$\rho_{ij}\sigma_{jk} = \delta_{ik}, \quad (3.78)$$

where $\delta_{ik} = \begin{matrix} 1 & i = k \\ 0 & i \neq k \end{matrix}$.

In matrix form

$$\begin{pmatrix} \rho_{xx} & \rho_{xy} & \rho_{xz} \\ \rho_{yx} & \rho_{yy} & \rho_{yz} \\ \rho_{zx} & \rho_{zy} & \rho_{zz} \end{pmatrix} \begin{pmatrix} \sigma_{xx} & \sigma_{xy} & \sigma_{xz} \\ \sigma_{yx} & \sigma_{yy} & \sigma_{yz} \\ \sigma_{zx} & \sigma_{zy} & \sigma_{zz} \end{pmatrix} = \begin{pmatrix} 1 & 0 & 0 \\ 0 & 1 & 0 \\ 0 & 0 & 1 \end{pmatrix}. \quad (3.79)$$

The expressions for the isotropic system can be obtained from this expression with conditions stated as follows. For the magnetic field acting along the z-coordinate direction $(B = B_z)$, the following are the conditions for isotropy [40, 41]

$$\begin{aligned} \sigma_{xx}(B) &= \sigma_{yy}(B), \\ \sigma_{xy}(B) &= -\sigma_{yx}(B), \end{aligned} \quad (3.80)$$

and

$$\sigma_{xz}(B) = \sigma_{zx}(B) = \sigma_{yz}(B) = 0. \quad (3.81)$$

For isotropy in the xy-plane, equations Eqns. 3.77 and 3.79 can be therefore given as

University of Cape Town

$$\begin{bmatrix} J_x \\ J_y \end{bmatrix} = \begin{pmatrix} \sigma_{xx} & \sigma_{xy} \\ \sigma_{yx} & \sigma_{yy} \end{pmatrix} \begin{bmatrix} E_x \\ E_y \end{bmatrix}, \qquad (3.82)$$

and

$$\begin{pmatrix} \rho_{xx} & \rho_{xy} \\ \rho_{yx} & \rho_{yy} \end{pmatrix} \begin{pmatrix} \sigma_{xx} & \sigma_{xy} \\ \sigma_{yx} & \sigma_{yy} \end{pmatrix} = \begin{pmatrix} 1 & 0 \\ 0 & 1 \end{pmatrix}. \qquad (3.83)$$

This can be equivalently rewritten as

$$\rho_{xx}\sigma_{xx} + \rho_{xy}\sigma_{yx} = 1, \qquad (3.84a)$$

$$\rho_{xx}\sigma_{xy} + \rho_{xy}\sigma_{yy} = 0, \qquad (3.84b)$$

$$\rho_{yx}\sigma_{xx} + \rho_{yy}\sigma_{yx} = 0, \qquad (3.84c)$$

and

$$\rho_{yx}\sigma_{xy} + \rho_{yy}\sigma_{yy} = 1. \qquad (3.84d)$$

Taking into account the condition for isotropy and substituting in Eqns. 3.84 b) and 3.84 c), the longitudinal and transversal conductivity tensor are obtained as

$$\sigma_{xx} = \frac{\rho_{xx}}{\rho_{xx}^2 + \rho_{xy}^2} \qquad (3.85)$$

and

$$\sigma_{xy} = \frac{\rho_{xy}}{\rho_{xx}^2 + \rho_{xy}^2}. \qquad (3.86)$$

But $\rho_{xy} = R_H B$, and using the definitions for Hall coefficient, the conductivity tensor is given by [42]

$$\sigma_{xx} = \frac{\rho_{xx}}{\rho_{xx}^2 + (R_H B)^2} = \frac{nq\mu}{1 + (\mu B)^2}, \qquad (3.87)$$

and

$$\sigma_{xy} = \frac{R_H B}{\rho_{xx}^2 + (R_H B)^2} = \frac{nq\mu^2 B}{1 + (\mu B)^2}, \qquad (3.88)$$

University of Cape Town

where n is the carrier concentration, μ is the mobility, and q is the charge of the carrier. ρ_{xx} and R_H are the standard measured quantities of longitudinal magneto resistance and Hall coefficient respectively.

Equations 3.87 and 3.88 are based on the assumption that the system contains a single charge carrier. For the multicarrier condition, the conductivities of individual carriers are additive and the total conductivity tensor of N carriers is given by

$$\sigma_{xx} = \sum_{i}^{N} \frac{n_i q_i \mu_i}{1+(\mu_i B)^2} = \sum_{i}^{N} \sigma_{xx,i} , \qquad (3.89)$$

and

$$\sigma_{xy} = \sum_{i}^{N} \frac{n_i q_i \mu_i^{\,2} B}{1+(\mu_i B)^2} = \sum_{i}^{N} \sigma_{xy,i} = B \sum_{i}^{N} \mu_i \sigma_{xx,i} , \qquad (3.90)$$

where n_i is the density of carrier i, q_i is the charge of carrier type i, $q_i = +q$ for holes and $-q$ for electrons carriers. The mobility μ_i is related to the critical magnetic field given as

$$B_i \simeq \frac{1}{\mu_i} = \frac{m_i^*}{\tau_i q} , \qquad (3.91)$$

where m_i^* is the effective mass and τ_i is the average relaxation time for a carrier of type i.

For a predefined number of carrier types, N, the least-square fit of measured data given in Eqns. 3.87 and 3.88 to Eqns. 3.89 and 3.90 can help to determine the carrier concentrations n_i and their mobilities, μ_i.

University Of Cape Town

In this notation,

$\sigma_{xy} > 0$ for holes,

$\sigma_{xy} < 0$ for electrons,

and

$\sigma_{xx} > 0$ always for either type of carrier.

An alternative method called the reduced conductivity tensor has been proposed to extract the same information [43, 44] but with one less parameter, which makes a computational steps simpler. In the reduced conductivity tensor, the longitudinal and transversal conductivity tensors are normalized to the conductivity at zero field. The components of the reduced conductivity tensor, the longitudinal reduced conductivity tensor, S_{xx} and the transversal reduced conductivity, S_{xy} are respectively given as [45]

$$S_{xx} = \frac{\sigma_{xx}}{\sigma_o}, \tag{3.92}$$

and

$$S_{xy} = \frac{2\sigma_{xy}}{\sigma_o}, \tag{3.93}$$

where σ_o is the zero field conductivity. The factor 2 is introduced for convenience so that the absolute value of the transverse reduced conductivity assumes the value equal to one [43]. The parameter f_i, which is the fractional contribution of carrier type i, is defined as

$$f_i = \frac{q_i}{\sigma_o} n_i \mu_i = \frac{|n_i \mu_i|}{\sum_i^N |n_i \mu_i|}. \tag{3.94}$$

The fitting equations are given as

University Of Cape Town

$$S_{xx} = \sum_{i}^{N} \frac{f_i}{1+(\mu_i B)^2}, \tag{3.95}$$

and

$$S_{xy} = 2B\sum_{i}^{N} \frac{f_i \mu_i}{1+(\mu_i B)^2}. \tag{3.96}$$

For N - fold multicarrier systems, the following conditions hold

$$0 \le f_i \le 1,$$

and (3.97)

$$\sum_{i}^{N} f_i = 1.$$

The parameters $B, \mu_{i,} f_i$ may be used as fitting parameters for the reduced conductivity. Graphical analysis, when the reduced conductivity tensor is expected to fulfill certain criteria for either a single carrier or a multicarrier system, makes the analysis more convenient. The criteria for single carrier conduction are

$$S_{xx}(B=0) = 1,$$
$$S_{xx}(B=B_m) = 0.5,$$

and (3.98)

$$\left|S_{xy}(B=B_m)\right| = 1.$$

where B_m is the magnetic field at which the transverse component of the reduced conductivity tensor assumes its extremum value. For multicarrier conduction the criteria are applied to the sum of all reduced conductivity tensors given as

$$S_{xx}(B=0) = 1,$$
$$S_{xx}(B=B_m) \ne 0.5, \tag{3.99}$$

and

University of Cape Town

$$\left|S_{xy}(B = B_m)\right| < 1 .$$

3.5 Hall effect in disordered systems

In disordered semiconductors, particularly in amorphous silicon, an anomalous Hall effect (AHE) is observed. The AHE is seen as sign reversal of the Hall voltage, which would indicate a reversal of the carrier type, and is a common occurrence in non-crystalline semiconductors studied so far [46]. An N-type semiconductor may for example therefore appear to have holes as the majority carrier [46]. Although some attempts have been made to develop a theory that best explains the phenomena, there is thus far no satisfactory explanation, and the phenomenon remains puzzling. Street [36] discussed two theories, both suggesting scattering to be the cause for the sign reversal. The explanation which is based on strong scattering, expressed in terms of the transfer integral between the involving sites, failed to fully account for the anomalous Hall effect. The first theory proposed by Friedman [47] was for the Hall effect of carriers at the mobility edge. According to this theory, the anomalous Hall effect is caused because of the interference of the scattering from two paths involving three sites A, B and C. The first path involves a direct transition from A to B while the second path is a transition from A to B via C. Regardless of the material type used, the model confirmed that the Hall coefficient is always negative [48].

The second theory proposed to account for the sign reversal in N-type material demands that the electron moves from one bond to an adjacent one, around an odd-numbered ring [36]. But this assumption may not always hold true for non crystalline materials [48]. Mott explained the P-type Hall coefficient for N-type silicon without the need for the assumption of the odd-numbered path [49]. Only considering the scattering centers for the carriers to be the stretched Si-Si bonds and applying Friedman's theory was enough to show the anomalous effect. But

University of Cape Town

for microcrystalline silicon with crystallite sizes as small as 3-5 nm, the normal Hall coefficient was observed which implies that the sign reversal results from a small scattering length [36].

3.6 Hall effect in polycrystalline materials

The difference between single and polycrystalline material is that the latter is made up of large number of smaller crystallites with random orientation. Each crystallite in a polycrystalline material may be regarded as a single crystal but could be of a different size. Each grain meets another at a grain boundary which extends to a few atomic layers with disordered atoms. The presence of grain boundaries in polycrystalline materials makes the electrical property of the material more complicated than in single crystalline material. The disordered atoms at the grain boundary form trapping states which trap the free carriers and make the region free of mobile carriers. The traps become electrically charged as a result, creating a potential barrier that resists the flow of carriers from one crystallite to the next [50]. The potential barrier formed is identical to the Schottky barrier except that the grain boundary is assumed to be two back-to-back-Schottky barriers [51]. The process is shown schematically in Fig. 3.14 for a grain boundary in an N-type semiconductor. The flow of charge across the grain boundaries can happen until the Fermi levels in the grains and boundary are equal. This process will result in the formation of space charge region on both sides of the boundary that is responsible for band bending.

University of Cape Town

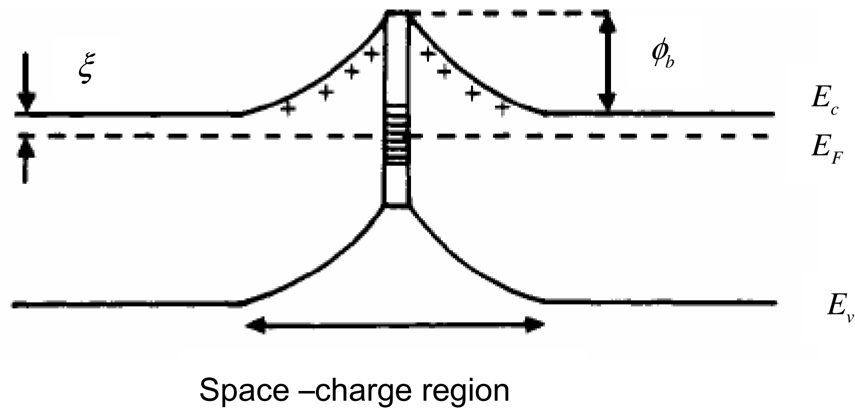

Fig.3.14: Band diagram around grain boundary in an n type semiconductor after Groveno [51]

The model, known as symmetric Schottky barrier, which was observed in grain boundaries of N-type Ge [52] that caused high resistance in either forward or reverse bias mode. However this model may not accurately describe the grain boundaries of all semiconductors [52].

By the virtue of being a disordered region, the states at the grain boundary scatter free carriers, and may also aid the segregation of impurities and dopant atoms [53]. The grain size plays an important role in the electrical property of the material since it determines the number of charge carriers available for trapping at a given grain boundary. The effect can be discussed in comparison with the magnitude of the mean free path of free electron λ. Under normal conditions the mean free path is assumed to be less than the grain size L. For cases in which grain size is less than the scattering mean free path, the carrier concentration determined by the Hall measurement, n, may not be the bulk concentration expected, rather much smaller given by

$$n = n_o \exp\left(\frac{-\phi_b}{kT}\right), \qquad (3.100)$$

University of Cape Town

where n_o is the bulk concentration of the grain. The carrier density and drift mobility are thermally activated but not Hall mobility. For the Hall mobility to be thermally activated the condition $\lambda < L$ should be met.

Seto [50] successfully showed the barrier model to be correct for polycrystalline silicon. His analysis considered a grain size of dimension L, trap density at the grain boundary of N_t / cm^2 located at energy E_t from the intrinsic Fermi level and impurity of one type (dopant) with a density of N / cm^3. The trap density limits the maximum charge that can be trapped. The dopant concentration is also important; for example if the density of trap state is greater than the dopant concentration, all the states of all the grains may be fully depleted of free carriers as a result becoming highly resistive. The functional dependence of potential barrier on doping concentration was demonstrated under different conditions comparing N_t with NL. The first case was when $NL < N_t$, for which the crystallite is completely depleted of free carriers. Under such condition the potential barrier becomes [50]

$$\phi_b = \frac{qL^2N}{8\varepsilon}, \qquad (3.101)$$

where q is a unit charge and ε is the dielectric permittivity of polycrystalline silicon. The potential barrier is linearly related to the dopant concentration. But in the case when $NL > N_t$, the crystallite is only depleted partially, and as a result the barrier potential becomes [50]

$$\phi_b = \frac{qN_t^2}{8\varepsilon N}. \qquad (3.102)$$

Here the potential barrier is inversely related to the doping concentration. From the above two expressions we observe that $N_t = NL$ is a critical value at which the potential barrier starts falling. This gives us a basis to explain the conduction mechanism. Basically the two possible transport mechanisms of carriers across

University Of Cape Town

the grain boundary are the thermionic emission and thermionic field emission (tunneling). Thermionic emission is possible when the carriers possess high enough energy to overcome the barrier. However, there is a probability for those carriers with less energy to pass through the grain boundary by quantum mechanical tunneling. From the above cases discussed the potential barrier attains its highest value for wider barrier in which the thermionic emission is dominant. For the second condition considered, the potential barrier decreases with increasing dopant concentration and thermionic emission dominates. For $\phi_b > kT$, the mobility and conductivity for polycrystalline silicon vary as $\exp\left(\frac{-\phi_b}{kT}\right)$.

As the dimension scales down, for nano sized grains, the process of formation of defects at the grain boundary remains the same. Such situations may be considered as a system with mean free path greater than the grain size.

An alternative transport model was proposed by Weis *et.al*. [54] that unifies the two cases in which the mean free path can be greater or less than the grain size. The model, known as a unified ballistic and diffusive transport mechanism, proved to be in agreement with the thermionic emission model.

3.7 Hall effect in a particle network

A particle network system is an inhomogeneous system, which can be a simple powder or powder mixed in certain medium. In such a system the shape of individual particle, the shape of the contact, the particle distribution (if it is mixed in a medium) affects the Hall effect measurement. The packing density, which is less than the bulk counterpart can also influence the Hall coefficient or other Hall parameters. Percolation models may be applicable to study either the conductivity or the Hall effect. The conductivity σ is given by the relation [57]

University of Cape Town

$$\sigma = \sigma_o (X - X_c)^s, \qquad (3.103)$$

where X is the volume fraction of the conducting material and X_c is the critical percolation limit below which charge transport is not possible.

If we assume an individual particle made up of an aggregate of grains, which makes it polycrystalline, to create a conduction path the particles must form a network. There should be a formation of additional potential barrier at the contact causing the increase in resistance [53]. The conductivity or alternatively the potential barrier between the powder particles depends on the contact size and the percolation path. For two particles of diameter l with a contact area between them of radius a, the effective resistivity of a powder particle is approximated as

$$\rho^* \approx \frac{l}{2a}\rho_1, \qquad (3.104)$$

where ρ_1 is the resistivity of the corresponding bulk material. The Hall effect measurement can be estimated the same way. The effective Hall constant would be the sum of the contribution from individual particles.

The above discussion is based on the condition in which particles are touching each other. But this will not rule out the possibility for the charge carrier movement when the particles are physically not touching each other. There is a probability for the hopping conduction between localized states, in this case individual particles, satisfying the conditions for hopping transport as discussed above.

3.8 Hall effect in composite system

A composite system may be symbolized as system made up of elements with different electrical and physical properties. To conduct the Hall study on such system is a complicated process, and only possible if one applies the multicarrier

University of Cape Town

technique discussed in the above sections. The multicarrier technique or the magnetoconductivity technique is the best approach to estimate the electrical properties of the individual components. The materials on which this work focused are basically composite systems with particles forming networks deposited on paper substrates. Based on the discussion given above, we expect to observe higher resistivity and lower carrier density than the corresponding bulk counterparts.

3.9 Impedance spectroscopy

Impedance is a more general and complex concept quantity than resistance, which takes into account the phase difference between the applied voltage and current [58]. Suppose a signal of $V(t) = V_m \sin(\omega t)$, with an angular frequency ω, is applied to a circuit. A current $I(t) = I_m \sin(\omega t + \varphi)$ will be measured, with a phase difference φ. The impedance is thus defined as the ratio of the applied voltage to the current [58]

$$Z(\omega) = \frac{V(t)}{I(t)}. \quad (3.105)$$

The magnitude of the impedance is given as,

$$|Z(\omega)| = \frac{V_m}{I_m}. \quad (3.106)$$

University Of Cape Town

The phase shift φ assumes different values based on the circuit components and frequencies [59]. For a pure resistance the phase shift is zero whereas for a pure capacitance, the phase shift is $\frac{\pi}{2}$. If a circuit is made up of the combination of resistors and capacitors, the phase shift will be $0 < \varphi < \frac{\pi}{2}$. In complex notation, the impedance can be written as [60]

$$Z = Z' + jZ'', \tag{3.107}$$

where $j = \sqrt{-1}$.

$Z' = \mathrm{Re}(Z) = |Z|\cos\varphi$ is the real component of impedance,

and

$Z'' = \mathrm{Im}(Z) = |Z|\sin\varphi$ is the imaginary component of impedance.

The phase angle can then be given as

$$\varphi = \tan^{-1}\left(\frac{Z''}{Z'}\right), \tag{3.108}$$

and the modulus $|Z| = \left[(Z'')^2 + (Z')^2\right]^{1/2}$. Alternatively in polar form, the impedance is given as

$$Z(\omega) = |Z|\exp(j\varphi). \tag{3.109}$$

Plots in complex planes, with the real component along the x-axis and the imaginary component along the y-axis, are useful techniques to study the charge transport in the bulk or at interface regions. Such plots, which are also known as Cole-Cole plots, [61] also help to deduce an equivalent electrical circuit. The relation between these complex quantities is given as admittance Y, modulus M

University Of Cape Town

or permittivity ε, which are the different expressions of impedance, can also be used to obtain relevant information of the device or material under test.

$$Z = \frac{1}{Y} , \tag{3.110}$$

$$Y = \mu\varepsilon , \tag{3.111}$$

$$\varepsilon = \frac{1}{M} , \tag{3.112}$$

and

$$M = \mu Z , \tag{3.113}$$

where $\mu = j\omega C$ and C is the capacitance in the circuit [62]. In terms of resistive and capacitive reactance components,

$$Z = R_s(\omega) - jX_s(\omega) , \tag{3.114}$$

and

$$Y = G_p(\omega) + jB_p(\omega) , \tag{3.115}$$

where the reactance is $X_s = \left[\omega C_s(\omega)\right]^{-1}$, the susceptance is $B_p = \omega C_p(\omega)$ and the conductance is $G_p = \frac{1}{R_p}$. The subscripts s and p stand for series and parallel connections respectively. Expanding Eqn. 3.115 the expression for admittance [63] is

$$G + jB = \frac{1}{R + jX} = \frac{R - jX}{R^2 + X^2} . \tag{3.116}$$

This can be expressed in terms of ω as

$$G + j\omega C_p = \frac{\left\{R + \dfrac{j}{\omega C_s}\right\}}{\left\{R^2 + \dfrac{1}{\omega^2 C_s^2}\right\}} , \tag{3.117}$$

University of Cape Town

where $C_s = \frac{-1}{\omega X}$ is the equivalent series circuit capacitance. The quantity $C_p = \frac{B}{\omega}$ is the equivalent parallel circuit capacitance. For a circuit with R and C in parallel,

$$Z = \frac{R}{1 + j\omega RC} = \frac{R}{1 + j\omega\tau}, \quad (3.118)$$

where $\tau = RC$ is the relaxation time. In real and imaginary component forms,

$$\mathrm{Re}\{Z\} = \frac{R}{1 + \omega^2\tau^2}, \quad (3.119)$$

and

$$-\mathrm{Im}\{Z\} = \frac{R\omega\tau}{1 + \omega^2\tau^2}. \quad (3.120)$$

Since $\omega\tau = \tan\varphi$, after substitution,

$$\mathrm{Re}\{Z\} = R\cos^2\varphi = \frac{R[1 + \cos 2\varphi]}{2}, \quad (3.121)$$

and

$$-\mathrm{Im}\{Z\} = R\sin\varphi\cos\varphi = \frac{[R\sin 2\varphi]}{2}. \quad (3.122)$$

The imaginary component attains its maximum value when $\sin 2\varphi = 1$, from which φ is determined to be $\frac{\pi}{4}$. The Cole–Cole plot for such a circuit yields a single semi circle whose centre lies on the real axis.

University Of Cape Town

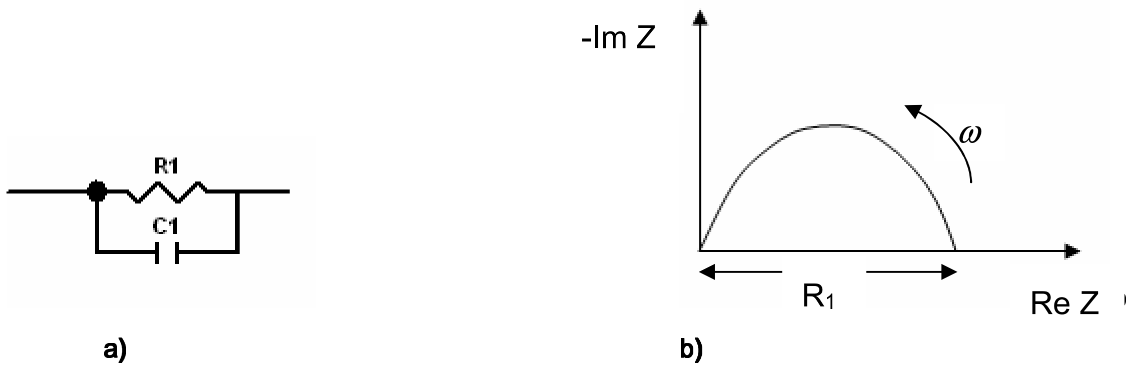

Fig.3.15: a) parallel RC circuit element, and b) the corresponding Cole–Cole plot.

As demonstrated in Fig. 3.15 one semicircle represents one parallel RC circuit element, and its diameter is equivalent to the resistance. The frequency changes from minimum to maximum as indicated by the arrow. At the minimum and maximum frequencies the imaginary component approaches zero. If, in the circuit there is a series resistance with RC parallel, the semicircle is displaced along the real axis by the magnitude of this resistance.

University Of Cape Town

4 Powder and Layer Production

4.1 Powder production

The two major routes of producing nanopowders were described in the earlier discussion as top-down and bottom-up. In this work we have used powders produced in both ways: by the mechanical attrition of bulk silicon and by laser pyrolysis from a silane gas precursor. The powder produced by laser pyrolysis was obtained from a commercial supplier, MTI Corporation, Richmond California. This powder had a nominal particle size of 50 nm. Its purity was specified as > 98% on shipping, with the only detectable impurity being oxygen.

University of Cape Town

Mechanical attrition was performed in house using different bulk silicon feedstocks. During the milling process the coarse-grained powder is fractured to a finer structure as a result of severe plastic deformation. The particle size distribution, the microstructure and the level of contamination can all be attributed to the choice of mill and its process parameters. The following are some of examples of choices which can influence the final powder [1-3]:

- the type of mill used (*eg.* attritor, planetary, centrifugal, vibratory or tumbling mills). Different mills have different capacity, different operation speed and operation conditions.
- the density of the milling medium (*eg.* hardened metal, ceramics tungsten carbide). A denser milling medium causes a stronger impact on the particles.
- the power of the mill (*eg*. high energy or low energy mill).
- the milling media-to-powder weight ratio, regardless of the shape of the grinding bodies A higher ratio yields smaller crystallites faster.
- the milling time.

- the material of the milling media used to perform the milling. In most cases it is the primary source of contamination.
- the amount of the material being milled.

However, it is difficult to say that any of these variables is independent, rather they are interdependent.

The starting materials were obtained from local and international suppliers. Bulk 2503 grade silicon metal was supplied by Silicon Smelters (pty.) Ltd., Polokwane, South Africa, and P- and N-type high purity silicon wafers were commercially obtained from Siltronix AG, Munich, Germany.

University Of Cape Town

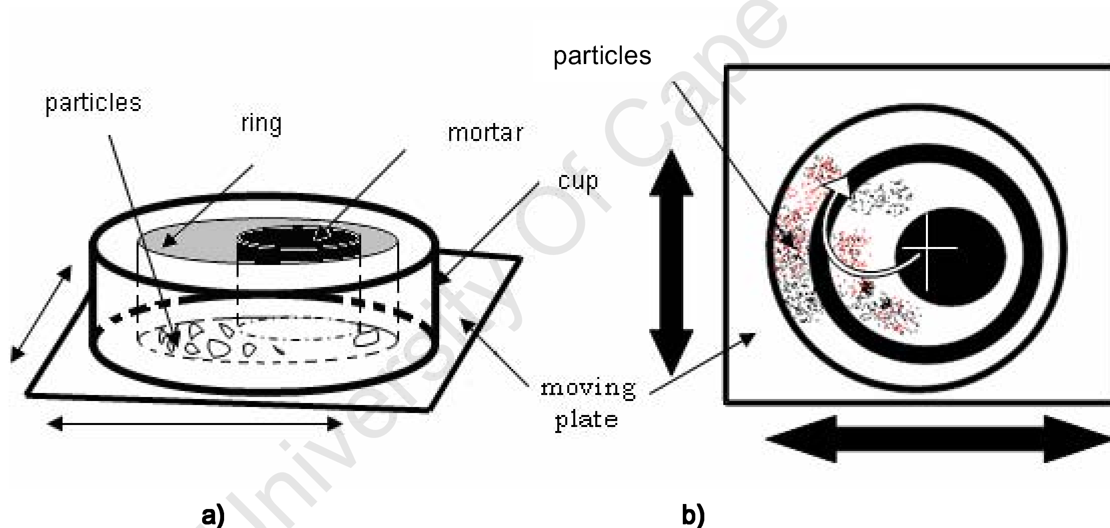

Fig. 4.1: Schematic of the high energy orbital pulveriser: a) side view and b) top view. The black double arrows show the direction of motion of the plate and the single white arrow the resultant relative motion of the milling media.

According to the manufacturer's analysis, the purity of the metallurgical grade silicon is 99.4 %, with the main impurities being Fe at 0.21 % and Al at 0.144 %. Other specified impurities were Ca, Ti, Cr, P, and Ni with concentrations, in ppm,

of 230, 129, 62, 43 and 18 respectively. As received, the silicon metal had an average particle size of about 10 mm which had to be reduced to the nano or submicron level. The N- and P-type materials were single crystalline wafers doped with antimony and boron respectively. Both were Czochralski grown wafers of diameter 4-inch and nominal purity 99.99%.

For milling, an 800 W Siebtechnik laboratory orbital pulverizer (Scheibenschwingmühle), equipped with 52100 chrome steel pestle and mortar was used [4]. This is a high energy vibratory mill. The schematic given in Fig. 4.1 shows the motion of the mill and the position of the particles between the hardened metal components. Photographs of the milling media are also given in Fig. 4.2 to illustrate the actual components used. Two sets of media have been used for the milling process. The first set, system 1, is the type used to mill metal grade silicon, shown in Fig. 4.2 a). There are two moving components, the pestle and the ring, in the cup. The second set, system 2, is the type indicated in Fig. 4.2 b), in which there is only one moving pestle in the cup. It was mainly used to mill smaller quantities of silicon wafers. The dimensions for the two systems are presented in Table 4.1. The cup with the pestle, or pestle and ring, inside is clamped onto the moving plate. The cup is therefore held in a fixed position relative to the moving plate, whereas the ring and the pestle can freely move in the cup. As the mill is engaged, the moving plate starts to vibrate in the horizontal plane. The cup and the moving plate always move together, but their motion is in the opposite direction to the relative motion of ring and the pestle. Acquiring motion in opposite direction ensures the maximum impact between the colliding bodies. In the process, the particles trapped between the colliding grinding elements sustain heavy impact which results in their fragmentation to smaller pieces. This process is accompanied by a compaction which involves elastic and plastic deformation of particles. Further action eventually leads to further fragmentation [5].

University of Cape Town

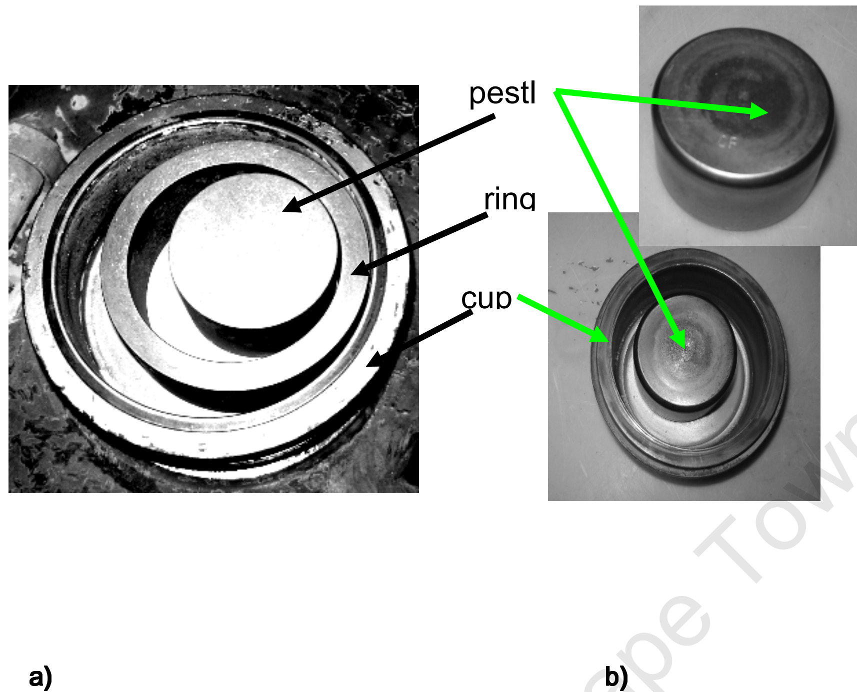

Fig. 4.2: The two milling systems used to produce powder a) system 1 and b) system 2.

The compaction and fragmentation will not continue indefinitely. The fineness of the powder approaches a milling limit, where no further reduction in size is possible. There are different reasons for the milling limit, the strong cohesive force responsible for agglomeration, surface roughness of the milling medium, excessive clearance between impacting surfaces and the bridging of larger particles shielding smaller particles from facing the impact [5].

University Of Cape Town

Table 4.1: Dimensions of the milling meda of the two systems.

Components	System 1	System 2
Cup	Diameter (inner) = 139 mm Depth = 48mm Mass = 2523 g	Diameter (inner) = 80 mm Depth = 37.1 mm Mass = 1045 g
Pestle	Diameter = 75 mm Height = 45.6 mm Mass = 1525 g	Diameter = 54.9 mm Height = 32.6 mm Mass = 575 g
Ring	Diameter (inner) = 94 mm Diameter (outer = 120 mm Height = 45.2 mm Mass = 1454 g	==

University Of Cape Town

In Fig. 4.1, the direction of motion of the milling medium holds for both systems. The powder to milling medium ratio most commonly used is 1:10 [6]. This is an important parameter for attaining a specific size reduction and size distribution in a given time. In our case, for both systems the ratio was about 1:60. The higher this ratio is, the shorter the time required to attain a fine powder. However, if such high ratio is accompanied by higher energy, it will increase the number of defects in the powder grains. In extreme cases, complete amorphisation can occur [6].

Mechanical attrition is known for its high level of contamination [7, 8]. Contaminants may be imparted from impurities in the feedstock and the wear of milling medium [7], but also from residue in the cup and on the milling medium, and from the atmosphere. Effort was made to keep the level of accidental

contamination to the minimum possible. This was achieved by thorough cleaning procedures. Before commencing milling the silicon, silica (sand) was milled for about 10 minutes, to ensure the removal of any residual contaminant remaining from the previous milling. Afterwards, the milling components such as the cup, the pestle, the ring, and the top cover were washed thoroughly with ethanol.

Using system 1, 50 g of metallurgical Si was dry milled in air five times, with each session of duration of one hour. Between each session there was a break of approximately ten minutes. This procedure was adopted to protect the system from overheating. The milling process took place in an ambient laboratory environment, without any special control. The temperature build-up during milling was monitored with a thermocouple and noted to reach as high as 162 ^{0}C over an hour of milling time. Likewise, the cooling trend was monitored to be an exponential decay as shown in Fig. 4.3.

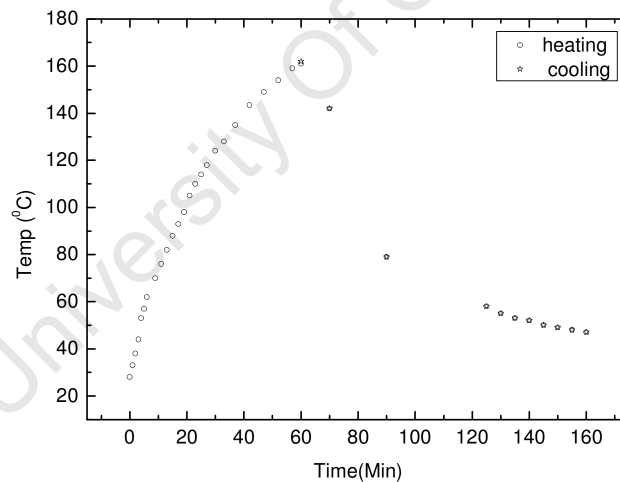

Fig.4.3: The temperature rise and fall, during and after milling with system 1.

The heating and cooling curves were fitted to an exponential growth and decay respectively to extract the time constants. For the temperature build up, the time constant was determined to be (29 ± 1) s, whereas for cooling it was (29 ± 4) s.

University Of Cape Town

The same cleaning procedures were followed to mill wafers using the second set, system 2, of milling media. Unlike system 1, there are four cups with their corresponding pestles to be loaded simultaneously. We have used only one cup for the milling of typically 5 g of Si wafers broken down to about 1 cm, filling the other three with an equal mass of silica to keep the machine balanced. To avoid the possibility of cross contamination, either only P-type wafer or only N-type wafer was milled at a time. The milling duration was again performed five times, with each session of duration of one hour. Between each session there was a break of about 15 minutes. Moreover, it was observed that, unlike the case of system 1, during this process there was only a small rise in temperature.

4.2 Printing methods

Two different methods of sample printing were used in this work. Manual printing was the method used to produces most of the samples. The second technique was screen printing. In principle both methods can be said to be similar since both operate on the stencil printing principle, in which the ink passes through open areas of a mask or stencil. But practically, the properties of ink required for the manual print are quite different from those required for screen printing. The requirements of the ink for each case are presented in the next subsections.

4.2.1 Hand printing

In the manual print process, shown in Fig. 4.4, the substrate is masked off to form a design and a glass rod is used to spread the ink. The manual print was introduced due to its simplicity for the quick test of the printability of inks. It was introduced as a preliminary testing step before commencing full scale automated screen printing. Figure 4.4 a), shows the first step in which the glass rod is used to push the ink over the region masked with tape only exposing the area to be printed. In Fig. 4.4 b), the ink covers the entire region including the mask. As

University of Cape Town

indicated in Fig. 4.4 c), which is the last step, removing the mask reveals the print of the design on the substrate. Manual printing was also used to produce plain layers directly on the substrate without the use of a mask.

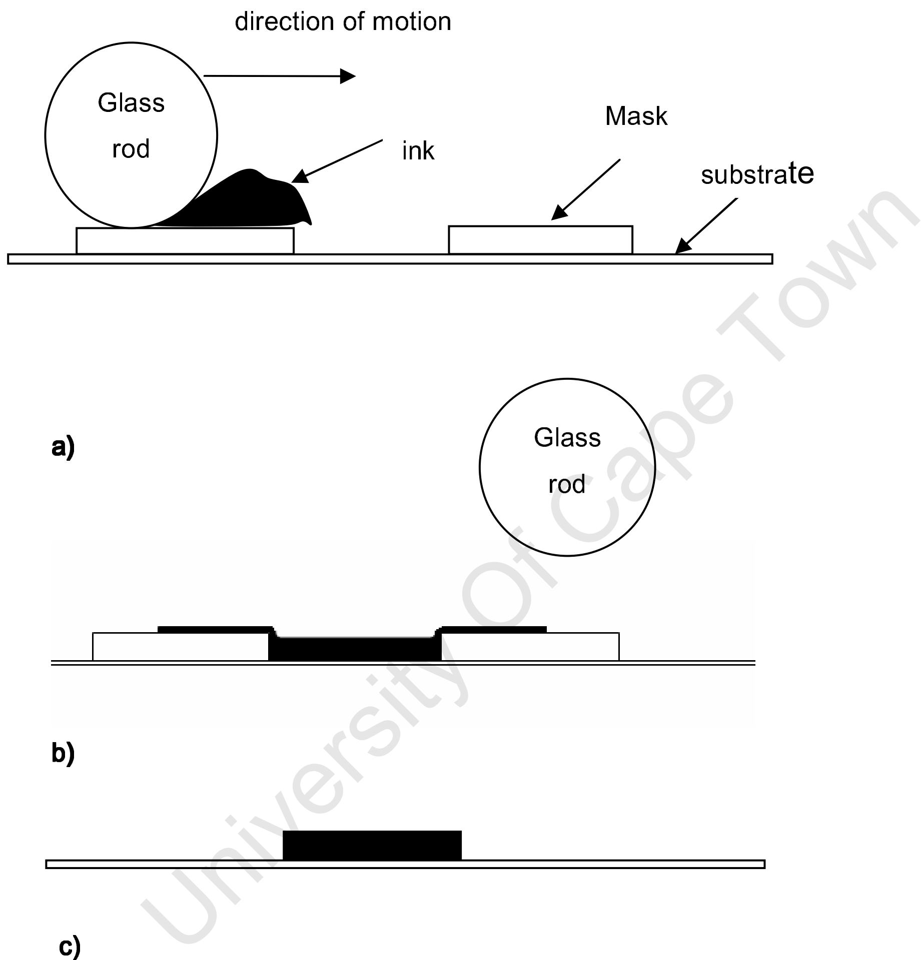

University of Cape Town

Fig. 4.4: The sketch to show the process of manual printing of sample layers: a) first step in the process of hand printing through masked stencil; b) second step the glass rod pushed the ink and is filled the open region; and c) the last step, the silicon layer appearance when the mask is removed.

4.2.2 Screen printing

The processes in screen printing, from stretching the screen on the frame to printing the design on the substrate, can be discussed briefly as follows. The screen is an important component of the screen printer. Nowadays it is made from synthetic materials such as polyester, but historically it was prepared from silk. That is why synonymously we use the terms silkscreen printing and screen printing. The polyester screen is stretched over a rigid frame and coated with negative photoresist from both sides. The design of interest is normally printed full size on a transparency. The transparency with the design is placed on the screen and exposed to light.

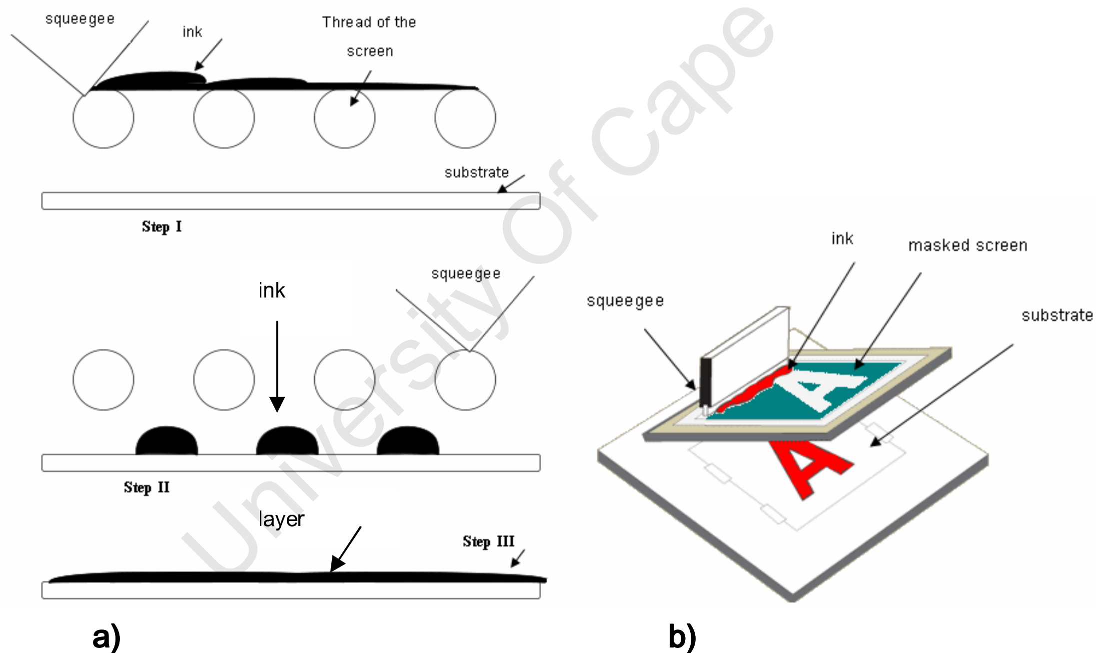

Fig. 4.5: a) the cross-sectional view of a screen to demonstrate ink flow steps, and b) image printing with screen printer [9].

Exposure is from the design side so that the design casts a shadow on the screen. Over the exposed region, the photoresist polymerises and blocks the screen. Washing the screen with water afterwards removes photoresist from the

University Of Cape Town

unexposed region. Figure 4.5 demonstrates the steps and components used in the screen printing process.

The quality of the print can be influenced by the mesh size of the screen and the tension used to stretch the mesh. Mesh size means the hole in the fabric that the ink passes through shown in Fig. 4.6. The higher the line density is, the smaller will be the mesh size. Small mesh size guarantees better resolution. But as the mesh size becomes smaller, it is more difficult to force the ink through it. It is advisable to know which mesh to use for which ink. The tension can also affect the print quality. If the tension exceeds a certain limit the mesh opening can be distorted. When the tension is low, a uniform print may not be achieved. In such cases the ink will flow towards the centre rather than lying on top of the screen.

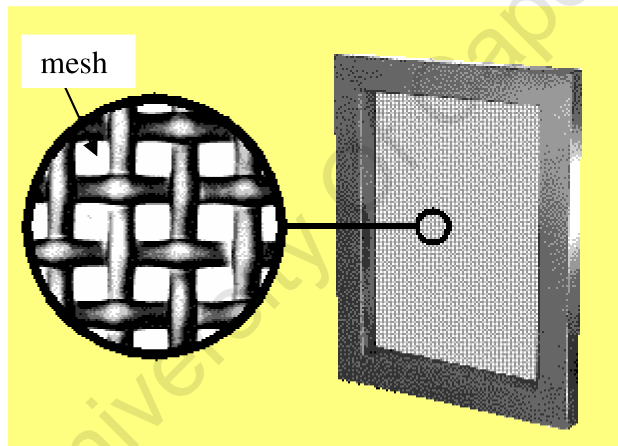

Fig. 4.6: The threads in the screen showing the mesh size [10].

The squeegee is one of the important components of screen printing. Its purpose is mainly to push the ink through the opening of the mesh onto the substrate, but it also pushes excess ink to the edge of the screen [11]. The hardness of the squeegee can influence the print quality. A soft squeegee can alter the set angle of attack by flexing during printing. The rheology of the ink, the type of substrate, the squeegee speed, and the squeegee pressure, the snap off distance for off-contact prints, the angle of attack, and the amount of flooding ink can also affect

University of Cape Town

the print quality [12]. Most of these parameters are interdependent, and hence make the screen printing process complex.

4.3 Ink properties

4.3.1 Rheological properties of ink

Rheology may be defied as the study of the flow behaviour of matter under the action of a stress [13]. The resistance of the flow of fluid under the action of stress describes an intrinsic property called viscosity which helps to categorize fluid as Newtonian and non-Newtonian. In a Newtonian fluid the viscosity is constant and independent of the applied stress. For a non-Newtonian fluid, viscosity may increase or decrease with the applied stress. When the viscosity decreases with increasing shear stress, the effect is called shear thinning or pseudoplasticity, but if viscosity increases with increasing shear stress, it is called shear thickening or dilatancy. In pseudoplastic or dilatant fluids the viscosity is time independent. When shear thinning is time dependent, it is known as thixotropy [14]. The viscosity of such an ink decreases with time for a constant applied stress. For a given strain rate, it therefore requires a finite time to reach its equilibrium viscosity, which is an important property for printability. The reverse phenomenon to thixotropy is known as rheopexy [15].

University of Cape Town

Surface tension is also an important parameter that influences the printability of the ink. It is defined as a tangential force that keeps a fluid together at an interface [16]. The cohesive forces that are present between the atoms and molecules, or even between different phases of the ink give rise to surface tension. When ingredients such as solvents or surfactants are added, these cohesive forces are changed, resulting in a change of surface tension. Thermodynamically surface tension is described as the surface free energy [17], which is the energy required to create a unit area of interface. Hence the

adhesion of the ink to a substrate can be explained in terms of the free energy of the interfaces. If the free energy of the liquid ink surface is greater than that of the interface to the substrate, printing is not possible. But, if the surface free energy of the ink is less than that of the interface with the substrate, adhesion of the ink to the substrate is possible. Figure 4.5 shows the forces acting on the drop of ink on substrate. In terms of these forces the condition for printability is given as

$$\gamma_{sa} + \gamma_{la} > \gamma_{sl} \,, \tag{4.1}$$

where γ is the interfacial tension, with the subscripts sa denoting the interface between the substrate and air, la between liquid and air, and sl between the substrate and liquid.

There are many different techniques [18] to measure the surface tension for a given ink, of which the contact angle technique is the simplest. Figure 4.5 shows the definition of the contact angle θ, which is the angle between the substrate and the tangent to the surface of the drop.

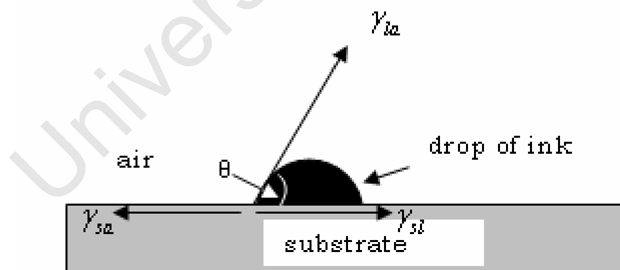

Fig. 4.5: The combination of interfacial forces that determine the contact angle.

The surface tension and contact angle are related through the balance of horizontal forces as [19]

University of Cape Town

$$\gamma_{sa} - \gamma_{la}\cos\theta = \gamma_{sl} \,. \tag{4.2}$$

For inks or substrates with high surface energy, the contact angle can be up to 180° [19]. However, in general an ink with a high contact angle will not wet the substrate, and will therefore, in general, not be printable. For a low contact angle, the ink wets the substrate, and such an ink is printable. But if the contact angle is too low, which is the condition for complete wetting, the ink spreads too much resulting in poor edge definition. Such low contact angles may also not be easy to measure. Hence it may be necessary to choose a different substrate, for which it is possible to measure the contact angle, and then optimize for the substrate used in the printing.

4.3.2 Requirements for hand printing

For manual printing, using an open stencil, the ink should generally behave as a Newtonian liquid, with a constant viscosity. Linseed oil, which is a Newtonian liquid with intermediate viscosity, was a good choice of binder. Even though the rheology of the ink has to be adapted according to the substrate used, generally less viscous inks provide better coverage.

4.3.3 Requirements for screen printing

The rheology of the ink used for screen printing is different from that for manual printing. The ink should be thixotropic with intermediate viscosity. A highly viscous ink will be difficult to pass through the mesh of the screen. If the viscosity is very low, the ink can run through screen and spoil the image design. The ink also should stay wet during long print runs or during longer working time. A quick drying ink can block the screen mesh and makes cleaning difficult. Adhesion is also an important parameter for the ink, both to the paper substrate and between

University of Cape Town

particles. Having these factors in mind, the ingredients to formulate a well printable ink were identified.

Figure 4.5 a) illustrates the importance of thixotropy and shear thinning in the screen printing process. In step I, as the squeegee acts on the ink, the shear stress applied by the squeegee makes the ink less viscous. Consequently the ink passes to the substrate through the opening between the threads. Step II demonstrates the situation immediately after the removal of the acting stress. Drops of ink are placed on the substrate alternately with empty spaces underneath the thread. For a thixotropic ink the restoration of its static viscosity takes a finite time. Therefore, during this time, the ink can flow to fill the empty regions resulting in the continuous layer shown in step III.

4.4 Ink formulation and mixing

All the electrical characterisation was carried out on layers of a composite system of silicon layers printed mainly on paper, but also on plastic, substrates. The silicon inks used can be grouped into two systems. The first group is a mixture of nanoparticulate silicon and polymeric binder, whereas the second group is a mixture of nanoparticulate silicon, polymeric binder and a dopant (inorganic salts). Different amounts and different types of salts were used in the composites to study the correlation between electrical parameters and salt quantity and type. All the binders used for this purpose are soluble in most organic solvents, such as acetone, lacquer thinners or chloroform. The selection of the dopant inorganic salts was mainly based on their environmental stability. Samples produced from the mixture of silicon and a salt will be referred to as doped samples.

University of Cape Town

4.4.1 Oil based inks for manual printing

The following steps were followed to produce doped ink for manual printing. Each time a defined quantity of Si nanopowder, 1.00 g for milled Si and 0.4 g intrinsic Si, was placed in different clean plastic bottles. Then the dopant inorganic salt in a required weight-percentage to the powder (2%, 4%, 6%, 8% etc) was added to the powder placed in each bottle. Just enough deionized water was used to make a solution of the salt and silicon powder. To attain homogenous mixture, it was first stirred, manually with a spatula or using a Fisons Whirlmixer, for about three minutes, followed by sonication in an ultrasonic bath. The solution was then dried at 60° C until the water had completely evaporated. The next step was to prepare printable ink by adding linseed oil, as a binder, and the solvent. For the milled powders, 500 µl of oil and 3 ml commercial lacquer thinners as a solvent, were added to each bottle. Because of the lower mass and apparent density of the intrinsic Si powder, only 200 µl oil was added but a larger volume, 4.5 ml, of solvent was used. The mixture was stirred manually using a stainless steel spatula for about five minutes until all the lumps were broken down, before sonicating for 30 to 60 min.

University of Cape Town

4.4.2 Acrylic inks for screen printing

For screen printing, acrylic emulsion supplied by Marchem Screen Printing Supplies, Cape Town, South Africa, was used as a binder, with propylene glycol as a solvent. The choice for propylene glycol as a solvent was due to its low volatility and hygroscopic property, which helps to keep the ink wet for a prolonged print time.

The process of ink production can further influence its properties. For example, if an acrylic is mixed ultrasonically, there is a possibility of breaking the emulsion and triggering polymerization. Therefore, the ink was mixed manually to a

smooth paste and then thinned down to the right viscosity. To make a batch of ink, 1.25 g of binder and 5.00 g of silicon powder were weighed in separate containers. A spatula was used to add the powder sequentially to the bowl containing the binder. The powder-binder mixture was stirred thoroughly with the spatula. Mixing was continued by adding one spatula of powder every two to three minutes. Glycol solvent was added as required, little by little. Thorough mixing yielded a smooth paste which was later thinned by adding more glycol. In total about 2.2 ml of glycol was used to thin the ink. The contact angle measurement was a method used to determine the quality of the ink. A clean glass substrate was used to optimize the contact angle for the ink to be screen printed on paper substrates. Accordingly the optimum range of contact angle θ, was found to be between 50º and 60º. The ink produced was observed to be thixotrophic, with a relaxation time of several seconds.

4.5 Printing procedures

Under this section a brief description of the actual printing procedures will be presented. The presentation will be split into two sub-sections, describing firstly manual printing and secondly the procedures for screen printing.

4.5.1 Manual printing

Two approaches were followed in the printing process. The first was to print a layer of ink on a plain substrate using a glass rod as described above section 4.2.1 while the second was to print silicon ink onto a paper substrate with silver metal contacts previously printed on it. To reduce the possibility of contamination, gloves were always used while printing and generally while handling the samples. All materials that were used for the printing such as the spatula and glass rod were thoroughly cleaned with acetone beforehand. Before starting the printing the ink was stirred thoroughly to attain a uniform dispersion. As indicated

University Of Cape Town

in Fig. 4.6, a glass rod of diameter 5 mm was used to spread the ink with a stroke length of about 30-40 mm. In most cases the prints were bi directional, to and fro, with two strokes in each direction, to ensure the uniformity of the deposited layers.

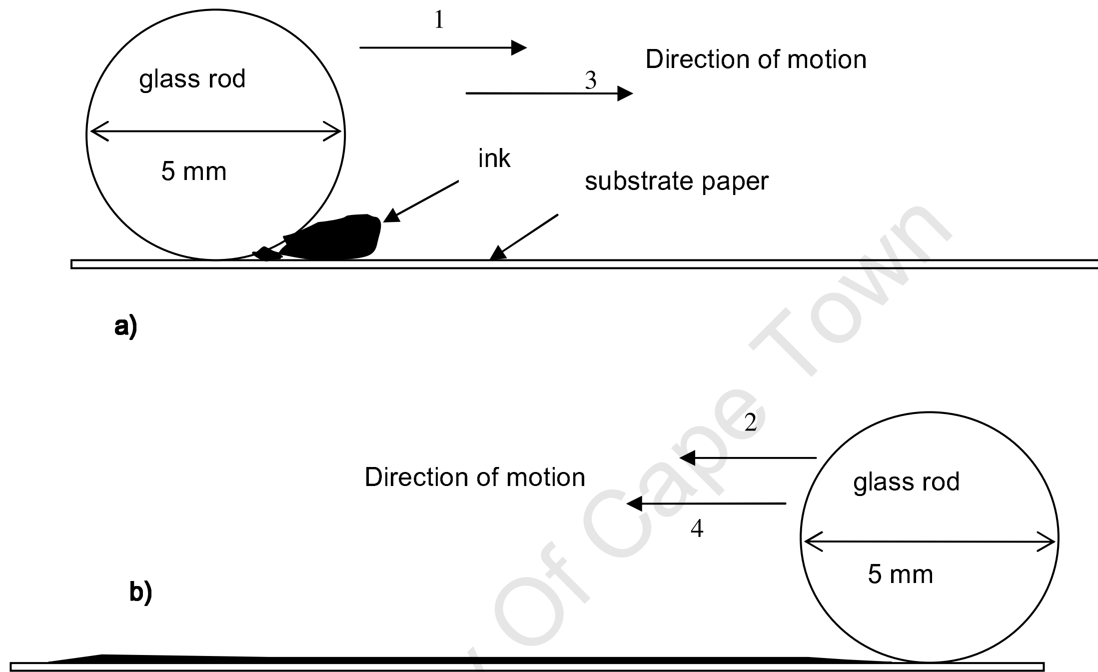

Fig. 4.6: The steps of silicon layer printing on plain paper: a) the starting condition and b) the final condition. The numbered arrows indicate the stroke order.

University Of Cape Town

4.5.2 Screen printing

Two models of Screen Printer were used during the course of this work. The first was a vintage AMI-PRESCO 645 semi-automatic Screen Printer with an effective print area of about 3 in. x 3 in. It was mainly used to print silver metal contacts on paper substrates and on hand printed silicon layers. The attempts made to print oil based silicon ink were not successful. The screen was stretched to a tension of 18 – 20 N/cm on an aluminium frame of 8 in. x 10 in. Stretching and related screen processing was carried out by Register Screen (Pty) Ltd, Cape Town,

South Africa. A polyester screen of 120 lines per cm and thread thickness 35 μm was used. The resulting mesh opening was about 50 μm which gave a very good resolution. All the printing was performed in off-contact mode, in which the screen only makes contact with the substrate when the squeegee applies pressure.

The second and new printing machine, an ATMA model AT60PD, has many advantages over the old one. It has wider effective printing area that allowed the use of A4 sized paper as a substrate. Parameter settings for movement are digital with high precision. Registration can be attained using micrometer screwgauges with a precision of about 100 to 500 μm, whereas the squeegee speed can be set within 1mm per second. A screen of 150 lines/cm with a thread thickness of 31μm was used. Stretching and related screen processing was also carried out by Register Screen. A procedure known as 'one and one plus one' was used to apply the photoresist. In this method first both sides of the screen are coated. When dry, a third layer is applied on the print side of the screen to provide a uniform stencil thickness and good edge definition. The tension after stretching was between 22 and 25 N/cm, which was found to be an optimum tension for the print quality. The resolution of the screen given by the mesh opening was about 35 μm.

4.6 Sample production and description

A picture of a manually printed sample with top contacts is shown in Fig. 4.7. As a substrate material mainly 80 g m^{-2} bond paper, produced by Mondi South Africa Ltd., was used. Only in very limited cases photocopy transparency sheets were used. The thickness of the deposited layers was not the same for all the inks. For intrinsic silicon based inks it was about between 1o and 20 μm as determined by a micrometer screw gauge. Thick layers of intrinsic silicon were susceptible to cracking. For inks containing milled silicon (metallurgical, N- and P-type silicon)

University of Cape Town

cracking was not a problem. The thickness of milled silicon layers was about 50 µm. After printing, the layers were allowed to cure in ambient conditions. After drying, the silicon ink coated paper substrates were cut to a size maintaining the minimum aspect ratio 3:1 which is a requirement for Hall bar samples [20]. After mounting on a thick card base, electrical contacts were made using Du Pont 5000 silver conductor. The samples were then kept for two to three days under ambient conditions for the metal ink to cure before starting any measurement.

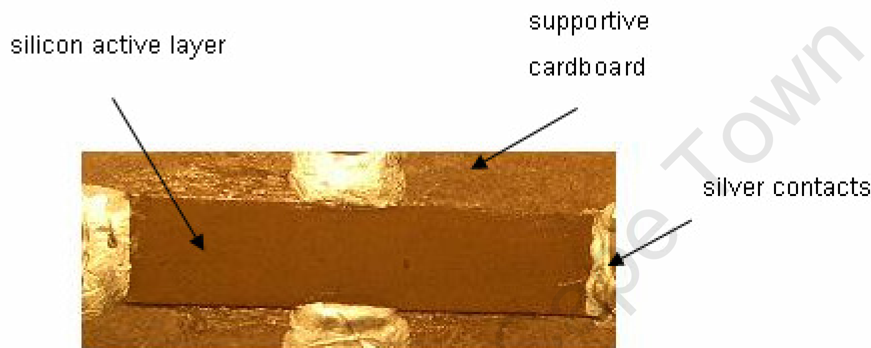

Fig. 4.7: Manually printed Hall bar structure from silicon layer

University Of Cape Town

The second approach to manual printing was to deposit a silicon layer in the correct format directly on a substrate with previously printed silver contacts. The contacts on these substrates were screen printed using an AMI-PRESCO 645 screen printer and stored in a clean environment before printing the silicon layer. Figure 4.8 shows the metal contact structure for a single Hall device with the mask used for printing the silicon in Fig 4.8 b). The dark region represents the metal contacts.

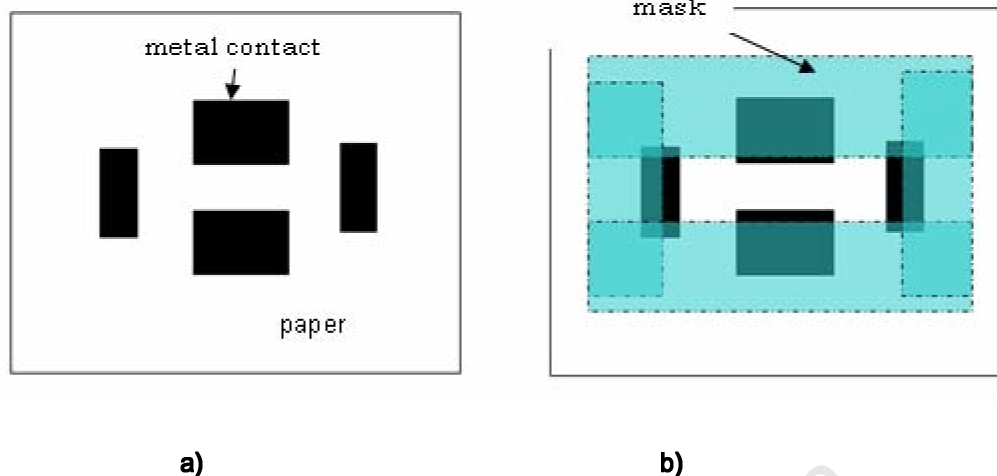

a) **b)**

Fig. 4.8: A sketch of a substrate with pre-printed metal contacts a) before and b) after masking.

The ink is only deposited over the unmasked open area. To ensure contact between the silicon and silver layers, the edges of the metal contacts were exposed. The printing steps are as described above and shown in Fig. 4.4. For each device structure about 0.1cm^3 to 0.2 cm^3 of ink was placed at one end of the masked region using a spatula. The ink was then spread over the substrate using the glass rod as described. The ink was spread with double strokes in two perpendicular directions. The effective dimension of the Hall bar is approximately 3 mm by 10 mm, consistent with the dimensional requirements discussed in chapter 3. The thickness of the layers was about 50 μm as measured with a micrometer screw gauge. After the print was made, the layers were kept under ambient conditions to dry before removing the mask. Each device was then pasted onto a supporting board for characterisation.

University of Cape Town

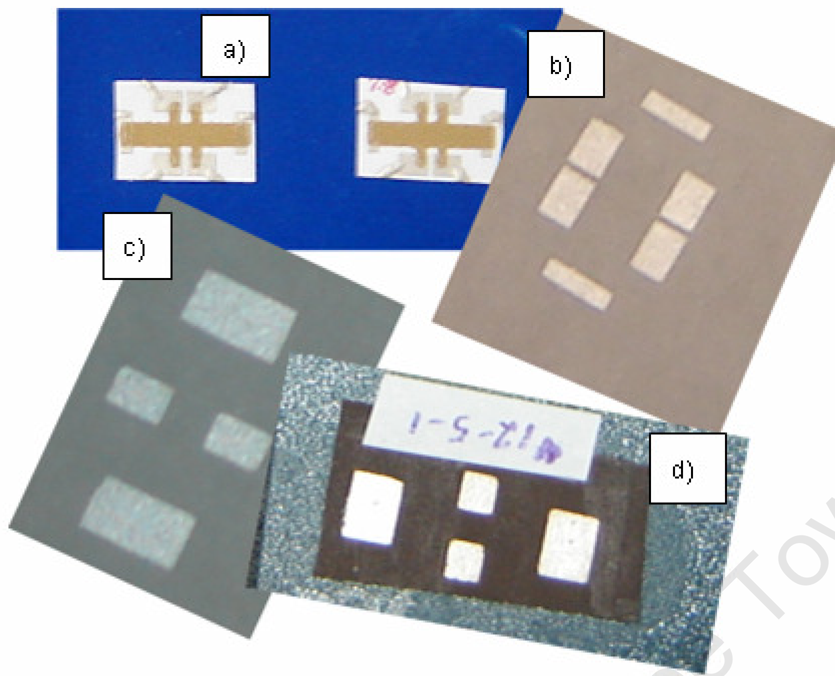

Fig. 4.12: Designs printed by AMI-PRESCO 645 screen printer: a)shows the print attempt of Hall bar of intrinsic silicon with six contacts; b) and c) the metal contacts printed on paper for Hall bar structure with six and four contacts respectively; and d) is metal contacts printed on hand printed silicon layer.

University Of Cape Town

Figure 4.13 shows the screen with multiple designs used with ATMA-AT60PD screen printer. The bright regions are the open areas through which the ink passes to the substrate. The designs are metal contacts for solar cells, transistors and Hall samples. The prints from the screen given in Fig. 4.13 were used as substrates for the printing of subsequent silicon layers. What is presented in Fig. 4.13 is just one example of different structures used for the Hall effect measurements.

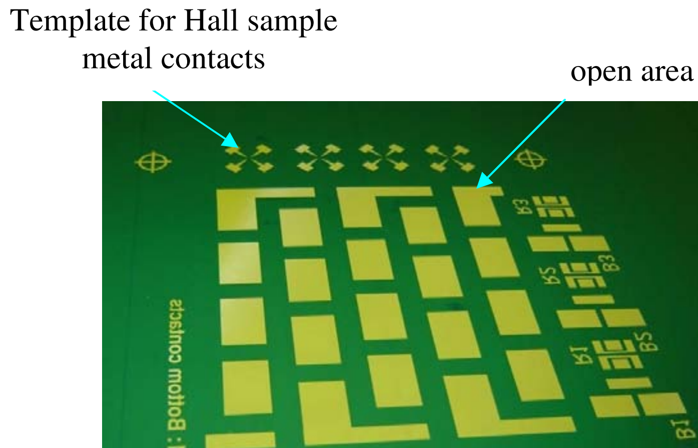

Fig.4.13: Picture for one of the screen used to print metal contacts

University of Cape Town

Generally both screen printers were used to produce samples with different geometries for both the van der Pauw and Hall bar measurement set-ups, as shown in Fig 4.14. The van der Pauw geometry had the following versions: Greek-cross, clover-leaf, circle and square shape, whereas the Hall bars had a classic rectangular shape with either four or six contacts.

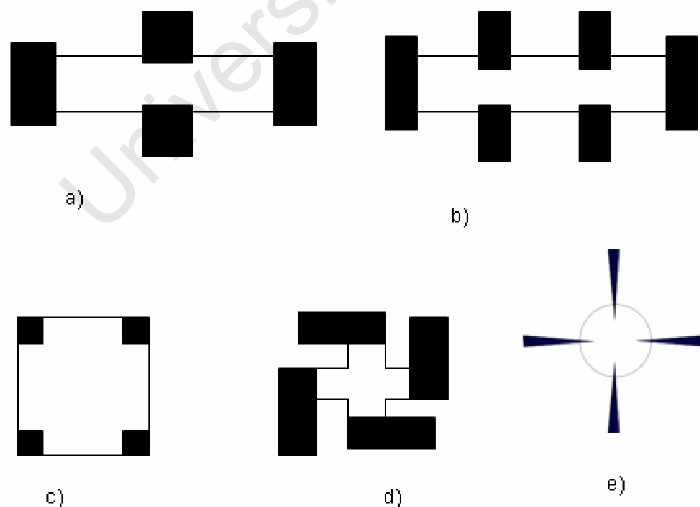

Fig. 4.14: The structures used for the electrical measurements: and b) are for the Hall bar geometry, whereas c), d) and e) are for the van der Pauw geometries.

For all Hall bar sample geometries, the dimensional requirement of a minimum aspect ratio was maintained. For example for the geometry given in Fig. 4.14 a), the width of the layer should be about a third its length. For the van der Pauw geometry, even though any arbitrary shape is possible, square shapes are most commonly used. The samples produced for this geometry were mainly square in shape but of different dimensions. Samples which were characterised were with dimensions ranging from ~10 mm x 10 mm to ~3 mm x 3 mm. Structures with Greek cross and circular shapes, shown in Fig. 4.15 were also used. The circular structure was printed with the screen template shown in Fig.4.13.

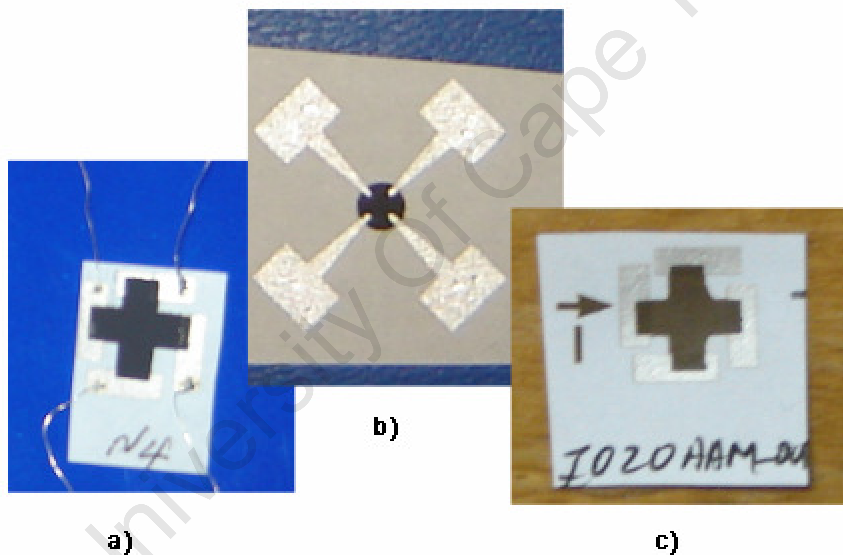

Fig.4.15: The complete Hall devices in a) & c) Greek-cross, b) Clover structures. The edge definition of the print in device c) was not good.

University of Cape Town

5 Experimental Techniques

5.1 X-ray diffraction

X-ray diffraction is a non-destructive technique used to the study the structure of crystalline and non crystalline materials. X-ray diffraction from crystalline planes is observed only if Bragg's conditions are fulfilled [1]. According to Bragg's assumption when an infinite crystal is subject to monochromatic X-rays, diffraction only occurs at an angle 2θ, if the path difference between the rays reflected from the successive planes is an integral multiple of the wavelength. Mathematically Bragg's diffraction condition is given as [2]

$$2d\sin\theta = n\lambda \, , \tag{5.1}$$

where n = 1, 2, 3, …

λ is the X-ray wavelength,

d is the distance between lattice planes, and

θ is the Bragg angle.

In the ideal case diffraction from all planes leads to constructive interference at a unique angle. This is only possible only for an infinite crystal. Practically there is no such perfection, and this causes the broadening of the diffraction peak.

Applying Scherrer's formula [3], it is possible to estimate the grain size of a polycrystalline material. If we let b be the full width at half maximum (fwhm) of the diffraction curve in radians and D be the grain size,

$$D = \frac{k\lambda}{b\cos\theta} \, , \tag{5.2}$$

where k is a constant satisfying $k \le 1$. Hence the grain size is inversely proportional to the width of diffraction curve.

University Of Cape Town

Max von Laue formulated an equivalent theorem to Bragg's diffraction law in an elegant way by only considering the periodicity of atoms in a crystal and elastic scattering [4].

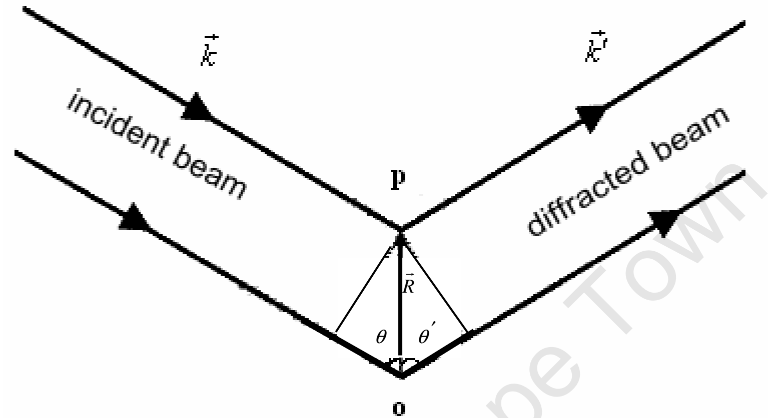

Fig.5.1: Scattering from electron at points o and p.

University of Cape Town

Figure 5.1 shows the situation in which an incident wave of wavevector $\vec{k}$ impinging on scattering centres at points o and p separated by a lattice vector $\vec{R}$. In the process the scatterers act as a sources of secondary waves forming the diffracted beam with wavevector $\vec{k}'$. The path difference between the scattering points is given as $R\cos\theta + R\cos\theta'$. Constructive interference happens if the path difference is equal to $m\lambda$, where m is an integer. Therefore

$$m\lambda = r\cos\theta + r\cos\theta' . \tag{5.3}$$

If we multiply Eqn. 5.3 by $\frac{2\pi}{\lambda}$,

$$2\pi m = \vec{R}\cdot(\vec{k}-\vec{k}') = \vec{R}\cdot\vec{q} , \tag{5.4}$$

where $\vec{q}$ is the scattering vector, standing for the difference in wave vector on scattering [4]. Equivalently Eqn. 5.4 can be expressed as

$$e^{-i\vec{q}\cdot\vec{R}} = 1 . \qquad (5.5)$$

But from the definition of reciprocal lattice we have

$$e^{i\vec{G}.\vec{R}} = 1 , \qquad (5.6)$$

where $\vec{G}$ is a vector of the reciprocal lattice.

Comparing Eqns. 5.5 and 5.6, we can show that the Laue condition for constructive interference occurs only if the scattering vector is equal to a reciprocal lattice vector, *ie*

$$-\vec{q} = \vec{G} \ , \qquad (5.7)$$

which is equivalent to $\vec{q} = \vec{G}$.

X-ray diffraction was carried out using facilities at iThemba LABS, Cape Town, South Africa and in the Chemistry Department of UCT. At iThemba LABS a Bruker AXS D8 Discover diffractometer, with Cu Kα radiation was used to characterize powder samples of N-type, P-type and intrinsic silicon. The P- and N-type powders were milled for forty minutes, whereas the intrinsic powder was used as received from the supplier. The diffraction pattern was measured over a two theta range of 10 to 85^0 in steps of 0.02^0.

The XRD facility at the Chemistry Department of UCT is a Huber G670 Guinier imaging plate X-ray diffractometer. The diffractometer has a 2θ range of 4 - 100º in intervals of 0.05º, and uses X-rays of wavelength $1.5405A^o$. The Huber G670 uses an image plate detector with a radius of 90 mm. In each measurement session, the sample powder was filled in a glass capillary tube and mounted in the sample position. A measurement on an empty glass capillary was carried out to subtract its contribution. The measurement time was set to 15 min. in all cases. More experiments were carried out on metallurgical and P-type silicon powders milled for various times.

University of Cape Town

5.2 Small angle X-ray scattering (SAXS)

Unlike X-ray diffraction which is mainly applicable to study the structure of crystalline materials, SAXS is a fundamental technique used to study the structure of any condensed matter. Guinier laid the foundation principles for the development of SAXS during his PhD research work in the years 1936-1939 [5, 6]. While XRD is useful to study the structure at atomic level, SAXS is useful to study structures with sizes on the nanoscale. With the standard X-ray sources, relevant information is obtained from SAXS only within a scattering angle less than 3°. It has a wide area of application in studying heterogeneous materials, fractal structures, micro-porous materials, nanocrystalline composites, and polymers amongst others [7-10]. There are basic differences between SAXS and standard XRD in terms of measurement techniques and area of applications.

University Of Cape Town

5.2.1 Scattering theory

When a sample is irradiated by X-rays, electrons become the source of secondary waves (scattered waves) as shown in Fig. 5.2. The secondary wave from each electron can be assumed to have the same amplitude but a different phase. The superposition of these waves can, therefore be represented as $e^{-i\vec{q}\cdot\vec{r}}$, where $\vec{r}$ is a vector showing the displacement between two scattering centres and $\vec{q}$ is the scattering vector given as

$$q = \frac{4\pi}{\lambda}\sin\left(\frac{\theta}{2}\right), \tag{5.8}$$

where θ the scattering is angle and λ is the x-ray wavelength.

To give more physical meaning to the analysis and comply with the uncertainty principle, it is necessary to consider a region of defined electron density.

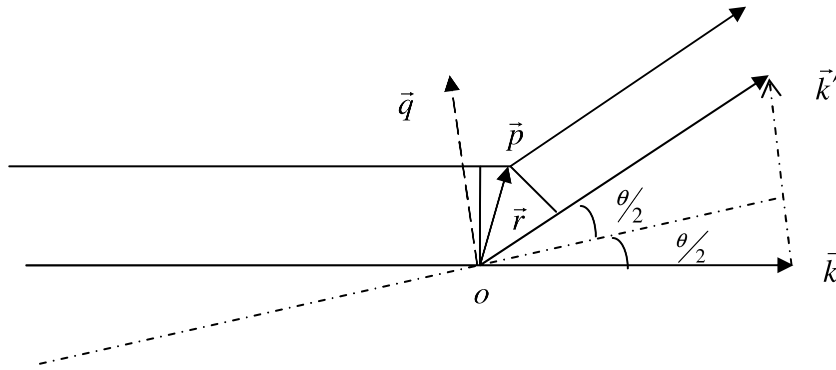

Fig. 5.2: Scattering by two point centres, after [11].

University of Cape Town

If the region under consideration has a volume dV and electron density of $\rho(\vec{r})$, the superposition of all the secondary waves from this region can be given as

$$F(q) = \iiint dV.\rho(\vec{r})e^{-i\vec{q}\cdot\vec{r}} . \tag{5.9}$$

From Eqn. 5.9 it can be seen that the amplitude $F(q)$ is the Fourier transform of the electron density distribution. In the general case, the intensity of the scattered waves is given as $I(q) = F(q)F(q)^*$ [11], which in full is

$$I(q) = \iiint \iiint dV_1 \cdot dV_2 \cdot \rho(\vec{r}_1)\rho(\vec{r}_2)e^{-i\vec{q}(\vec{r}_1-\vec{r}_2)} . \tag{5.10}$$

Two steps will be followed to carry out the double integral in Eqn. 5.10. First, summarize all pairs with equal relative separation $\vec{r}$. This yields a density of points in a fictious space [11] denoted as $\tilde{\rho}^2(\vec{r})$. Mathematically such an operation is referred to as an auto correlation, defined as

$$\tilde{\rho}^2(\vec{r}) \equiv \iiint dV_1\rho(\vec{r}_1)\rho(\vec{r}_2) , \tag{5.11}$$

where $\vec{r}_1$ and $\vec{r}_2$ are varied such that $\vec{r} = \vec{r}_1 - \vec{r}_2$ is held constant.

The second step is to integrate over the fictitious symmetric space including the phase factor,

$$I(\vec{q}) = \iiint dV \cdot \tilde{\rho}^2(\vec{r}) e^{-i\vec{q}\cdot\vec{r}} \ . \tag{5.12}$$

In a SAXS measurement of low dimensional systems such as particles, the system is assumed to be statistically isotropic and to have no long range order. As a result the following approximation can be made [12]

$$< e^{-iqr} > = \frac{\sin qr}{qr} \ , \tag{5.13}$$

where the distance r is the only parameter affecting the distribution of the auto correlation. Hence the scattering intensity can be redefined as

$$I(q) = \int 4\pi r^2 dr \cdot \tilde{\rho}^2(r) \frac{\sin qr}{qr} \ . \tag{5.14}$$

The same expression can be projected onto a single particle system for which Eqn. 5.15 has an asymptotic expression at small q given by

$$I(q) = I_o \exp\left(\frac{-q^2 R_g^2}{3} \right). \tag{5.15}$$

Equation 5.15 is know as the Guinier law, where R_g is the radius of gyration [13]. For an ellipsoid with semi-major axes of $a, b,$ and c, the radius of gyration is

$$R_g^2 = \frac{1}{5}\left(a^2 + b^2 + c^2\right). \tag{5.16}$$

For spheres, $a = b = c = r$ for which the radius of gyration will be

$$R_g^2 = \frac{3}{5} r^2 . \tag{5.17}$$

University of Cape Town

The scattering intensity under normal conditions is proportional to the square of the amplitude of the scattered signal. At small q this is the same as the square of the number of electrons, n_e^2. If there are N scattering elements over the irradiated volume, the intensity can be given as [14]

$$I(q) = Nn_e^2 . \tag{5.18}$$

For well defined smooth surfaces such as spheres, at high scattering vector, the number of spherical scattering elements is proportional to the surface area of the particles (S) divided by the area per scattering element, r^2. The number of scattering electrons over the spherical element is proportional to r^3. By substituting in Eqn. 5.18, it can be shown that

$$I(q) \propto \frac{S}{q^4} . \tag{5.19}$$

Specifically, for a composite system of a particle in a medium, with a relative density difference between the two phases given by $\rho_1 - \rho_o$, the scattered intensity is given by

$$I(q) = \frac{2\pi(\rho_1 - \rho_o)^2 S}{q^4} , \tag{5.20}$$

where S is now the total surface area of the interface region in the scattering volume.

5.2.2 Scattering from fractal structures

The mass of an object can be defined in terms of its characteristic size, *e.g.* radius R, as

$$M \propto R^d , \tag{5.21}$$

University Of Cape Town

where d is the mass fractal dimension, which describes the dimensionality of the object. Given an object of radius R, the relation between the surface area and the radius can be similarly given as $S \propto R^{d_s}$, where d_s is the surface dimension. For a smooth surface $d_s = 2$, whereas for a rough surface it can take any value between 2 and 3. Applying the scaling law to the general power law for the scattering intensity [15]

$$I(q) \propto q^{-\alpha}, \tag{5.22}$$

where $\alpha = 2d - d_s$. For a Euclidian object, in 3 dimensions, $d = 3$. The value of α for a smooth surface is therefore 4, which is Porod's law. But for a rough surface, where d_s can assume values between 2 and 3, the scattering power will be $3 < \alpha < 4$, indicating that scattered intensity decays weaker than predicted by Porod's law [16]. For mass fractals, the surface area scales with mass [17], so that $d = d_s$. Therefore for a mass fractal system the scattering power can assume values of α less than 3.

University Of Cape Town

5.2.3 Beaucage's global scattering function

The analysis of SAXS data, as described above, categorizes the q dependence of the scattering intensities into two regions. The scattering intensity in the low q region is described by an exponential (Guinier) law, whereas the scattering intensity in the intermediate and higher q range satisfies a power law. The slope from a log-log plot of scattering intensity versus scattering vector over the interval where the power law is valid can help to determine the fractal nature of the scattering centres. Likewise the slope from a semi-log plot of intensity versus the scattering vector in the Guinier region can help to determine the radius of gyration of the charge distribution in the scattering volume. Beaucage [18] has introduced a generalized equation given as

$$I(q) = G\exp\left(\frac{-q^2R_g^2}{3}\right) + B\left\{\left[erf\left(\frac{qR_g}{6^{\frac{1}{2}}}\right)\right]^3\right\}^{\alpha} , \quad (5.23)$$

where G and B are constant prefactors specific to the system of scattering objects. The first term in Eqn. 5.23 describes the exponential decay in scattering intensity at a size comparable to R_g for a given structure. The second term describes the power-law decay in the scattering intensity. The unified equation has been proved to be consistent with results obtained from other techniques [19].

5.2.4 SAXS experiment

The National Synchrotron Light Laboratory (LNLS) is a unique facility of its kind in the southern hemisphere [20], installed in Campinas, Sao Paulo State, Brazil. The LNLS synchrotron source is composed of a 120 MeV LINAC preinjector, 500 MeV booster synchrotron injector and a 1.37 GeV electron storage ring [21]. The source has an emmitance of 100 nmrad with an initial beam current of about 200 mA, and a beam life time of 16 Hrs.

University Of Cape Town

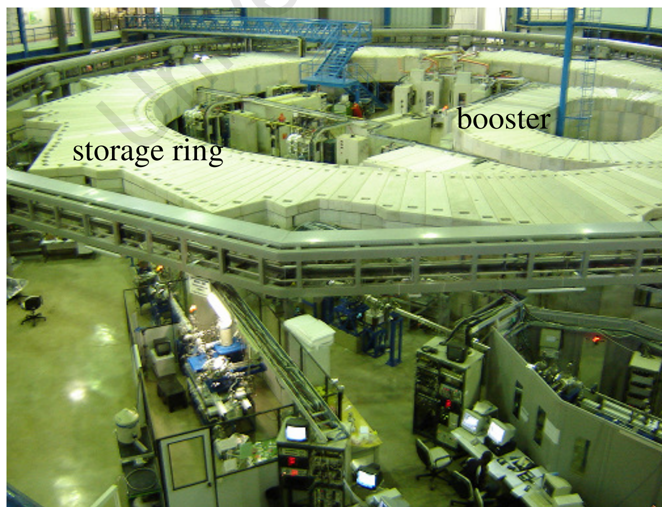

Fig.5.3: The national Synchrotron Light Laboratory (LNLS) facility, Campinas, Brazil.

Figure 5.3 shows a photograph of the Synchrotron facility at Campinas, Brazil. The circular concrete wall shields the storage ring whereas the inner oval concrete wall shields the booster. The experimental station appearing in the left foreground of the picture is for SAXS measurements.

The samples for the SAXS experiment can be categorized into two groups: free standing samples and samples printed on substrates. In the free standing category there are four different types of layers prepared from powders of intrinsic, metallurgical, N-type, and P-type silicon. The P-type and N-type silicon wafers were milled for 1 hour with a break after 30 min, but the metallurgical Si was milled for 3 hours in 30 min sessions until the set milling time was reached. Each powder type was mixed with cellulose acetate butyrate (CAB), from Goodfellow Ltd. UK, as a binder. The solvent used was trichloromethane. The ink from each powder was hand printed on glass slides. When the ink had dried the layer was peeled off the glass substrate to produce a free standing film. The second category of samples involved layers of three different types of powders and four types of binders. The binders used were CAB, commercial quality low density polystyrene (PS), a self polymerizing commercial acrylic printing base (ACR) from Daler-Rowney, USA, and refined linseed oil (LIN) supplied by Windsor and Newton, UK. Since the acrylic base only dissolves in polar solvents, ethanol was used as a solvent. The remaining compositions all were dissolved in trichloromethane.

University of Cape Town

The sample naming is done in such a way that it reflects the powder type and the binder used. For example the metal grade silicon in linseed oil is designated as M-LIN. For the free standing samples since only one type of binder involved, the naming is just indicated by the powder type accompanied by the word “FREE”. For example the free standing layer of intrinsic silicon is named as I-FREE. The details of ink production are discussed in chapter 4. In all cases the amount of powder used to produce ink was 0.4 g. The amount of PS and CAB binders used

were 0.16 g, ACR was 0.32, and LIN was 0.2 g. The composites were hand mixed using a spatula and printed using a glass rod on a cellulose substrate of thickness 25 μm. No special curing treatment was performed, and all the layers were kept in ambient condition for a week before conducting the SAXS experiment.

The LNLS has 12 bending magnets in the electron storage ring, at which the beamlines are positioned. One known as the D11A-SAXS beamline is dedicated for SAXS. The polychromatic, white photon beam from the storage ring first passes through a beryllium window and then to a single crystalline monochromator. The monochromatic beam is focussed horizontally and tuneable between $2A^o$ and $1A^o$ [22]. For this experiment it was set to $\lambda = 1.608A^o$. For typical detector-to-sample distances, the energy resolution $\frac{\Delta E}{E}$ is about 1000 [23]. The SAXS setup has three sets of slits to define the beam collimation. The first set of slits is located before the monochromator, and the second one is immediately after the monochromator. The first and second sets of slits help to define the beam cross section. The third set which is directly in front of the sample is used to reduce the parasitic scattering at very small angles.

University of Cape Town

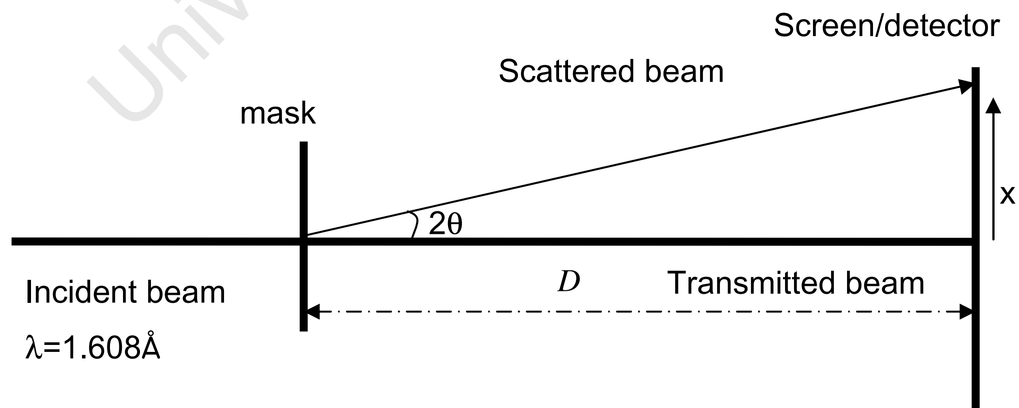

Fig.5.4: A simplified setup sketch for the one dimensional SAXS measurement.

Figure 5.4 shows a simplified sketch of the experiment for which D was 1077 mm. The measurement was performed in transmission geometry implemented for the whole sample at a slit width of 0.5 mm. Using the 0.5mm slit width helps to minimize possible smearing effects on scattering intensity at lower scattering angles [20]. The beamline is equipped with two kapton scattering films and detectors, positioned each side of the sample holder, to monitor the primary beam intensity and absorption in the sample chamber. Air scattering and parasitic scattering from the sample holder were determined by measuring with an empty sample chamber and empty sample holder respectively. Similarly, the substrate signal was measured using a blank cellulose acetate film in the sample holder. SAXS spectra for the printed layers were measured with the silicon between the substrate and the detector. Data were recorded using a vertically mounted 1-dimensional wire chamber detector with a calibration of 61.576 μm per channel and a fixed sample to detector distance of 1.077 m, yielding and effective angular range of 5^0 above the primary beam. The measurement times were 3 x 600 = 1800 s for each sample. Conversion from detector position in channels to scattering vector and standard corrections were made on-site with software provided with the instrumentation. This program uses established algorithms and measured data to correct for the detector inhomogeneity, intensity variation and parasitic scattering. The measured substrate contribution was subtracted, as variable parameter in proportion to the measured attenuation, in the subsequent data analysis. It was found, however, that, because the scattering from silicon is much higher than that from the carbon-based substrate material, magnitude of this correction had little effect on the final results.

5.3 Scanning electron microscopy (SEM)

Scanning electron microscopy is a powerful technique used to study surface morphology, microstructure, and composition, by producing an image of the

University of Cape Town

sample with high resolution [24, 25]. When the surface of a sample is irradiated by a beam of electrons, there will be a scattering of electrons, both elastically and inelastically, as shown in Fig. 5.5. In both cases the scattered electrons provide an important signal that is used to characterize the sample. The possible measurement signals from electron scattering include: emission of secondary electrons, backscattering of electrons, emission of Auger electrons, characteristic X-rays and visible photons. The characteristic X-ray signal is helpful to study the elemental composition of a sample using energy dispersive X-ray spectroscopy [26]. However, SEM is best known for image based analysis. The signals of secondary electron emission and backscattered electrons are the ones which are generally used to generate high resolution images. The quality of the image can be influenced by the scanning spot size, the magnitude of the probe current and by the angle of convergence. For a highly resolved, and higher quality, image it is better to use smaller spot size and high probe current [27]. A low angle of convergence helps to generate well focused image [28, 29].

University Of Cape Town

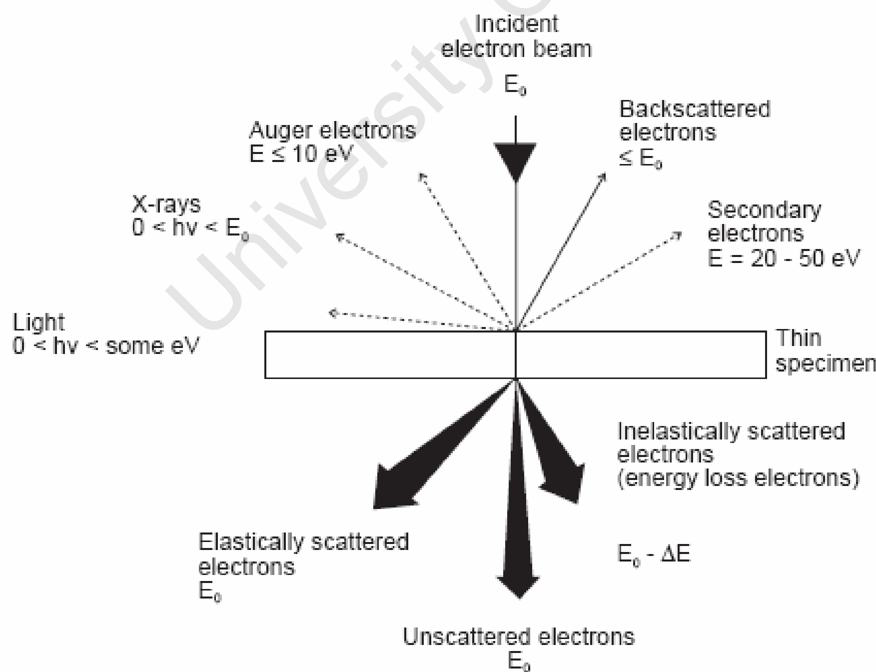

Fig.5.5: Types of electron scattering [30].

In the microscope used, a Leica S440, the energy of the electron beam can be adjusted between 300eV to 30 keV. It is capable of attaining a resolution of 4.5 nm for Tungsten and 3 nm for the LaB_6 filament.

SEM micrographs were produced from hand printed layers of silicon ink in linseed oil. Secondary electron imaging was used to study the layer morphology at different magnifications.

5.4 Transmission electron microscopy (TEM)

A transmission electron microscopy is a true microscope which operates on the same basic principles as an optical microscope, in which lenses are used to form images from the scattered beam [31]. Unlike in the optical microscope, the thickness and refractive index of electron lenses are variable depending on the accelerating voltage [32]. The images formed by a TEM are magnified and inverted. The extent of magnification is limited by the resolution limit, which depends on the de Broglie wavelength λ of the electron [33]

$$l = \frac{0.61\lambda}{n\sin\alpha}, \tag{5.24}$$

where n is the refractive index between the object and the objective lens and α is the subtended angle by the aperture at sample position. The electron wavelength λ, and accelerating voltage expressed as an energy E, are related by $\lambda = \frac{hc}{E}$, where h is Planck's constant, c is the speed of light in vacuum. In practical units this is

$$\lambda(nm) = \frac{1.2398}{E(keV)}. \tag{5.25}$$

The microscope used was a Leo 912 OMEGA equipped with adjustable accelerating voltage from 60 kV to 120 kV. The attainable magnification can be

University of Cape Town

set according to the operation mode selected, since its setting is uniquely defined. With the imaging system it is possible to attain magnification as large as 500,000 at a resolution of 0.37 nm. Another point that makes TEM different from SEM is the form of the sample required. Since it is needed that electrons should pass through, it must be thin. As a result sample preparation for TEM is challenging.

Different set of powders were characterised with this technique. For most of the measurements, samples were produced from a very dilute dispersion of powder in ethanol. The mixture was allowed to settle so that larger particles were eliminated from the analysis. A drop of solution of the suspended particles was dried at 60 ^{0}C onto standard carbon coated copper TEM grids. For the elemental mapping of dopants, the powder was cast in a resin binder, which was then sliced using a microtome.

5.5 Raman spectroscopy

Named after its discoverer, C. V. Raman in 1928 [34], Raman scattering is a powerful scattering technique used to study the bonding of materials. Its application is over a wide range of disciplines from biological sciences [35], chemical sciences [36] to material science where it is used to study properties of the material such as phase state, degree of crystallinity, and crystal size.

When light is scattered elastically, without violating the principles of conservation of energy and momentum, the internal energy states of the scattering object, both rotational and vibrational, remain unaffected, implying that the photon energy before and after collision is the same. This is the condition for Rayleigh scattering [37]. However, a small fraction of light is scattered inelastically, which is a basis for Raman scattering. After scattering the rotational or vibrational energy of the bond changes by ΔE_m, and in the process a phonon is either

University Of Cape Town

created or annihilated. If we let $h\upsilon_s$ be the energy of scattered photon and $h\upsilon_i$ be the energy of incident photon,

$$\Delta E_m = h(\upsilon_i - \upsilon_s)\,. \tag{5.26}$$

This shift in photon energy corresponds to the energy of a phonon that has been either created or annihilated. When ΔE_m is positive, the photon loses energy to the material, creating a phonon, giving rise to Stokes scattering. But when ΔE_m is negative, the material loses energy to the photon by the annihilation of a phonon, giving rise to anti-Stokes scattering [38, 39]. Figure 5.6 shows the three possible scattering processes. There is no Raman effect in Rayleigh scattering. The typical phonon energy is of the order of meV, whereas the energy of the scattered visible light is of the order of eV. Because the phonon energy corresponds to infrared wavelengths, complementary information can be obtained from Infrared (IR) Spectroscopy [40].

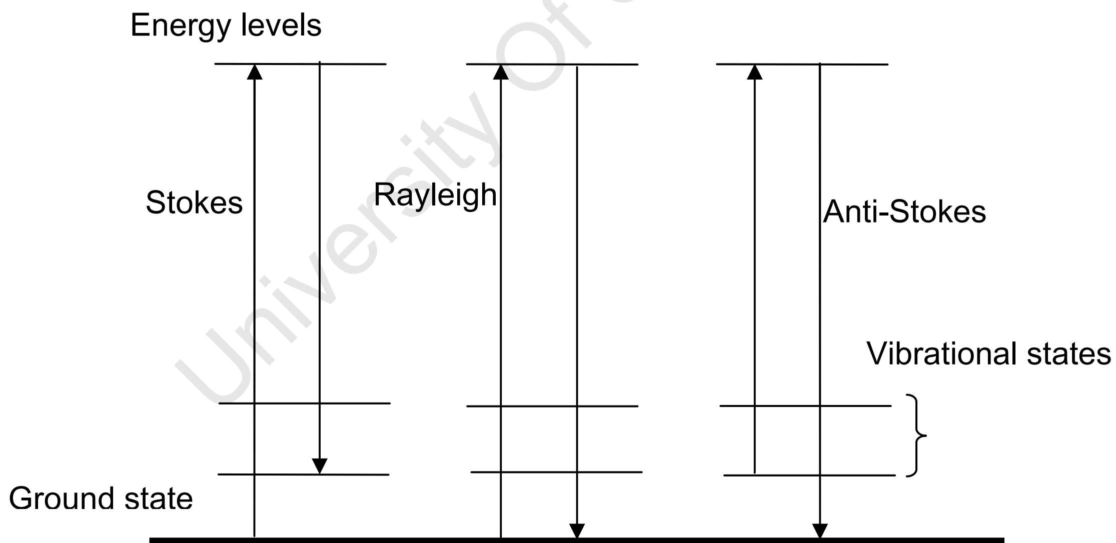

Fig.5.6: Simplified sketch showing Raman scattering

According to the Boltzmann distribution function, the ratio of the intensity of the Raman anti-Stokes and Stokes lines is predicted to be [41]

University Of Cape Town

$$\frac{I_A}{I_S} = \left(\frac{\upsilon_i + \upsilon_{phonon}}{\upsilon_i - \upsilon_{phonon}}\right)^4 \exp\left(\frac{-h\upsilon_{phonon}}{kT}\right), \tag{5.27}$$

where $-h\upsilon_{phonon} = -\Delta E_m$.

Obviously, the exponential term is the dominant term, leading to a conclusion that the anti-Stokes scattering is less intense than the Stokes. An equivalent explanation can be given in terms of the number of molecules in the ground state compared to the excited state. The lower intensity of anti-Stokes line means fewer molecules are initially in the excited state. Under normal conditions most of the molecules are expected to occupy the ground state. For a bond to be Raman active, a vibration must produce an oscillating polarizability α [42]. When a bond is placed in electromagnetic radiation, the electric field component induces negative charges on one side and positive charges on the other. As a result a dipole moment μ will be created.
Mathematically

$$\mu = \alpha E, \tag{5.28}$$

where E is the electric field and α is polarizability. The electric field of the electromagnetic radiation in the vicinity of the molecule varies with time

$$E = E_0 \cos 2\pi\upsilon t, \tag{5.29}$$

and hence

$$\mu = \alpha E_0 \cos 2\pi\upsilon t, \tag{5.30}$$

where E_0 is a constant amplitude. The intensity of the radiation emitted by the dipole moment is proportional to the maximum value of the square of μ. The polarizability α of a bond is not constant as it varies with certain vibrations or rotations as the shape of electron cloud changes. For small displacement ΔS,

University Of Cape Town

the polarizability can be expanded in a Taylor series to first order approximation as

$$\alpha = \alpha_0 + \frac{\partial \alpha}{\partial(\Delta S)}\Delta S + \ldots, \qquad (5.31)$$

where α_0 is the equilibrium polarizability. The displacement ΔS varies periodically,

$$\Delta S = (\Delta S)_0 \cos 2\pi\upsilon' t, \qquad (5.32)$$

where $(\Delta S)_0$ is constant and the maximum value of ΔS and υ' is the frequency of the normal oscillation. Combining the above equations will yield

$$\alpha = \alpha_0 + \frac{\partial \alpha}{\partial(\Delta S)}(\Delta S)_0 \cos 2\pi\upsilon' t. \qquad (5.33)$$

Substituting in the dipole moment expression, Eqn. 5.28, results in

$$\mu = \alpha_0 E_0 \cos 2\pi\upsilon t + \frac{\partial \alpha}{\partial(\Delta S)}(\Delta S)_0\, E_0 (\cos 2\pi\upsilon' t)(\cos 2\pi\upsilon t). \qquad (5.34)$$

Rearranging yields

$$\mu = \alpha_0 E_0 \cos 2\pi\upsilon t + \frac{\partial \alpha}{\partial(\Delta S)}(\Delta S)_0\, E_0 [\cos 2\pi(\upsilon - \upsilon') + (\cos 2\pi(\upsilon + \upsilon')t]. \qquad (5.35)$$

From this we note that the induced dipole can assume three different frequencies υ, $\upsilon + \upsilon'$ and $\upsilon - \upsilon'$ which gives rise to Rayleigh scattering, Stokes and anti Stokes Raman scattering respectively.

In this research a Delta Nu Advantage 532 bench top spectrometer, equipped with a low magnification optical microscope was used. The Advantage 532 uses visible light of wavelength 532 nm, which is frequency doubled from a Nd:YAG source with a power of 20mW [43]. In all cases, samples were used in powder

University of Cape Town

form, which was placed and compacted in a vial. An adjustable stage was used to position the sample in focus.

The first step in the process of measurement was to optimize Advantage 532 Raman spectrometer. The input of Alex Finnemore [44] in the optimization and data acquisition is duly acknowledged. It was noticed in measurements of a silicon wafer reference sample that a large background was due to the microscope system. The reason for this was subsequently found to be due to a damaged compound lens. In particular a broad peak around 1080 cm^{-1} was seen under all measurement conditions (Fig. 5.7). This was taken as a background signal and subtracted during the analysis.

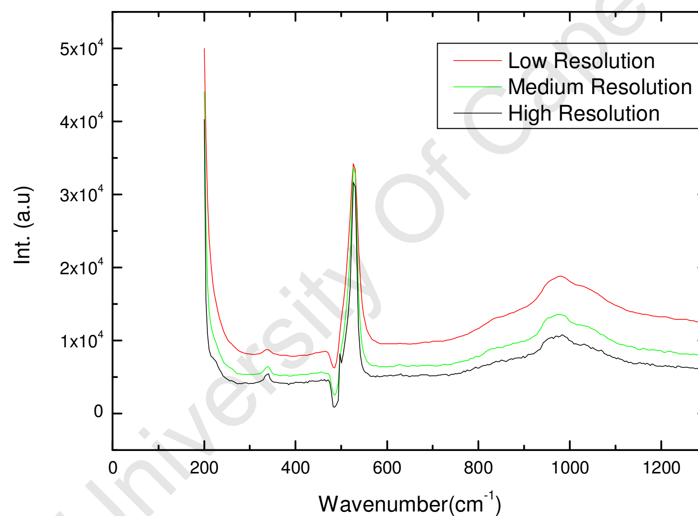

Fig.5.7: Raman spectra of a silicon wafer reference sample recorded under different conditions showing instrumental background at around 1080 cm^{-1} (data from [44]).

5.6 Electrical measurements

The Hall effect measurement system (HMS) shown in Fig. 5.8 is a cluster of advanced integrated hardware and control software. The system is capable of measuring the resistivities of samples of different geometries at variable

University Of Cape Town

temperature and variable magnetic fields. The hardware components are: high precision voltmeter (Keithley 2182A Nanovoltmeter), stable current source (Keithley 6220 Precision Current Source), high precision ammeter (Keithley 6485 Picoammeter), electromagnet with Lakeshore 642 Electromagnet Power Supply unit, Lakeshore 475 DSP gaussmeter, HMS Matrix amplifier, Lakeshore 340 temperature controller and sample mounting unit with the heating/cooling system.

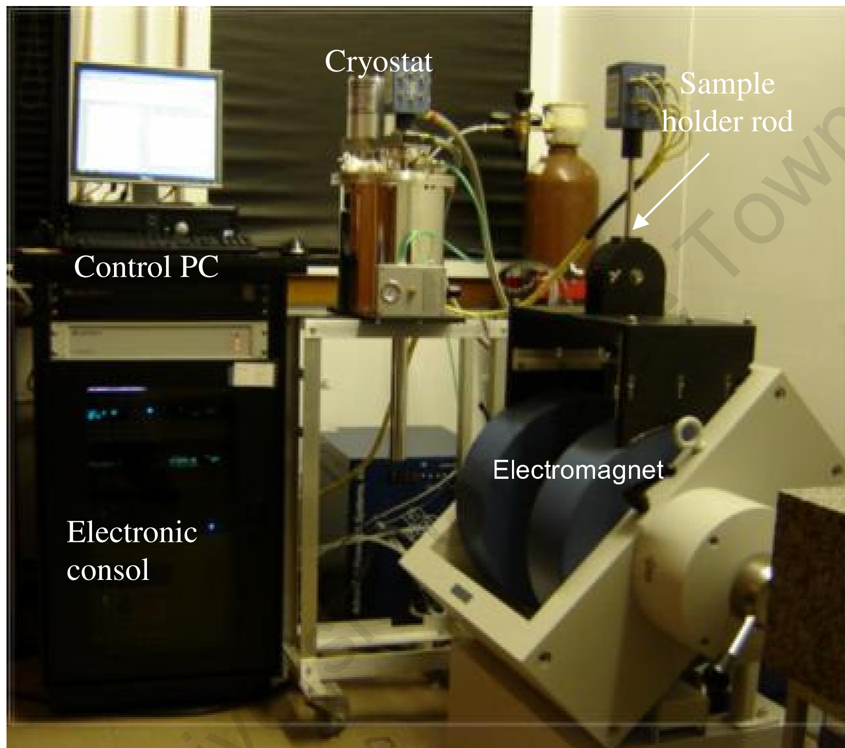

Fig.5.8: The Lake Shore 7500 Hall effect measurement system.

University of Cape Town

5.6.1 The software

The control software, supplied by Lakeshore Inc, is fully automated to control all the components of the HMS system. The software enables the performance of various measurements such as current-voltage, variable field and variable

temperature dependent measurements [45]. The measurement setup conditions are given in **Appendix A.**

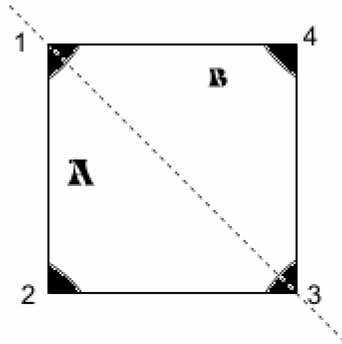

Fig. 5.9: Definition of the geometries for a Van der Pauw sample. The lower region is geometry A and the upper region geometry B.

It is advisable to carry out the IV measurement at zero field between pairs of contacts as this helps to judge the quality of the contacts. If the contacts are good, the curve is a straight line indicating ohmic behaviour. In most cases, for the geometry given as in Fig. 5.9, the measurement configurations are $R_{12,12}$, $R_{23,23}$, $R_{34,34}$ and $R_{41,41}$ as defined in chapter 3.

The basis for this software is the theory presented in section 3.3. For Van der Pauw type samples shown in Fig. 5.9, two geometries, A and B, are defined from the way the sample is connected in the Hall measurement system. Defining the sample geometry is important to minimize the errors caused by misalignment of contacts. A series of resistance measurements between the opposite edges of the sample, and also the Hall resistances along the diagonals are performed. The excitation current is applied across one edge and the potential difference along the opposite edge is measured to calculate the resistance. For example in Fig. 5.9, when current is applied between points 1 and 2, voltage is measured between points 4 and 3. This gives the resistance $R_{12,34}$ between opposite sides of the sample. The measurement is done in permutation and the resistance values for the two geometries are determined according to Eqns. 3.57 a) and

University of Cape Town

3.57 b). By making use of the dimensions of the sample, the resistivity, given by Eqn. 3.62, is calculated in real time. Since the current is reversed for each contact and an average taken over the geometries, possible errors, with exception of the Ettingshausen effect, as discussed in chapter 3, will be minimized.

The correct Hall voltage is determined by taking a series of measurements according to Eqns. 3.50 to 3.53, for positive and negative values of excitation current and magnetic fields. Reversing the magnetic field and the excitation current helps to remove the parasitic voltage that appears along with the true Hall voltage. In total, to yield single data point, 32 actual resistance measurements are performed. Sixteen of the measurements are for geometry A and the remaining sixteen for the geometry B. From the Hall resistance measurement, the Hall coefficient is calculated using the relation given by Eqn. 3.72, and the carrier type identified from the sign of Hall coefficient. The carrier concentration is determined from the Hall coefficient using Eqn. 3.28. In a similar way, from the ratio of Hall coefficient and the zero field resistivity, as given by Eqn. 3.29, the mobility of the carrier is determined.

University of Cape Town

5.6.2 IV measurements

Current-voltage (IV) measurements were an important part of the experiment to determine the quality of contacts and layers. For this purpose we have used three different setups, the home built and two automated systems. The home built setup was mainly used in the study of hand printed layers of various silicon inks in rectangular shape or in Hall bar geometry. The automated system, a Keithley 4200 Semiconductor Characterisation System, was used both for the hand printed and for screen printed layers, whereas the Lakeshore HMS was used purely for screen printed samples.

The main materials that have been studied were intrinsic, metallurgical, N-type, and P-type silicon. DuPont 5000 Silver was also studied for its electrical response and its feasibility to make electrical contacts. The curing behaviour of printed silver layers was measured by a simple resistance measurement using a four point probe technique with the help of a Keithley 2000 Digital Multimeter interfaced to a personal computer.

On the other hand, blocks of silver layers were prepared using the screen printer with the aim to use them as metal contacts for the Hall devices in Hall bar geometry. The pattern and code designation of the print is as indicated in Fig. 5.10.

University of Cape Town

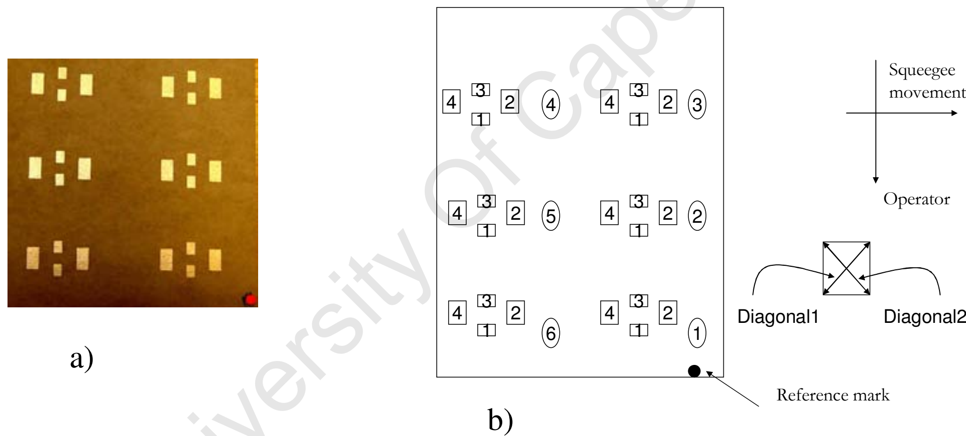

Fig.5.10: a) photograph of silver contacts printed on paper, b) code convention of contacts for Hall bar.

The reference mark with other labelling helps to precisely track each and every device. The device numbering is in the counter clockwise direction starting from the bottom right. Each silver block within a device is similarly labelled in counter clockwise direction starting from the bottom. Therefore each block can precisely be described as a combination of device number and block number. These structures were used to study how the print quality and thickness affect the

resistance of each block. For this purpose large number of layers were printed with single and double print cycles. Unlike in the earlier time dependent analysis, before the measurement all the layers were allowed enough drying time under ambient conditions. A digital multimeter was used to determine the resistance across the diagonal of each block and the mean value was considered to represent the resistance of each block. The measurement was conducted for 10 randomly chosen printed layers. According to the chosen notation convention R_{ab} stands for resistance of device a and block b, where $a = 1,...,6$ and $b = 1,2,3,4$. Blocks with odd values, or all with even values, of b have the same dimensions. Those which are even numbered have a larger surface area with dimensions 5.5 x 3 mm^2, whereas the smaller blocks have dimensions of 3 x 2 mm^2.

The resistance measurement technique was used to recommend one from the two possible ways of making contacts as demonstrated in Fig. 5.11. For this study layers of intrinsic, metallurgical, N-type and P-type silicon were used to produce samples with top and bottom contacts. The inks were prepared with linseed oil and CAB as a binder, and printed using the techniques were as discussed in the previous chapter.

University of Cape Town

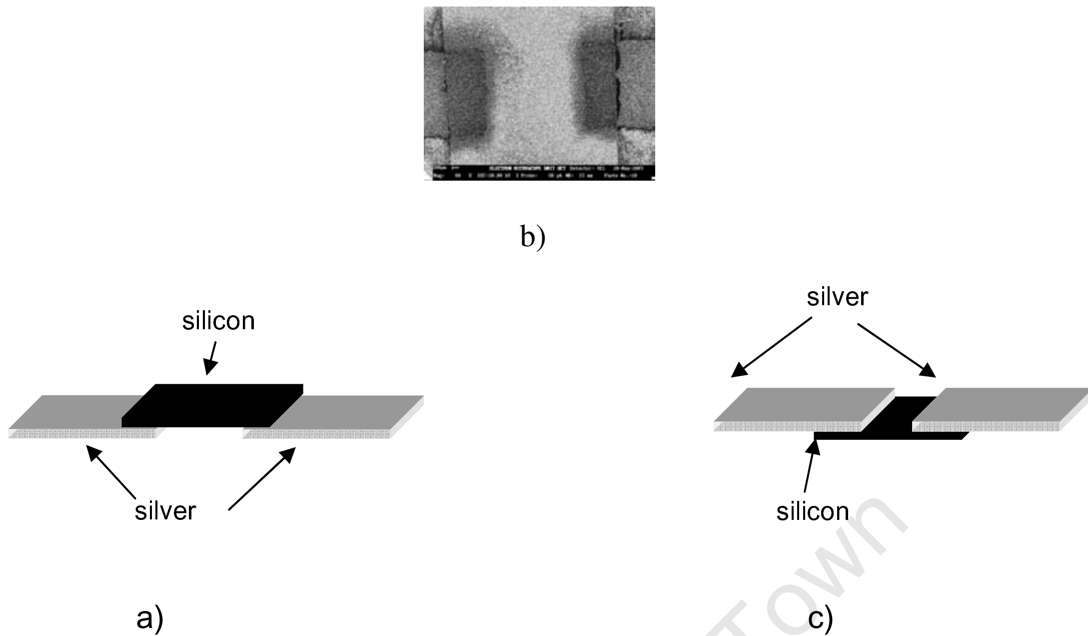

Fig.5.11: The two ways of making metal contacts: a) bottom contact with b) the actual device micrograph from scanning electron microscope, and c) top contact.

University of Cape Town

The effective device size for the bottom contact structure was 5 mm x 10 mm where as for the top contact structure it was 5.5 mm x 10 mm. A two point resistance measurement was conducted across the length of the device using the Keithly 4200 semiconductor characterisation system.

5.6.3 Home built Hall measurement system

The Hall effect is the main technique used in this work for the electrical characterization of materials. As already mentioned above, two measurement setups were used during the entire study. The home built setup was equipped with a permanent magnet of fixed field strength 0.125 T. This is a low field system which does not give an opportunity for field dependent studies. The samples that have been characterized were intrinsic silicon, metal grade silicon, P-type silicon and N-type silicon in linseed oil binder. The samples were produced according to the methods described in chapter four. The device structure mainly used at this stage of experiment was the Hall bar with

rectangular geometry. The thickness of each layer was estimated using a micrometer screw gauge. The electrical connections for the Hall measurement were as shown in Fig. 5.12, with the magnetic field acting perpendicular to the page. As a first step in the determination of the Hall parameters, the resistivity of each sample was determined from the IV characteristic curves between contact points 1 and 3 of Fig. 5.12

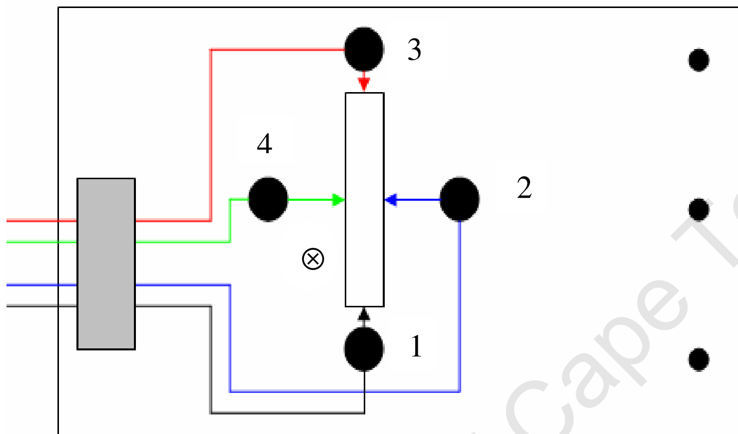

Fig.5.12: Electrical connections in the home built Hall effect measurement system using Hall bar geometry.

University Of Cape Town

The Hall voltages were measured between points 2 and 4 with and without the magnetic field for both positive and negative current directions. This was done to take into account the effect of any Hall voltage offset.

The data acquisition and analysis techniques for all the samples were identical. In the home built single field measurement system, there were some necessary assumptions made during the analysis such as the dominance of single charge carrier, the homogeneity of the printed layers and a constant laboratory environment.

5.7 Impedance analysis

Impedance Analysis, as has been discussed chap. 3, is a powerful technique to characterise the electrical properties of materials. The Cole–Cole plot, which is the plot of imaginary impedance or immittance versus the real component, is the core for the analysis. The response curve tells the nature of conduction in the bulk or at interfaces. The equivalent circuit for the sample can easily be extracted. For this measurement a HP LF4291A low frequency impedance analyser was used. The oscillation level varies from 5 mV to 1.1 V with a minimum resolution of 1 mV. It has a dc source varying up to +/-35 V to study the bias effect [46]. Samples were produced in a sandwich structure of silicon, with top and bottom silver contacts and silicon layer in the middle. Both single and bilayer structures were studied.

University Of Cape Town

6 Results

6.1 Powder characterization

Different techniques have been applied to characterize the powders in terms of their phase structure, grain size, morphology, and composition. The following three subsections will present the results.

6.1.1 X-ray diffraction

A Bruker AXS D8 Discover Diffractometer was used to characterize milled and commercially obtained silicon as described in the experimental sections. The P- and N-type powders were produced from single crystalline silicon wafers milled for 40 minutes. Figure 6.1 a) and b) show the X-ray diffraction patterns for the P and N powders respectively, while Fig. 6.1 c) shows the corresponding pattern for the intrinsic powder produced by pyrolysis of silane. In all the three samples studied, five peaks, corresponding to the (111), (220), (311), (400) and (331) reflections of crystalline silicon were observed. The last two peaks at higher diffraction angles are more clearly visible for the N- and P-type powders. This suggests that the milled P and N silicon particles have larger grain sizes than the intrinsic Si powder. The broadening of the first peak (111) at the base in Fig. 6.1 c) is a contribution from an amorphous phase, which may be either from the glass used as a substrate or a possible amorphous phase in silicon nanoparticles. For the P- and N-type material the peak at 23^0 could be a contribution from SiO_2. The (111) peaks for N and P powders are slightly broadened, at a FWHM of 0.2^0 compared to the instrumental width of 0.15^0. The peak width is larger at 0.26^0 for the intrinsic powder, also indicating a smaller grain size.

University of Cape Town

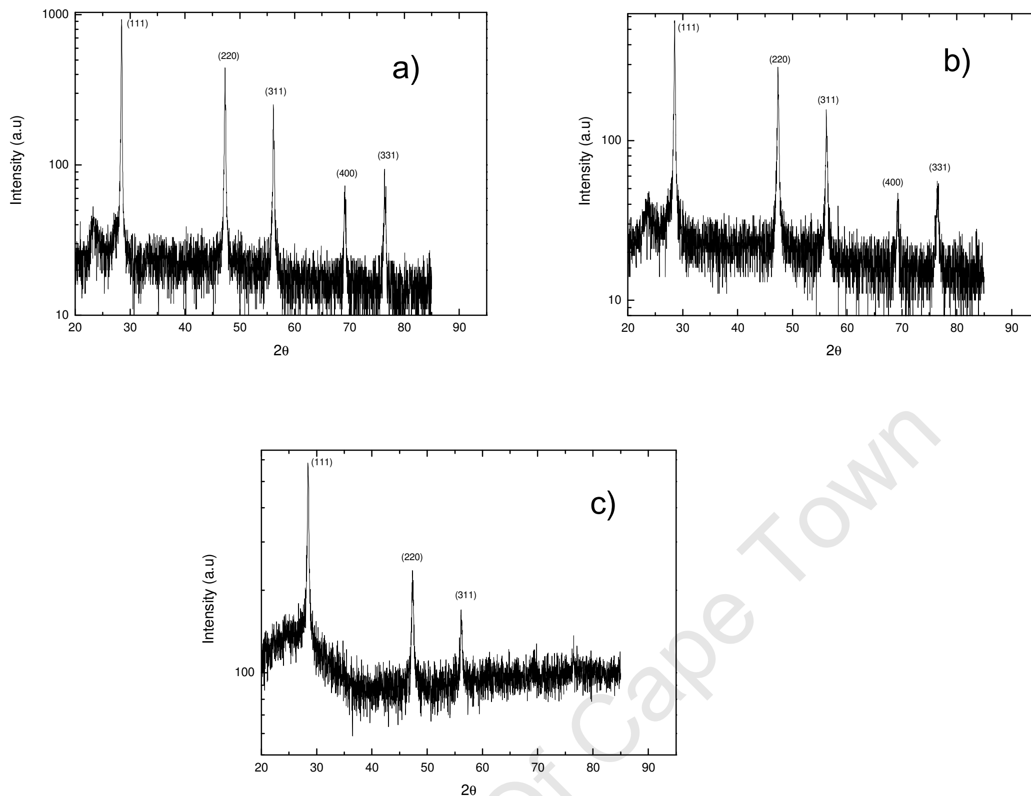

Fig. 6.1: X-ray diffraction patterns for powders of: a) P-type b); N-type; and c) intrinsic silicon.

University Of Cape Town

The Guinier camera facility in the Chemistry Department at UCT was used for the characterization of metallurgical and P-type Si for different milling times. Because of its higher instrumental resolution and lower background noise, the application of Scherrer's technique, according to Eqn. 5.2, was considered reasonable to estimate the crystallite size.

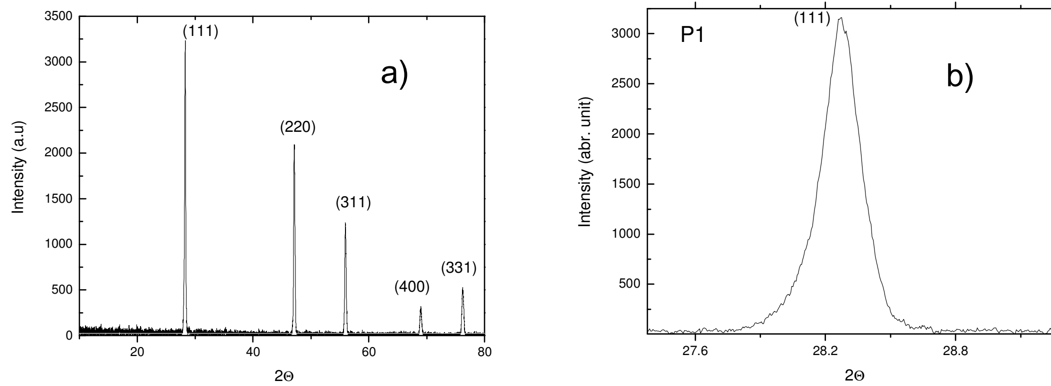

Fig.6.2: a) XRD pattern from P-type silicon milled for 1 Hr, b) an expanded view of (111) peak.

This is a robust technique to estimate the crystallite size irrespective of whether the material is single or polycrystalline. The contribution from the instrument to the FWHM was subtracted according to the relation

$$(FWHM)^2 = (FWHM)^2_{\exp} - (FWHM)^2_{ins}\ .$$

The subscript $\exp$ stands for measured width, whereas ins is for the instrumental broadening. From the specifications of the machine, the X- ray beam has a line width of 0.4 mm and a radius of the focal circle of 90 mm, for which the instrumental resolution is considered to be 0.1º.

The (111) diffraction peak was considered for the analysis. The average crystallite size for the intrinsic silicon was obtained as (26.2 ± 1.3) nm, whereas for metallurgical silicon milled for 180 minutes it was (30.6 ± 1.5) nm. The dependence of crystallite size on the milling duration was studied for the P-type silicon. For longer milling times, the FWHM of the first peak was increasing suggesting a decrease in crystallite size. As shown in Fig. 6.3 the FWHM for the 1 Hr milled P-type silicon is 0.22 ± 0.01º whereas for the 5 Hrs milled powder it is 0.25 ± 0.01º.

University Of Cape Town

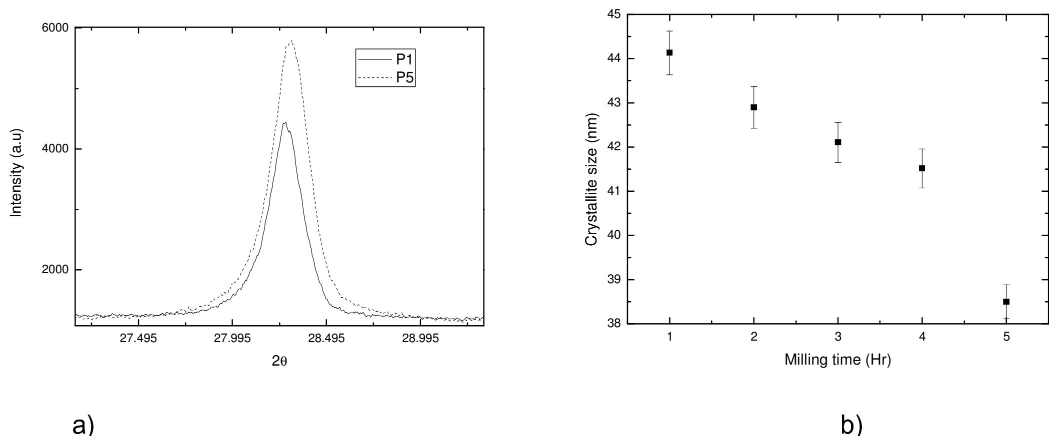

a) b)

Fig. 6.3: a) the change in the (111) peak position and FWHM between 1Hr and 5Hr milled P type silicon powder, b) crystallite size as a function of milling time for p-type materials.

Using Scherrer's equation, after correction for the instrumental broadening, the estimated crystallite size reduced systematically from 44 nm to 38.5 nm over 5 Hrs milling time as shown in Fig. 6.3 b). There is also an indication of lattice relaxation with milling. The peak position for 1Hr milled P-type powder is at $2\theta=28.276 \pm 0.001^{o}$, whereas for 5 Hrs milled powder it is at 28.300 ± 0.001^{o}, corresponding to a relative change in lattice spacing of approximately 0.05%

6.1.2 Transmission electron microscopy

The micrographs shown in Fig. 6.4 were obtained using the Leo 912 OMEGA TEM at the UCT electron microscope unit. The analysis of the micrographs shows that the morphology of the intrinsic silicon powder particles are more spherical in shape and form a chain like structure with branches. Sintering may be the result of the elevated temperature during the synthesis process. The other remaining powders shown were milled for one hour each.

University of Cape Town

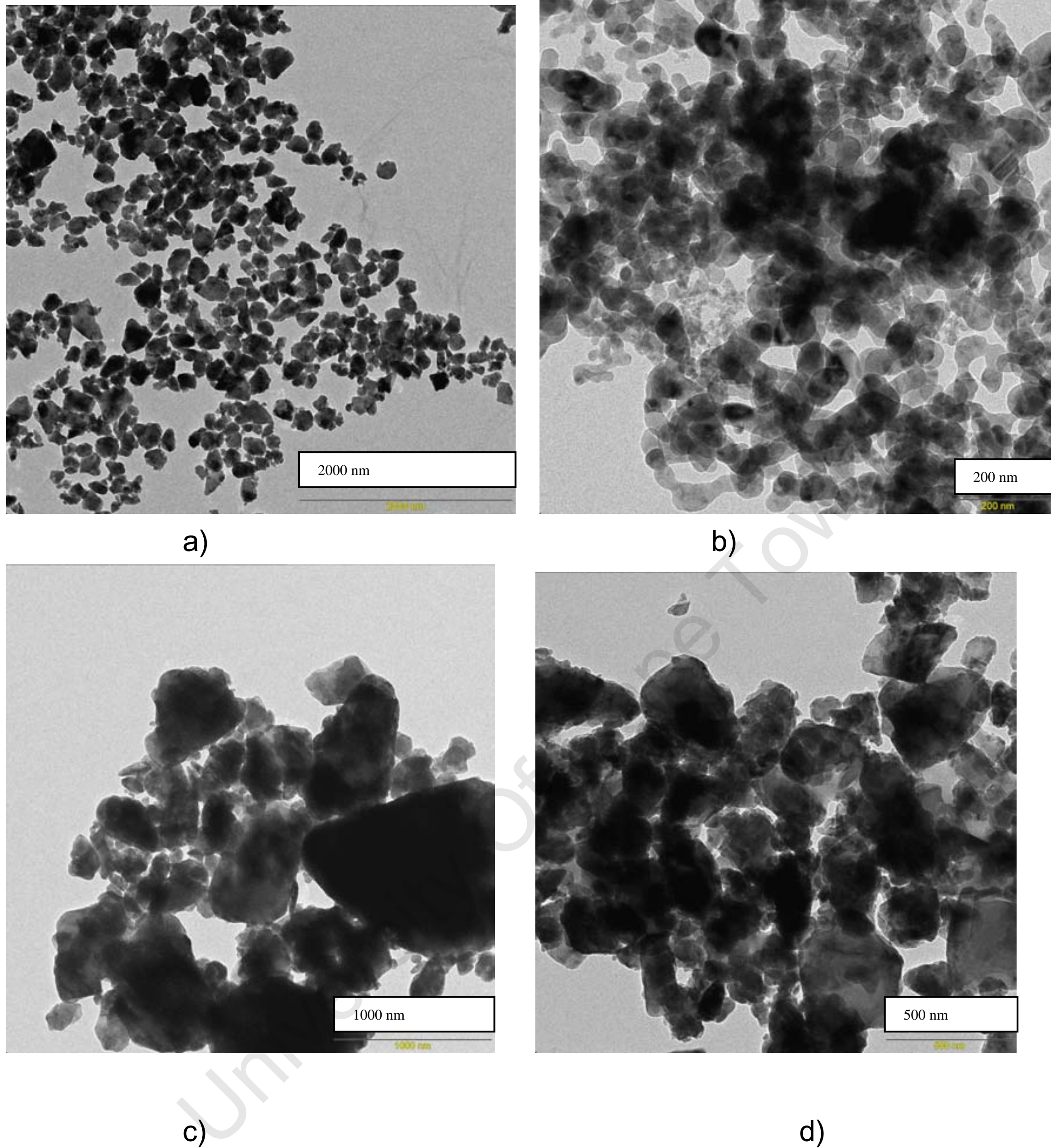

Fig. 6.4: TEM micrographs for: a) the N-type; b) Intrinsic; c) Metallurgical grade; and d) P-type silicon.

The particles of milled metal grade silicon (Fig. 6.4 c)) appear to be oblate while the particles from milled wafers appear to be more rugged but with a regular shape. The particle size distribution was calculated from the micrographs given in Fig. 6.4 using Digimizer image processing software [1].

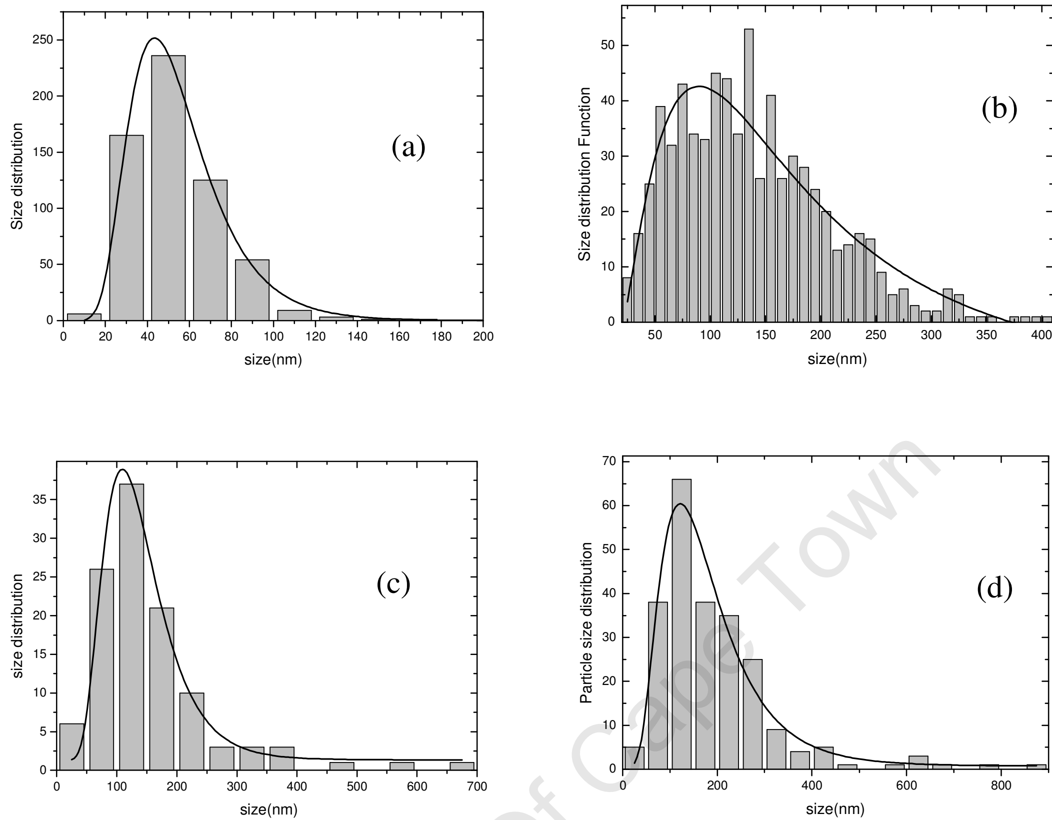

Fig. 6.5: Size distribution of: a) i-Si; b) 1Hr milled N-type silicon; c) 1Hr milled M-Si; and d) 1 Hr milled P- type silicon.

University Of Cape Town

Origin software was used to plot the frequency against the particle size. The distribution was fitted to a lognormal function to determine the average particle size indicated in Table 6.1.

Table 6.1: Average particle size of the powders

Material	Size (nm)
i-Si	51.08 ± 0.26
N-type silicon	163 ± 26
M-Si	129.7 ± 3.3
P-type silicon	160.4 ± 6.8

According to the producers' specification the average particle size for intrinsic silicon (i-Si) is less than or equal to 50 nm, in agreement with the TEM observation.

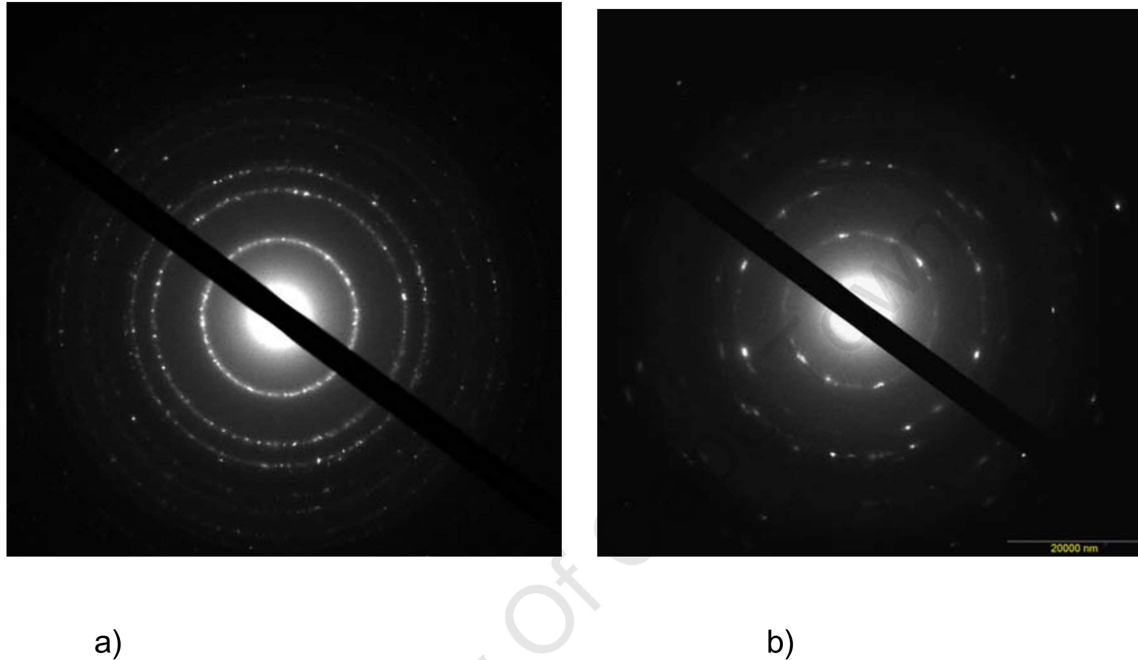

a) b)

Fig. 6.6: Electron diffraction from a) intrinsic silicon and b) P-type silicon powder.

The electron diffraction patterns shown in Fig. 6.6 indicate the presence of a large number of superposed diffraction patterns with narrow rings suggesting that the particles may be polycrystalline. As can be seen, the size of bright spots is the same as the width of the ring, suggesting that there is little or no amorphous fraction. This was observed for all the milled powders. In case of intrinsic silicon, it was impossible to be conclusive since the area sampled for the diffraction covered a number of particles.

University Of Cape Town

6.1.3 Raman spectroscopy

The major objectives for this experiment were to establish the contamination level of the silicon powder as a function of milling time and synthesis methods. Also it was hoped to verify the effect of size reduction on the Raman shift which may complement other techniques that have been discussed.

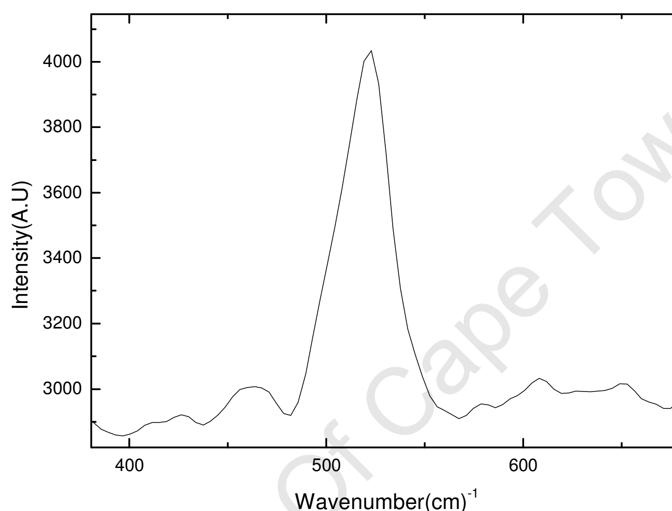

Fig. 6.7: Raman shift for single crystalline silicon used for the calibration purpose.

University of Cape Town

From literature crystalline silicon has two main Raman peaks. The first order peak is around 520 cm^{-1} whereas the second order peak occurs at around 950 cm^{-1} [2]. Depending on the crystallite size, the first order peak position can shift to as low as 512 cm^{-1}, whereas for amorphous silicon a broad band around 480 cm^{-1} is expected [3]. The spectrum obtained for a silicon wafer, shown in Fig. 6.7, is consistent with the literature which validates our measurement system.

Characterization was performed for powders produced from different milling processes and different milling times. Metal grade silicon powder was produced using a high energy orbital pulverizer for different milling times of ½, 1, 2, and 3 Hrs. A low energy ball mill with steel and zirconia ceramic media was also used

to produce powder from metal grade silicon. In both cases the powder-to-ball mass ratio was 1:20 and the milling proceeded for up to 6 weeks.

6.1.3.1 Zirconia ball milled silicon powder

The Raman spectrum for powder samples milled with zirconia balls for 1, 2 3, 4, and 7 days are given in Fig. 6.8, without background correction. The broad band extending from 700 cm^{-1} to 1400 cm^{-1} is due to fluorescence, and can be attributed to an inherent property of the material. This in turn increases the background particularly when a longer integration time is used, consequently obscuring both the second order silicon and oxide peaks around 950 cm^{-1}. From the experiment, a trend of increasing fluorescence with increasing milling time was observed. Also the intensity of second order peak around 950 cm^{-1} was observed to decrease which could imply an increase of an oxide phase.

University Of Cape Town

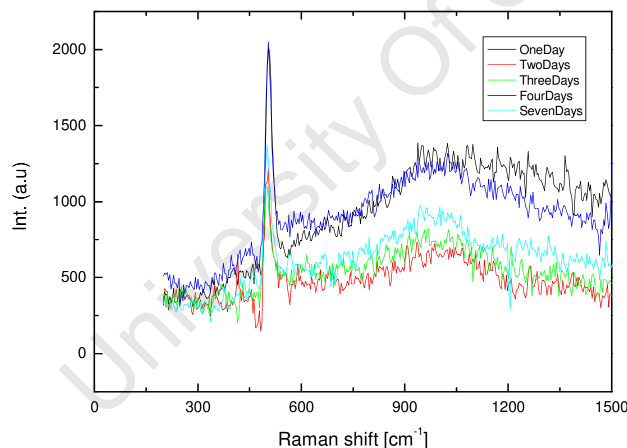

Fig. 6.8: Raman shift for Zirconia ball milled silicon powder without background correction.

The analysis was performed by fitting the spectrum around the visible peaks at 950 cm^{-1} with two Gaussians components. The integrated area was used as an inverse indicator for the presence of an oxide layer. It is noted that the intensity of

the second order silicon peak for the one day milled powder was the highest and decreased rapidly over two to three days milling. There seems to be a slight increase for longer milling times, as shown in Fig. 6.9.

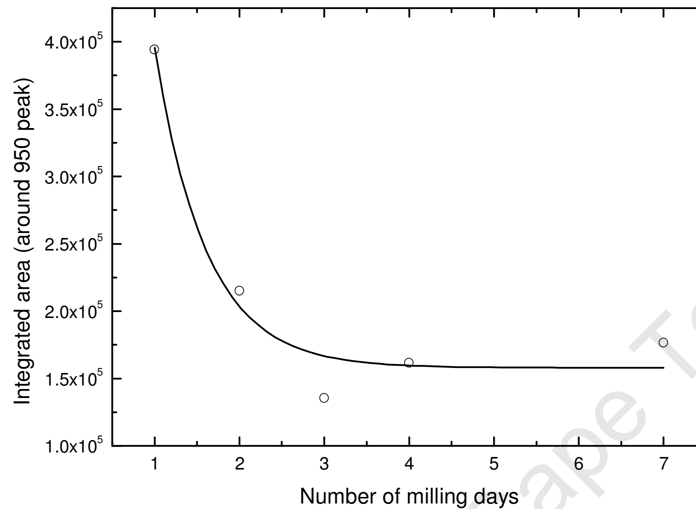

Fig.6.9: oxygen content indicator for Zirconia hardened ceramic ball milled silicon powder.

University Of Cape Town

The database obtained from *www.rruff.info* [4] was employed for the interpretation of the spectrum. Accordingly 50 peak positions were identified for silicon oxides which may be grouped further in to seven materials: opal, quartz, tridymite, coesite, stishovite, cristobalite and melanophlogit. These are all silica but differ in their oxygen coordination, and formation pressures and temperatures [5]. As indicated in **Appendix C** the possible Raman shift positions span a wide range from 179 to 1240 cm^{-1}.

The Raman spectrum given in Fig. 6.10 is from a powder milled for nine days, after background correction, with the stishovite spectrum [4] for reference. The arrows are used as a guide to the eye where similarity prevails. It is clear from this spectrum that the zirconium milled silicon contains a minor phase which appears to be stishovite-like.

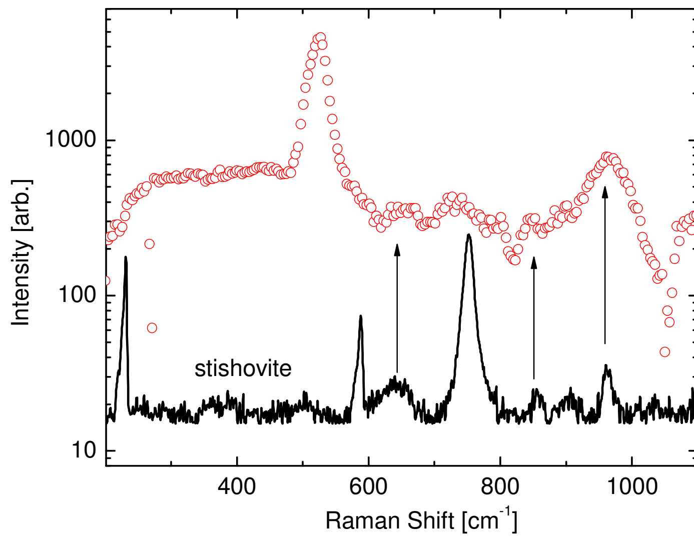

Fig. 6.10: Raman shift for zirconia ball milled Si, (open circles) compared with stishovite (continuous line).

6.1.3.2 Steel ball milled silicon powder

The spectrum presented in Fig. 6.11 is for silicon milled for 10 days using steel balls. The trend of increasing fluorescence with milling time still persists, and the reduction in the intensity of the second order peak was also noted. When compared with the spectra from the database, the background spectrum of appears partially like coesite and partly like stishovite.

University Of Cape Town

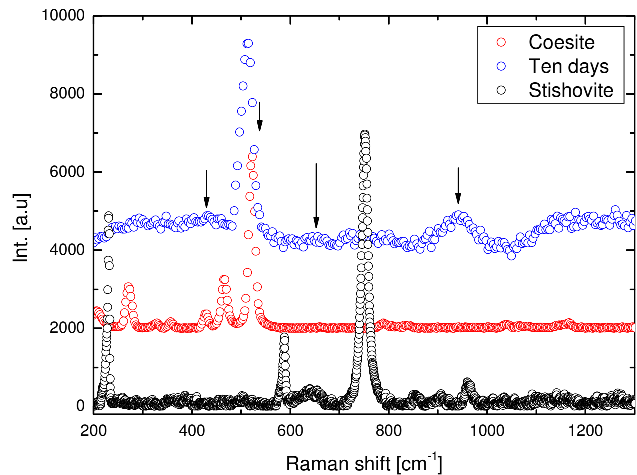

Fig. 6.11: Raman spectrum for metallurgical Si milled with stainless steel balls for ten days as compared with coesite and stishovite spectra.

6.1.3.3 High energy milled powder

The Raman spectrum for powder milled for different durations is presented in Fig. 6.12 after background subtraction. Unlike for the low energy milled powders, there was little or no contribution from fluorescence.

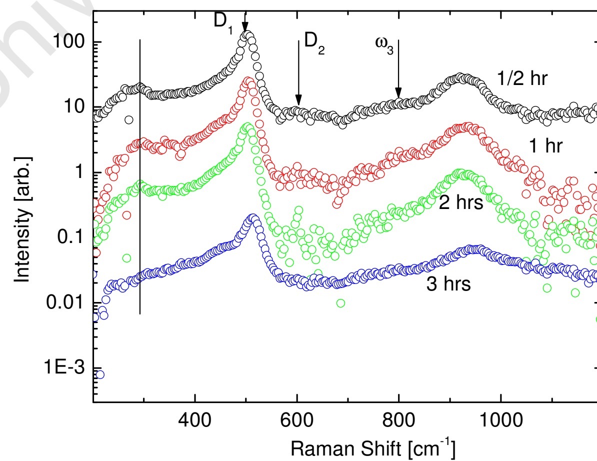

Fig.6.12: Raman shift from high energy milled powder.

University Of Cape Town

The prominent peak around 510 cm^{-1}, could be the first order silicon peak shifted to lower wavenumber on account to its crystallite size. The low frequency band around 300 cm^{-1} which also decreases with milling time, may be a silica band associated with coesite and/or tridymite. The discrete bands associated with *a*-SiO_2, and defined as D_1 and D_2, [6, 7], respectively at 495 cm^{-1} and 606 cm^{-1} are indicated. The band around 800 cm^{-1}, denoted as ω_3, is attributed to the stretching vibration of Si-O in *a*-SiO_2 [7]. The Raman shift corresponding to D1 in coesite is very close to the first order silicon peak which makes it difficult to gauge its contribution to the total intensity.

6.2 Layer structural characterization

SEM and SAXS were the two main techniques applied to study the morphology and particle distribution in the printed layers.

6.2.1 Scanning electron microscopy

Micrographs of hand printed metallurgical and P type Si in linseed oil are shown in Fig. 6.13.

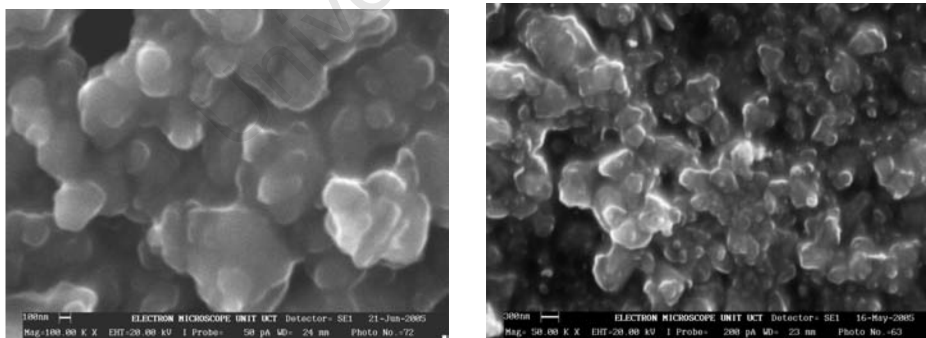

Fig.6.13: SEM micrograph of hand printed a) metallurgical and b) P-type silicon.

University Of Cape Town

These micrographs reveal the presence of clusters, and even clusters of clusters which form a complete network. Percolation principles may therefore be applicable in the discussion of the flow of charge carriers between two points.

6.2.2 Result from SAXS

The curves given in Fig. 6.14 are typical examples of SAXS spectra for free standing layers. The Beaucage universal equation, Eqn. 5.23, [8] was used to fit the data, and is represented by a solid line. An envelope function with no relevant physical information was also introduced to account for absorption in the beam stop at low q near to the primary beam. This envelope function consists of an error function, with its peak position and width as free parameters.

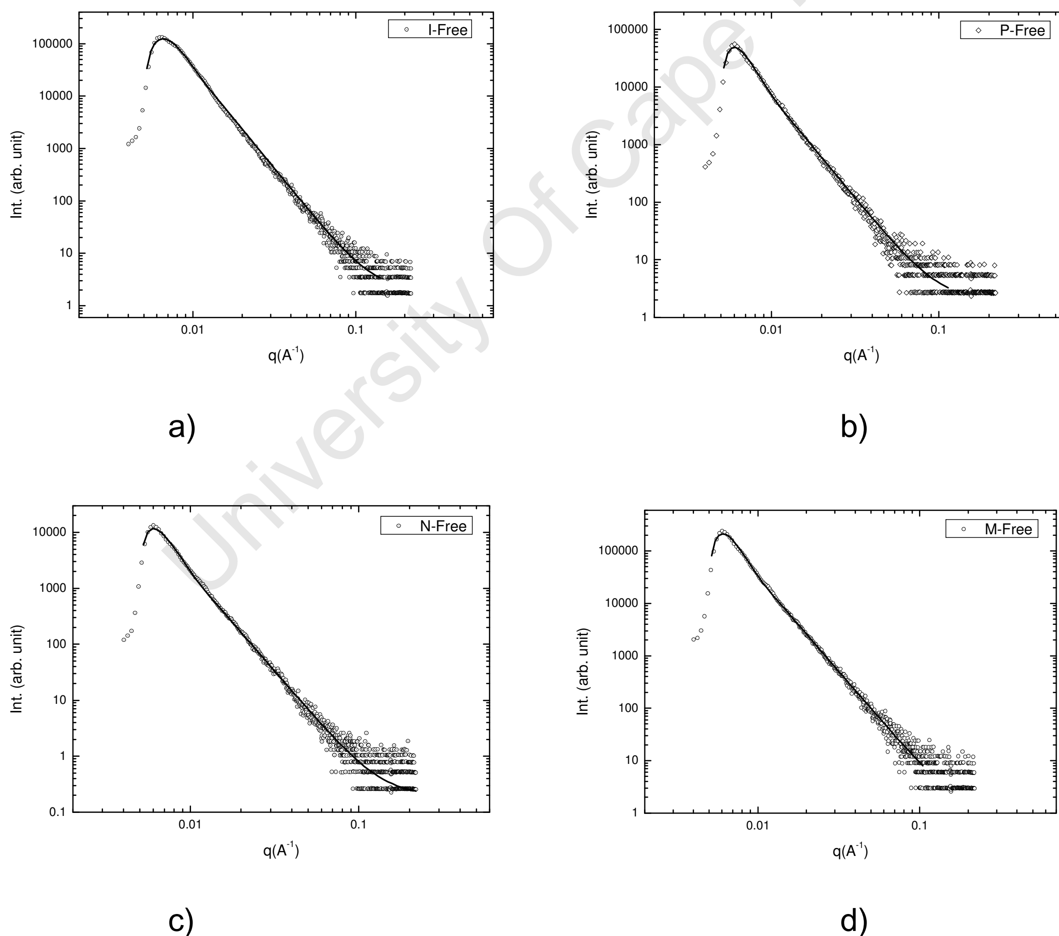

Fig. 6.14: Small angle scattering curves for free standing layers: a) intrinsic; b) P-type; c) N-type; and d) metallurgical silicon. The solid lines represent a fit to a unified model [8].

University of Cape Town

Even though there appears to be some structure in the data for the intermediate q region, it is not significant enough to extract meaningful information. As a result a single structural level was assumed to fit the data with Beaucage's unified equation. The radius of gyration and the fractal dimension extracted from the fitting are presented in Table 6.2.

Table 6.2: Radius of gyration and fractal dimension obtained from a unified fit [8] to the data shown in Fig 6.15.

sample	Radius of gyration (nm)	Fractal dimension
P-Free	44.56 ± 2.48	2.24 ± 0.07
N-Free	43.22 ± 1.83	2.39 ± 0.05
I-Free	28.89 ± 0.39	2.27 ± 0.12
M-Free	39.46 ± 1.18	2.34 ± 0.07

University of Cape Town

The milled powders have fairly equal radii of gyration but for intrinsic silicon it is significantly smaller. The fractal dimension for all the powders falls between 2 and 3.

One advantage of the unified model is that constants such as the Guinier and Porod prefactors, G and B respectively, are important parameters which can be used to estimate the nature of the size distribution and the magnitude of the dispersion. For a system of spheres of uniform size, an approximate relationship between B and G can be given as [9, 10]

$$B = \frac{9}{2}\frac{G}{R^4} = \frac{81}{50}\frac{G}{R_G^4}, \tag{6.1}$$

where R is the radius of the particle and R_G is the radius of gyration. Hence, the polydispersivity index (PDI) can be defined as

$$PDI = \frac{50}{81} R_G^4 \frac{B}{G}, \tag{6.2}$$

so that PDI = 1 for a monodisperse distribution of spheres. Hence if the PDI is close to unity, the particles in the system have a regular size and shape. But a PDI which deviates much from unity indicates the presence of various sizes in the distribution.

The polydispersivity index PDI is calculated using the parameters obtained from the fitting. The parameter denoted as B, the Porod prefactor, is very small with an error of the same order of magnitude of its value. As a result, the error calculated for PDI is exaggerated, and a constrained fit with other parameters kept fixed was required to obtain the values and error estimates shown in Fig. 6.15.

The log- normal size distribution is given by [9],

$$f(R_G) = \frac{1}{R_G \sigma \sqrt{2\pi}} \exp\left(-\frac{\ln R_G - \ln m}{2\sigma^2} \right), \tag{6.3}$$

where m is the median size. The logarithmic standard deviation σ for a distribution of spheres can be derived from the polydispersivity index as [10],

$$\sigma = \sqrt{\frac{\ln(\mathrm{PDI})}{12}} . \tag{6.4}$$

University of Cape Town

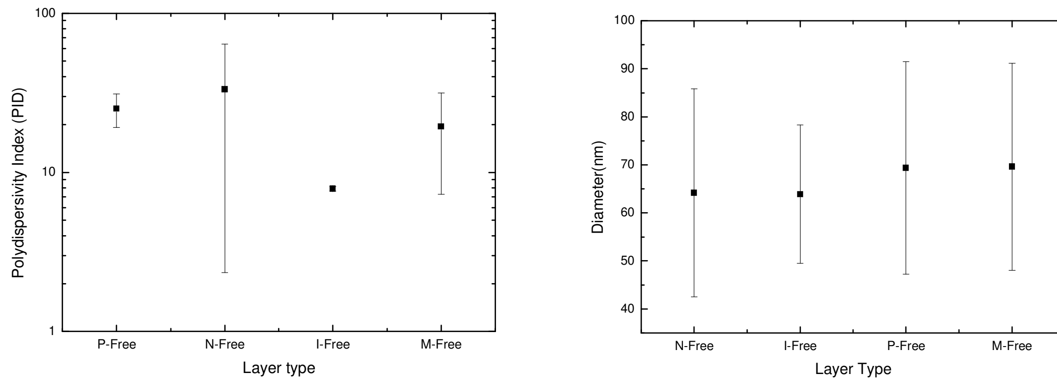

Fig. 6.15: a) Polydispersivity index and b) an estimate of particle size distribution for free standing layers of silicon.

The median value of the distribution, m which is an important parameter to determine the linear standard deviation, ξ, is given by

$$m = R_G e^{\frac{-\sigma^2}{2}} . \tag{6.5}$$

The linear standard deviation ξ is then given as

$$\xi = R_G \sqrt{e^{\sigma^2} - 1} , \tag{6.6}$$

which is used to present the distribution of the particles. As can be seen from Fig. 6.15 the intrinsic silicon has a narrower dispersion than the milled powders which on a relative scale have the same spread of sizes. This result is consistent with the result from TEM.

The GNOM package [11] was also used to analyze the SAXS data for the free standing layers. The fits were very good as presented in Fig. 6.16, and the radii of gyration extracted from the analysis (Table 6.3) also agree reasonably well with the previously determined values.

University Of Cape Town

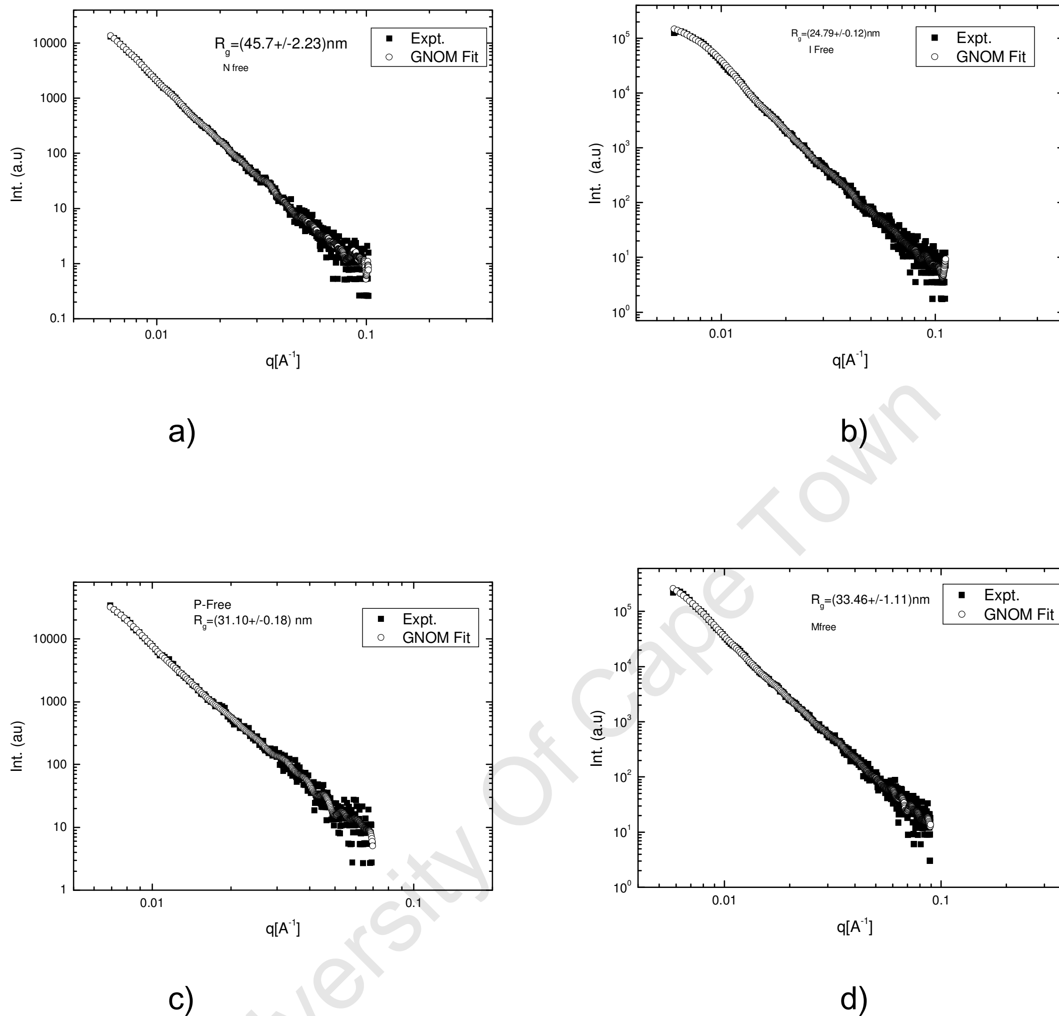

Fig.6.16: Fits of SAXS scattering using the GNOM package for free standing layers of: a) N-type; b) intrinsic; c) P-type; and d) metal grade silicon.

For all the curves shown in Fig. 6.16, the intermediate q region was considered in applying Porod's law to determine the scaling factor presented in Table 6.3 for all the curves. The coefficient falls between 3 and 4, indicating a surface fractal scaling in agreement with the previous analysis method.

University Of Cape Town

Table 6.3: Summary of the results of GNOM fitting to the free standing layers.

Sample	Radius of gyration (nm)	Porod exponent (α)	Fractal dimension
P-Free	31.10 ± 0.18	-3.69 ± 0.02	2.42 ± 0.01
N-Free	45.72 ± 2.23	-3.57 ± 0.02	2.25 ± 0.01
I-Free	24.79 ± 0.12	-3.78 ± 0.02	2.22 ± 0.01
M-Free	33.46 ± 1.11	-3.64 ± 0.02	2.36 ± 0.01

Because the two methods yield similar results, the analysis for the second set of samples printed on cellulose substrates was only performed using Beaucage's unified equation. As described in section 5.2, all the background correction and subtraction of the contribution from the substrate and the sample holder were performed before the analysis. A summary of the parameters determined is presented in Table 6.4.

University of Cape Town

Table 6.4: The SAXS analysis of different powders in different binders. I stands for intrinsic, M for metallurgical and P for P-type silicon, and LIN for linseed oil, CAB for cellulose acetate butyrate, PS for Polystyrene and ACR for Acrylic.

Material	Porod exponent (α)	Radius of gyration (nm)	Fractal type and dimension	PDI
I-ACR	-3.98 ± 0.01	31.29 ± 0.45	2.02 ± 0.01, surface	1.47 ± 0.15
I-PS	-3.94 ± 0.22	28.30 ± 0.54	2.06 ± 0.12, surface	2.27 ± 2.06
I-LIN	-3.98 ± 0.01	30.05 ± 0.39	2.02 ± 0.01, surface	1.52 ± 0.14
I-CAB	-3.99 ± 0.15	27.98 ± 0.35	2.01 ± 0.08, surface	1.88 ± 1.22
M-LIN	-3.84 ± 0.05	36.42 ± 0.47	2.16 ± 0.03, surface	4.07 ± 0.97
M-CAB	-3.34 ± 0.05	35.05 ± 0.49	2.66 ± 0.04, surface	37.29 ± 12.31
M-PS	-3.77 ± 0.07	34.89 ± 0.75	2.23 ± 0.04, surface	6.09 ± 2.11
M-ACR	-2.69 ± 0.03	34.96 ± 0.38	3.31 ± 0.02, mass	841.64±111.22
P-CAB	-3.44 ± 0.09	34.39 ± 0.73	2.56 ± 0.07, surface	22.12 ± 8.84
P-ACR	-3.52 ± 0.12	35.01 ± 0.87	2.48 ± 0.08, surface	10.47 ± 7.26
P-LIN	-3.17 ± 0.11	33.80 ± 0.76	2.96 ± 0.10, surface	60.06 ± 29.87
P-PS	-3.58 ± 0.11	33.84 ± 0.82	2.42 ± 0.07, surface	11.28 ± 5.85

University of Cape Town

The low PDI indicates that the size distribution of intrinsic silicon remains close to monodisperse regardless of the binder type used. Therefore it is reasonable to represent the characteristic size of any powder by the mean value of the gyration radius obtained disregarding the binder type. The intrinsic powder shows relatively small particles whose average radius of gyration may be taken as 29.41± 0.04 nm. For the metallurgical silicon in all binders, the average radius of gyration is 35.3 ± 0.5 nm, and for the P type silicon it is 34.2 ± 0.8 nm. The radius of gyration for the P type and metallurgical silicon is almost the same. If we assume the average value of the two to represent the size of each, it is possible to estimate the important parameters of the size distribution using the

conditions given in Eqns. 6.2, 6.3 and 6.4. Accordingly for the intrinsic silicon we get the logarithmic standard deviation, for a PDI value of 1.52, as 0.035. The median value of radius of gyration is equal to 30.03 nm. For the P and M material, if we consider a PDI = 22.12 as representing them, excluding M-ACR the logarithmic standard deviation is 0.26. The median value of the radius of gyration is 33.26 nm. Table 6.5 summarizes the result for all parameters, which are represented graphically in Fig. 6.17.

Table 6.5: Summary of parameters for all the layers on substrates.

Material	Radius of gyration (nm)	Median radius of gyration (nm)	σ	$\pm 3\sigma$	Linear standard deviation ξ
I-ACR	31.29 ± 0.45	31.28	0.03	±0.09	0.94
I-PS	28.30 ± 0.54	28.2	0.07	±0.21	1.98
I-LIN	30.05 ± 0.39	30.03	0.035	±0.11	1.05
I-CAB	27.98 ± 0.35	27.94	0.053	±0.16	1.48
M-LIN	36.42 ± 0.47	36.16	0.12	±0.36	4.39
M-CAB	35.05 ± 0.49	33.51	0.30	±0.9	10.76
M-PS	34.89 ± 0.75	34.50	0.15	±0.45	5.26
M-ACR	34.96 ± 0.38	29.89	0.56	±1.68	21.22
P-CAB	34.39 ± 0.73	33.25	0.26	±0.78	9.09
P-ACR	35.01 ± 0.87	34.34	0.196	±0.59	6.93
P-LIN	33.80 ± 0.76	31.90	0.34	±1.02	11.8
P-PS	33.84 ±0.82	33.17	0.20	±0.6	6.84

In Fig. 6.17, the error bars indicate the linear standard deviation with the data points representing median values. As can be seen intrinsic silicon as has a narrow size distribution whereas both P and M type have more or less the same distribution range. The erratic behavior for the M-ACR still appears.

University of Cape Town

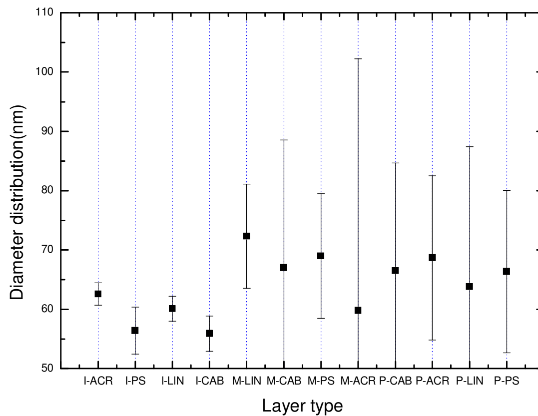

Fig. 6.17: The Particle size distribution with the points representing the median values and the error bars indicating the linear standard deviation.

6.3 Preliminary electrical characterization of silver ink

Silver paste (DuPont 5000) was studied for its electrical response, to investigate its suitability for making electrical contacts. The drying time of printed silver layers was first reported in the postgraduate diploma project of Hind A. Ahmed [12]. The evolution of the resistance of a silver layer as a function of time is as shown in Fig. 6.18.

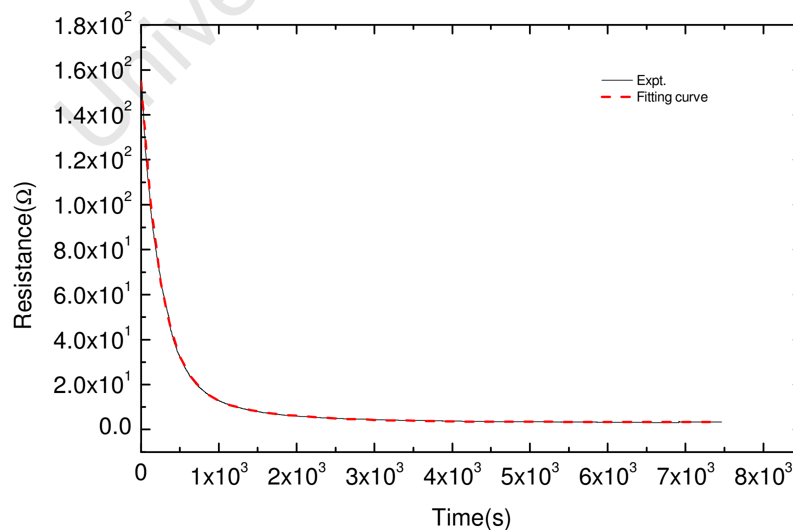

Fig. 6.18: Resistance measurement as a function of time.

University of Cape Town

The time dependence of the resistance can be described by two exponential functions. Accordingly the curve was fitted to a sum of two exponentially decaying functions given as

$$R = R_o + A_1 \exp\frac{-t}{\tau_1} + A_2 \exp\frac{-t}{\tau_2}, \qquad (6.6)$$

where τ_1 and τ_2 are characteristic times, R_o, A_1 and A_2 are constants. The parameters extracted from the curve fit are presented in table 6.6.

Table 6.6: Time dependent parameters for the curing of silver paste.

Parameter	Value
τ_1	(244.78 ± 0.44) s
τ_2	(1018.45 ± 7.37) s
A_1	(132.49 ± 0.18) Ω
A_2	(19.67 ± 0.20) Ω
R_o	(3.27 ± 0.01) Ω

University Of Cape Town

The two time constants represent the two major processes taking place during the curing, which are the polymerization of the binding polymer and the rate at which the solvent evaporates. The shortest time constant could be associated with the evaporation of the solvent, whereas the longer time constant could possibly be for the polymerisation process. The time required for the layer to dry in this sample was about two hours. Obviously the drying time is thickness dependent, the thicker the layer the longer time it will take.

Applying heat can shorten the drying time and improve the conductivity of layers. This was confirmed by a simple resistance measurement experiment conducted on a layer before and after heat treatment. Before heat treatment the resistance between the end points of a 10 mm x 5 mm layer was measure as $(1.00 \pm 0.03)\Omega$.

Later the layer was kept in an oven at 120 ºC for one hour after which the resistance had fallen to $(0.40 \pm 0.01)\Omega$.

Resistance measurement was also used to study the print quality and uniformity of silver layers, as discussed in chapter 4 and labelled according to the same notation convention. The average resistance value of each block with single and double print cycle is presented in Fig. 6.19. For this particular print setting, a single print cycle may produce thin layers leading to a high resistance. However the resistance of layers deposited in two successive print cycles dropped nearly to a third.

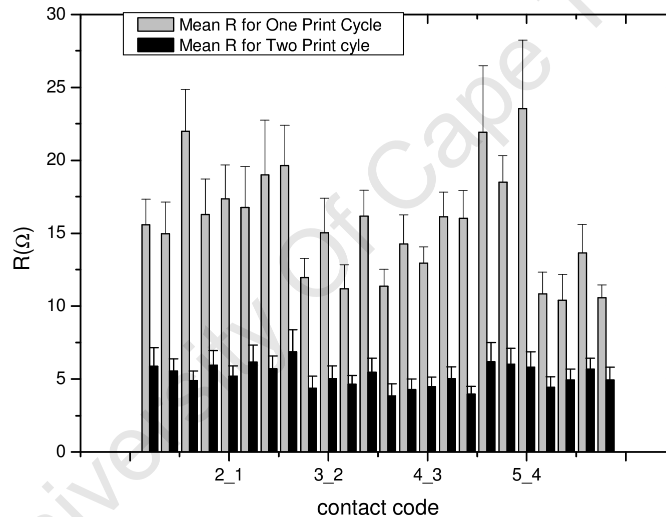

Fig. 6.19: Effect of overprinting on the resistance of silver layers.

This result helped to set a benchmark for the subsequent printing of layers, which was two cycle prints. Overprinting also ensured the uniformity of the layers, minimizing the risk of pinholes.

The eventual application of silver is to contact the silicon layers to the outside world. In general there are only two possibilities to make metal contacts to a printed layer: top or bottom contacts. The difference between the two approaches

University of Cape Town

was investigated by a current sweep method applied to generate the VI characteristic curves from which the resistance values were calculated. Fig. 6.20 shows a few representatives of VI curves to indicate in general the behaviour.

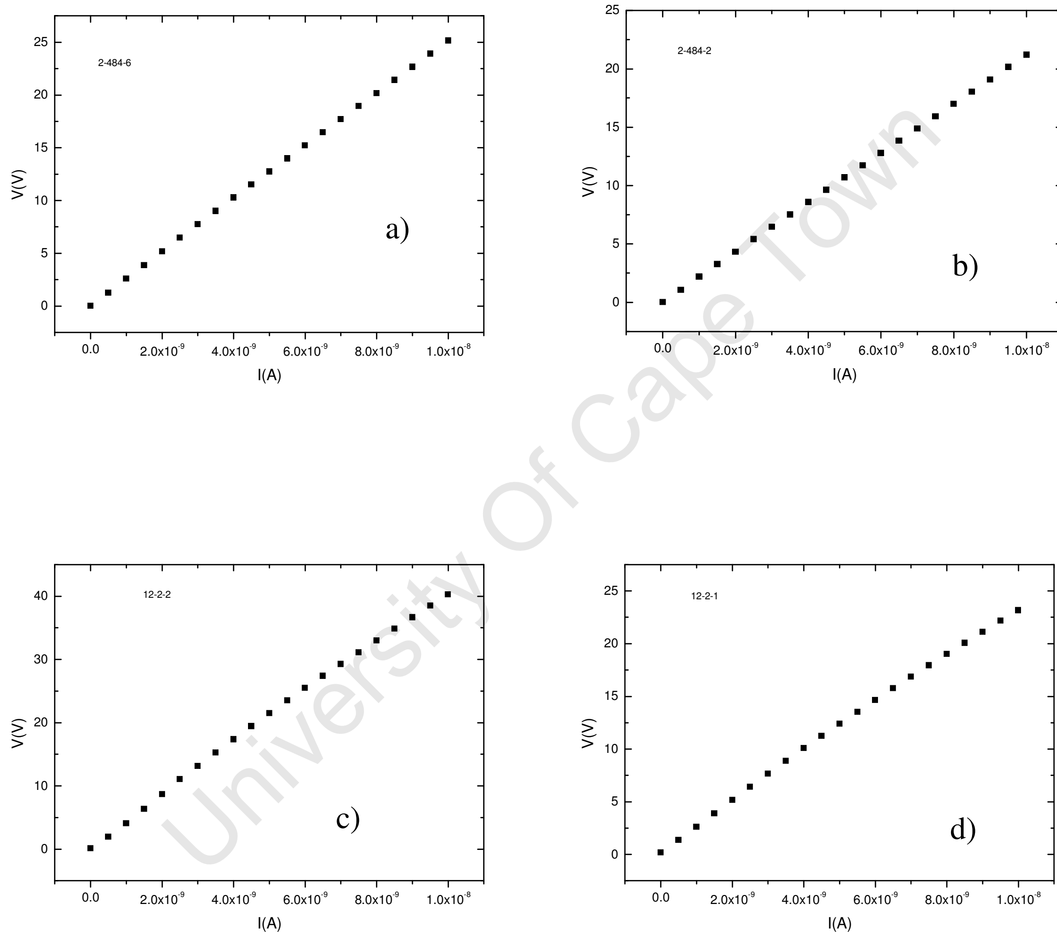

University Of Cape Town

Fig 6.20: Characteristic curves for the bottom contact, a) and b) and top contacts c) and d)

Such curves were obtained for about 200 different samples. All the curves were fairly linear or ohmic. Ohmic behaviour is a required property of the contact, especially when the result from the IV measurement is to be used for the analysis of other electrical parameters using the Hall effect method, which ensures the

reliability of the analysis. A summary of all the measurements is given in table 6.7.

Table 6.7: Resistances of silicon layers with top and bottom contacts.

Ink Type	Average resistance of the device (GΩ)			
	Linseed Oil		CAB	
	Top Contact	*Bottom Contact*	*Top Contact*	*Bottom Contact*
i-si	4.62 ± 1.11	1.58 ± 0.24	5.90 ± 1.09	1.45 ± 0.06
M-si	4.72 ± 0.46	2.67 ± 0.48	4.74 ± 1.38	2.44 ± 0.37
P	3.28 ± 0.74	1.77 ± 0.53	3.28 ± 0.74	1.77 ± 0.53

University Of Cape Town

For all samples, layers with top contacts had higher resistances. This could be explained in terms of the level of porosity of the underlying layer which absorbs the liquid. In the bottom contact, silver is directly printed on the paper substrate which is porous and absorbs the liquid components of the silver ink exposing the metal on the top. But the situation is different for the top contact. The metal is printed on the silicon layer which is not an efficient absorber of the liquid. As a result the ink undergoes a segregation process, which may form an insulating layer that could contribute to rise in the resistivity. The result is therefore an indicator for the procedures to be followed for subsequent sample preparation.

6.4 Hand printed oil based silicon inks

Oil based silicon inks proved to be only suitable for hand printing. The following subsections deal with the characterization of hand printed layers of different inks.

6.4.1 Hall effect studies of hand printed layers

The Hall effect studies of hand printed layers were carried out with the home built system for which the description was given in the previous chapter. The actual measurements were IV characteristic curves to determine the resistivity of each sample and their corresponding Hall voltages. Accordingly the electrical quantities determined from each material are summarized in table 6.8. In the table, sample i-Si refers to sample from commercially obtained powder produced by pyrolysis. The N-type silicon and P-type silicon refers to samples from powders of milled wafers, whereas M-Si refers to sample from powder of milled metallurgical silicon as stated in chapter 4.1 of this thesis.

University of Cape Town

Table 6. 8: Hall effect measurement result for four types of nanopowder in different volume of linseed oil [13]. The i-Si refers to sample of intrinsic silicon from pyrolysis, P-type silicon refers to sample produced from milled P type wafer, N-type silicon refer to sample from milled N type silicon wafer and M-Si refers to sample from milled metallurgical silicon.

Nano powder	Particle vol. fraction (%)	Resistivity (MΩcm)	Hall mobility $cm^2V^{-1}s^{-1}$	Type	Carrier conc. ($\times 10^{12}$ cm^{-3})
i-Si	92	0.67 ± 0.07	2.80 ± 0.44	n	3.30 ± 0.40
N-type silicon	88	0.26 ± 0.01	1.60 ± 0.29	n	15.00 ± 0.27
	90	0.29 ± 0.01	1.90 ± 0.15	n	11.00 ± 0.07
	92	0.32 ± 0.02	1.20 ± 0.09	n	17.00 ± 0.09
P-type silicon	88	130 ± 1.10	0.12 ± 0.03	p	0.41 ± 0.09
	90	15.50 ± 1.10	0.15 ± 0.03	p	0.26 ± 0.06
	92	16.20 ± 1.20	0.45 ± 0.09	p	0.86 ± 0.18
M-Si	91	2.22 ± 0.16	0.65 ± 0.06	n	4.30 ± 0.42

The intrinsic and metallurgical Si materials are not intentionally doped, and in principle both types of carrier are expected to coexist. But since electrons have a

lighter effective mass and hence attain higher mobility, the material behaves as an N-type material. The Hall effect in the same batch of metallurgical Si was independently characterized at Lakeshore Cryotronics Inc. Three samples named as sample 1, sample 2 and sample 3 with thicknesses of about 30 μm, 30 μm and 60 μm respectively were provided. The surface area of each was 5 x 10 mm^2. Table 6.9 presents the results from Lakeshore.

Table 6.9: Result for the Hall effect measurement at Lake Shore Cryotronics, Inc. [14]

Device	Sheet Res. [ohm/sqr]	Sheet Hall Coef.[cm^2/C]	Type	Sheet Carrier Density [cm^{-2}]	Hall Mobility [cm^2/Vs]
Sample 1	6.03×10^7	-1.89×10^8	n	3.30×10^{10}	3.02
Sample 2	6.48×10^7	-1.84×10^8	n	3.40×10^{10}	2.96
Sample 3	2.35×10^8	-3.05×10^8	n	2.05×10^{10}	1.32

These results agree with the earlier measurements. For all the samples it was found that electrons are the majority carriers.

The original wafers for both N- and P-type silicon were also characterized since carrier data was not available and the result shown in table 6.10 was obtained.

Table 6.10: The electrical parameters from silicon wafers before milling as characterized in the home built Hall measurement system.

Wafer	Resistivity [Ω cm]	Hall Coef. [cm^3/C]	Type	Carrier Density [10^{19} cm^{-3}]	Hall Mobility [10^{-2} cm^2/Vs]
P-Si	33.88 ± 0.73	0.46 ± 0.19	p	1.36 ± 0.56	1.40 ± 0.60
N-Si	0.36 ± 0.03	$(6.26 \pm 1.38)10^{-4}$	n	42.70 ± 9.40	4.10 ± 0.90

University Of Cape Town

Comparing the results in tables 6.8 and 6.10, it is noticeable that the silicon powders maintained their respective carrier types. The carrier concentration for the N-type material remained higher in both cases. Even though the carrier concentration was reduced drastically in the printed layers, the result from the measurement verified the flow of carriers. This may be achieved through the network formed between the particles or clusters.

The Hall effect measurements on doped intrinsic silicon were an important component of this work. Two different inorganic salts, NaCl and $MgCl_2$ were used for this experiment. The actual measurements were recording of the IV curve and measurement of the Hall voltage using the home-built system. The IV characteristic curves were all ohmic, as shown in Fig. 6.21 for intrinsic silicon doped with NaCl.

University Of Cape Town

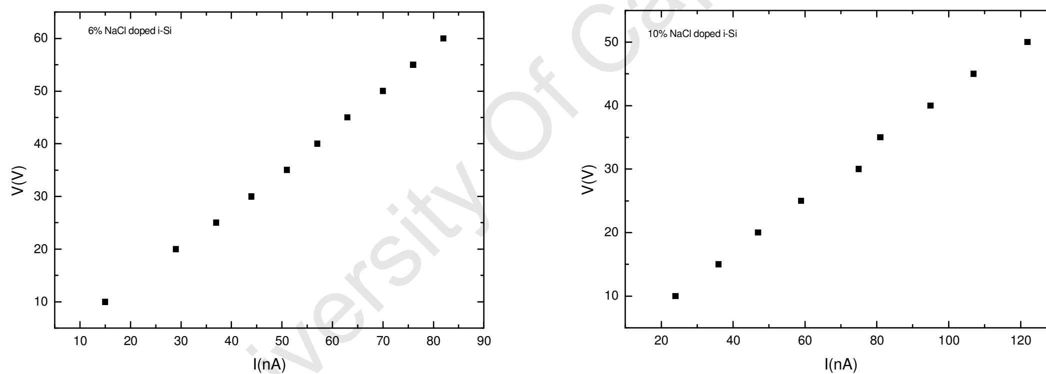

Fig. 6.21: IV graphs for intrinsic Si doped with NaCl prepared for the Hall effect measurement.

The analysis of all other Hall effect parameters was carried out according to the description given in chapter 3. The Hall coefficients as a function of the weight percentage of the respective salt added to the mixture are given in Fig. 6.22 and 6.23. When 2% by weight of NaCl was added, the material remained N type but with a slightly lower carrier concentration than when undoped. As the dopant concentration increased above 2%, the carrier type shifted from N type to P type. But the Hall coefficient decreases with the dopant concentration attaining the

minimum when the dopant concentration maximum at 10%, and yet remaining P type material as shown in Fig. 6.22.

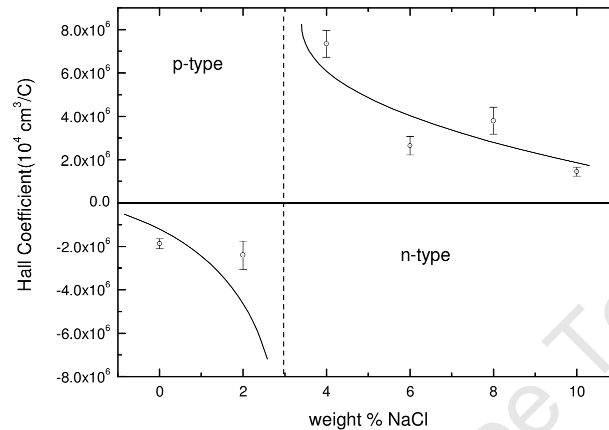

Fig.6.22: Hall coefficient of silicon nanoparticulate doped with ionic salt NaCl. The solid line is guide to eye to show the trend. The sign of coefficient shows the carrier type.

Doping with $MgCl_2$ more or less followed the same trend as doping with NaCl (Fig. 6.23). At a doping level of 4% by weight of $MgCl_2$ it was not possible to measure any decisive result but as the doping level increased above 4%, the carrier type shifted from N- type to P-type. The resistivity slightly increased with the doping level. However when the doping level reached 20%, the original carrier type was restored.

University of Cape Town

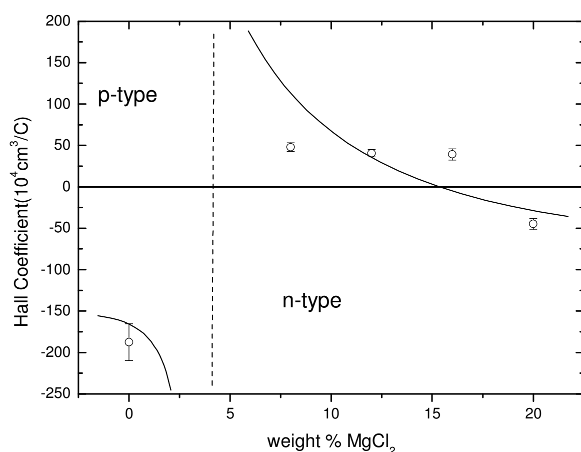

Fig.6.23: Hall coefficient of silicon nanoparticulate doped with ionic salt $MgCl_2$. The solid line is guide to eye to show the trend. The sign of coefficient shows the carrier type.

University Of Cape Town

Unlike NaCl, the second salt $MgCl_2$ and other salts did not yield stable electrical characterstics. This could be attributed to the hygroscopic nature of salts. Figure 6.24 shows how the current was continuously changing in a silicon layer doped with $MgCl_2$.

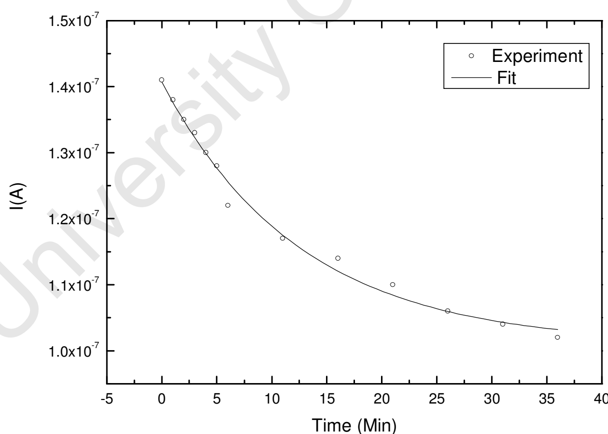

Fig. 6.24: Decaying of current for constant applied voltage.

A constant voltage of 60V was applied between the contacts along its length and the current was monitored. It was noticed that current fell exponentially with time. This may be an indicator that $MgCl_2$ is more hygroscopic than NaCl, with the characteristic time possibly representing the drying time of the layer. In the Hall

effect measurements, the system had been given longer time for the current to stabilize before proceeding with the measurement.

Fig. 6.25: Sodium iodide is too hygroscopic to be used in this experiment.

A more dramatic example is shown in Fig. 6.25. Solid granules of sodium iodide were placed in a petri dish and their interaction with the environment was monitored. It was highly hygroscopic, dissolving completely after a short time of exposure to the atmosphere. Such salts were not appropriate for this study and hence excluded.

The addition of an inorganic salt to the metal grade silicon inks was also studied at different concentrations. The samples were prepared in the same way as reported in chapter four. Doped silicon ink was hand printed onto previously printed silver metal contacts, ensuring that the samples had the same dimensions. Resistance measurements were conducted along the length of the sample, and the IV characteristic curves showed an ohmic resistance. Hall effect measurements were not performed on these samples, but a clear trend is seen for the effect of doping on the resistivity.

University Of Cape Town

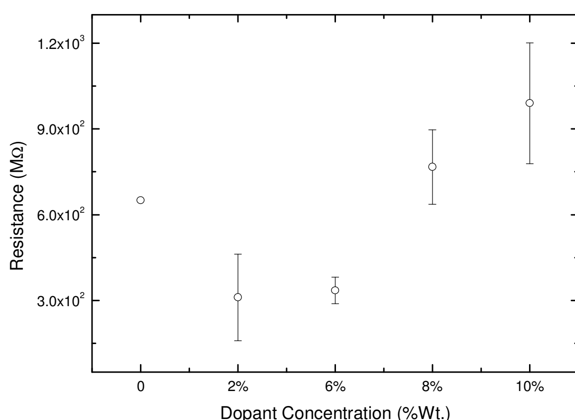

Fig. 6.26: The effect of NaCl doping on metal grade silicon in linseed oil.

University Of Cape Town

Figure 6.26 shows the change in the resistance with increasing doping level. At lower doping level, the material's resistivity falls but starts increasing at higher doping levels. The process may have introduced immobile ions that caused the increase in resistance. Hence this result is presented only to indicate the possibility for further investigation when a screen printable ink is achieved.

6.4.2 Layers in hetero- and sandwich structures

In the earlier experiments doping nominally intrinsic silicon with inorganic salts resulted in P-type behaviour. The single low field Hall measurement verified that the undoped metallurgical Si, in a layer form, is an N-type material. It is therefore interesting to deposit doped and undoped silicon in stack form and test if it exhibits diode like behaviour. At the same time a simple capacitor structure of undoped metallurgical Si between silver top and bottom contacts was produced.

Accordingly the P-type material was prepared for two different doping levels of 4% and 6% NaCl.

In all cases, when the IV measurements were carried out either manually or in the fully automated system, both samples exhibited non-ohmic but broadly symmetric curves.

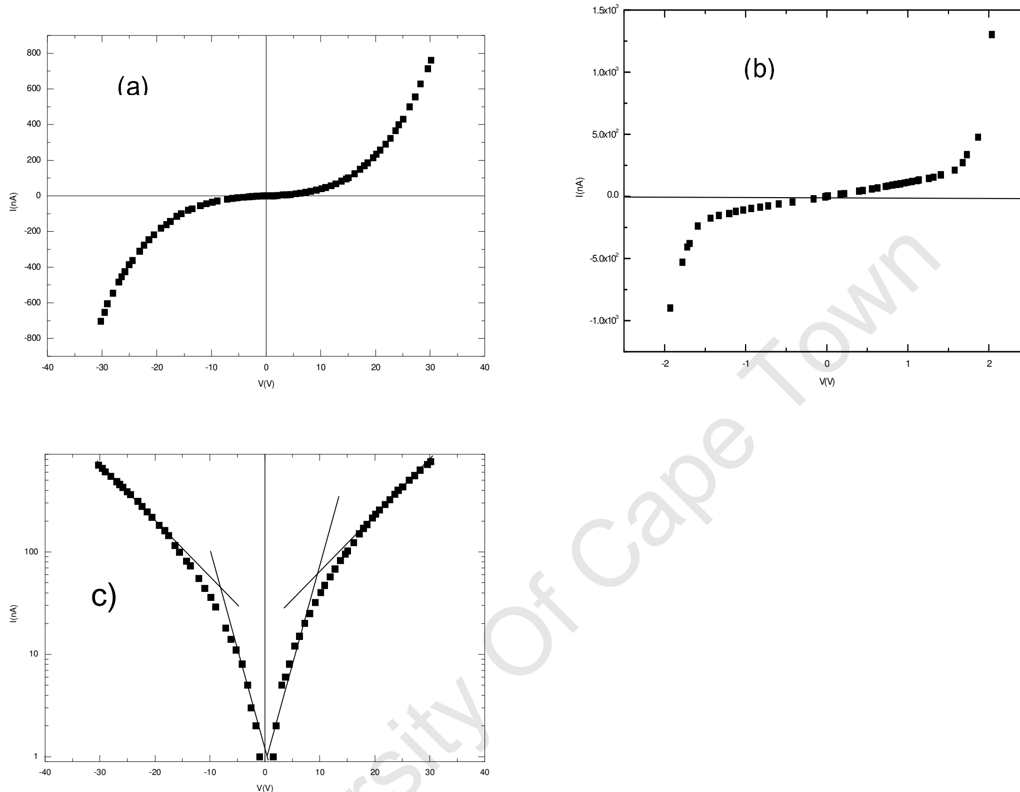

Fig.6.27: The I-V characteristic curve when the doped layer is a) 4% wt. NaCl, b) 6% wt. NaCl, and c) semi log representation of a).

University Of Cape Town

At small bias voltages, irrespective of its sign, the hetero-structure is highly resistive. As the applied voltage increases the current starts to increase exponentially, as seen in Fig. 6.27 a) and b). The semi log plot, Fig. 6.27 c) shows two slopes which indicate the presence of more than one conduction mechanism. At low bias voltage ohmic conduction appears to dominate. The second type of conduction at high electric field can result from space charge limited current [15]. At lower applied voltage the carriers are mainly trapped with the structure acting as a capacitor. But as the potential is increases the trap

region keeps on accumulating excess carriers until finally the barrier ceases and the current flow increases exponentially.

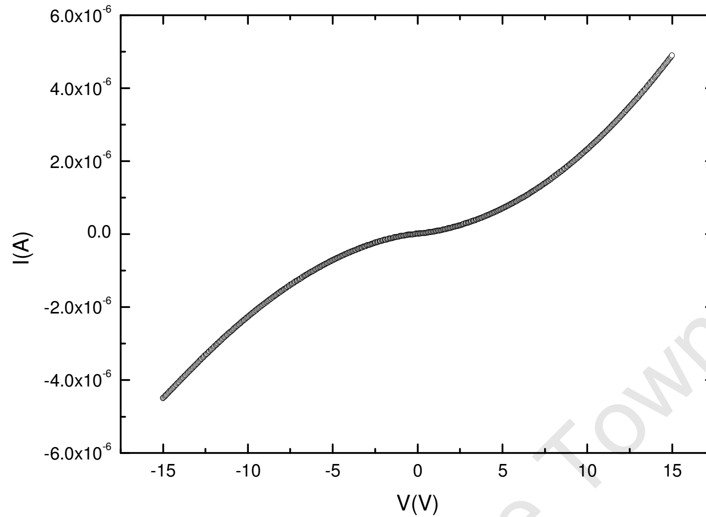

Fig.6.28: The IV characteristic curve for MSM sandwich structure

University of Cape Town

The IV response of the single layer shown in Fig. 6.28 follows the same trend as those presented for the PN structure. The circuit representing the structure can be modeled once one understands the interface properties. From the structure, both sides of the semiconductor were connected to the same kind of metal. If there is a formation of Schottky junction the whole structure represents two back to back diodes. The charge flow mechanism is, as explained earlier, blocking any flow at low bias voltage until the breakdown of the space charge limited current occurs. The equivalent circuit is investigated in more detail using impedance spectroscopy in the next section

6.4.3 Impedance measurement

The impedance of the MSM and PN structures were measured using a HP LF4192A Impedance analyzer. The measuring frequency varied from 500 Hz to $1x10^7$ Hz, set to sweep automatically. The oscillating voltage was set to 100mV for which the resolution is 5 mV. The data acquisition was assisted by a labview

computer program capturing the impedance and the phase angle over the range of frequency of interest. After resolving the impedance into its real and imaginary components Cole-Cole plots were generated. An impedance modeling software called Zview [16] was used to determine an equivalent circuit as well as to determine the values the equivalent circuit components. Zview was used to simulate the bode plot that is equivalent to the experimentally determined value. The circuit components and network that were used to generate simulated data can then be regarded as an equivalent circuit and component values. The Cole-Cole plot, shown in Fig. 6.29, is a typical example for the MSM structure. Irrespective of the sign of the bias voltage, an identical curve was obtained. This result is consistent with the symmetric IV characteristic curve for which conduction is possible irrespective of the bias direction.

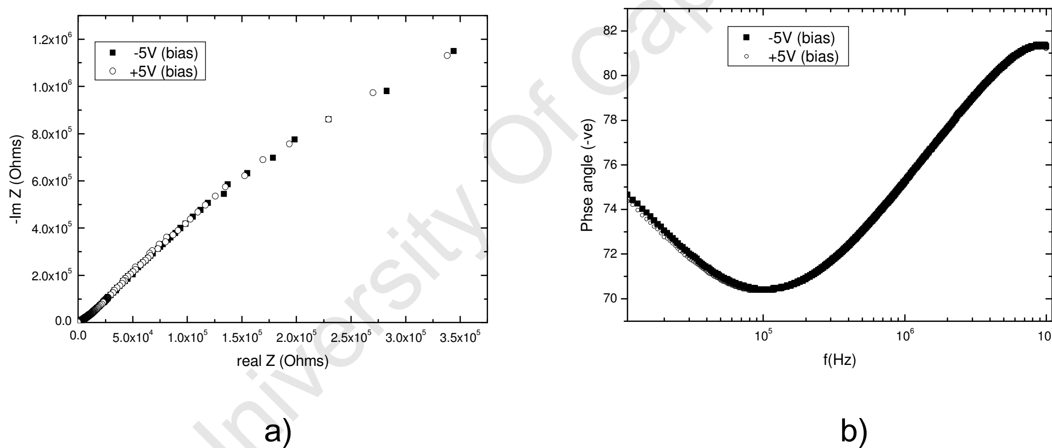

Fig.6.29: a) The Cole –Cole Plot for MSM structure, and b) its corresponding bode plot.

The shape of the curve indicates the presence of parallel capacitors and resistors. When the device was biased with either negative or positive voltage, the section of the semicircle seen remained unchanged in its shape and size, indicates that the dominant capacitance seen is not formed in the depletion layer. A similar behaviour is observed for the PN structure that was characterized, as shown in Fig. 6.30.

University Of Cape Town

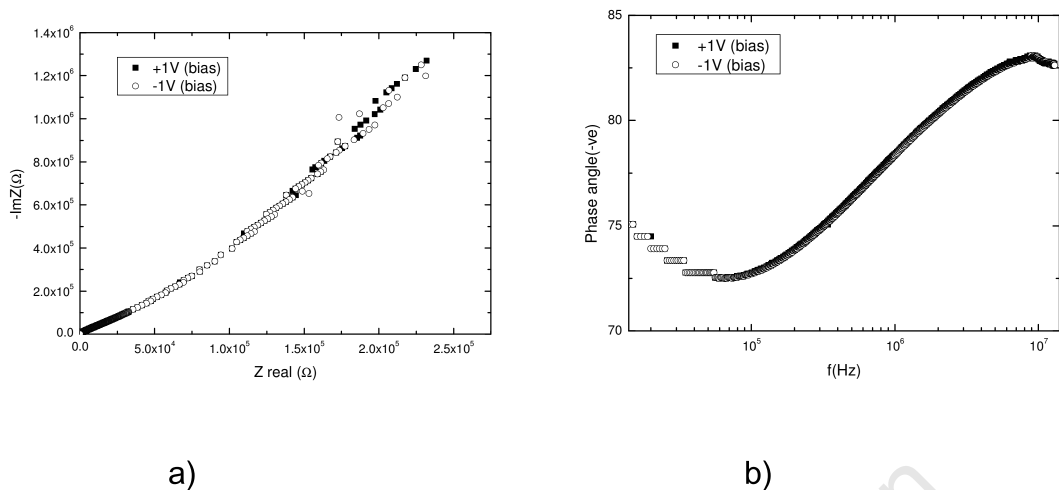

a) b)

Fig.6.30: Fig: The Cole –Cole Plot for PN structure a), and b) its corresponding bode plot.

University of Cape Town

Both the bode and the Cole-Cole plots in Fig. 6.30, result in overlapping curves for the positive and negative bias voltages. This result substantiates the result obtained from the IV measurement. The responses of the structures, MSM or PN junction, are similar in both IV and impedance measurements. This suggests the absence of a defined interface between the P and N layers.

The Zview software was first used to simulate the bode plot for both structures, as shown in Fig. 6.31.

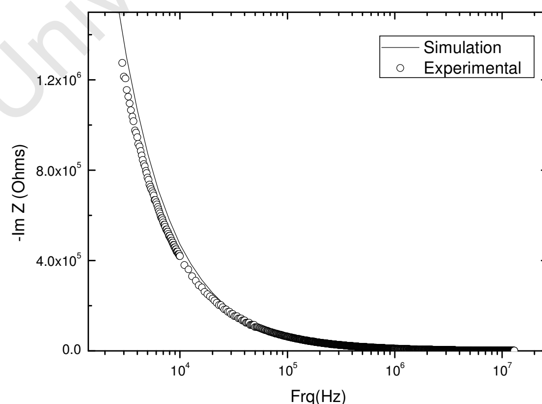

Fig. 6.31: The bode plot for PN structure.

The critical phase angles determined were then used as a reference to decide the best simulated curves. Accordingly, the Cole-Cole plots, shown in Fig. 6.32 were determined for the structures.

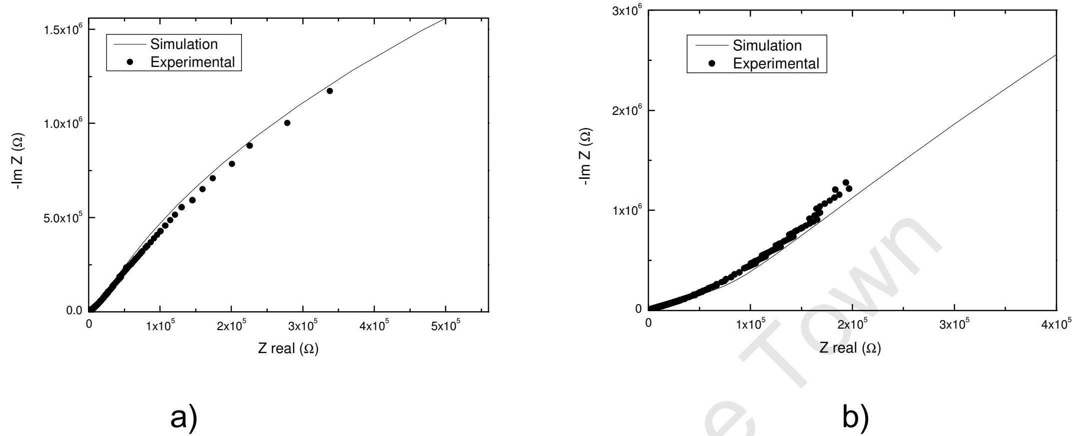

Fig.6.32: The simulated Cole-Cole a) for MSM and b) for the PN structures

The simulated curves agree fairly well with the experimental data. Thus the circuit which is used to generate the simulated curves can be said to represent the structures. The same type of circuit network has been used in both structures to generate the simulated curves, which can be regarded as an indicator for the similarity of the two structures. This circuit is shown in Fig. 6.33.

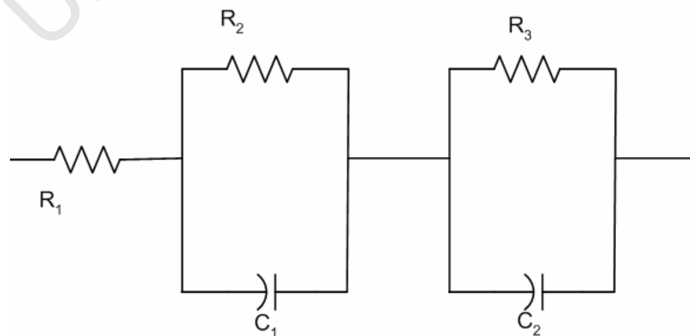

Fig. 6.33: An equivalent circuit for the MSM and PN structures.

University Of Cape Town

In Fig. 6.33, the contact resistance is represented as R_1 whereas the two RC elements in series represent the equivalent resistance and capacitance between the metal and semiconductor, and between semiconducting particles. The estimated values for these elements are given in table 6.11.

Table 6.11: Values of components in the equivalent circuit.

No	Structure	$R_1(\Omega)$	$R_2(k\Omega)$	$R_3(M\Omega)$	$C_1(pF)$	$C_2(pF)$
1	MSM	59	74	10	71.7	294
2	PN	10	66	1000	186	539

University of Cape Town

6.5 Field dependent characterization of bulk material and powders

Field dependent study of the electrical properties of materials is a powerful technique whose rationale is described in chapter 3 of this thesis. The model that was used to analyze the data was tested with a standard sample and with other well defined materials.

6.5.1 Test of model – InAs

The standard sample used for this purpose is an InAs wafer, supplied by Lakeshore Cryotronics, Inc. as a reference material for the operation of Hall Measurement System (HMS). The curves given in Fig. 6.34 demonstrate the fitting of experimental results for InAs.

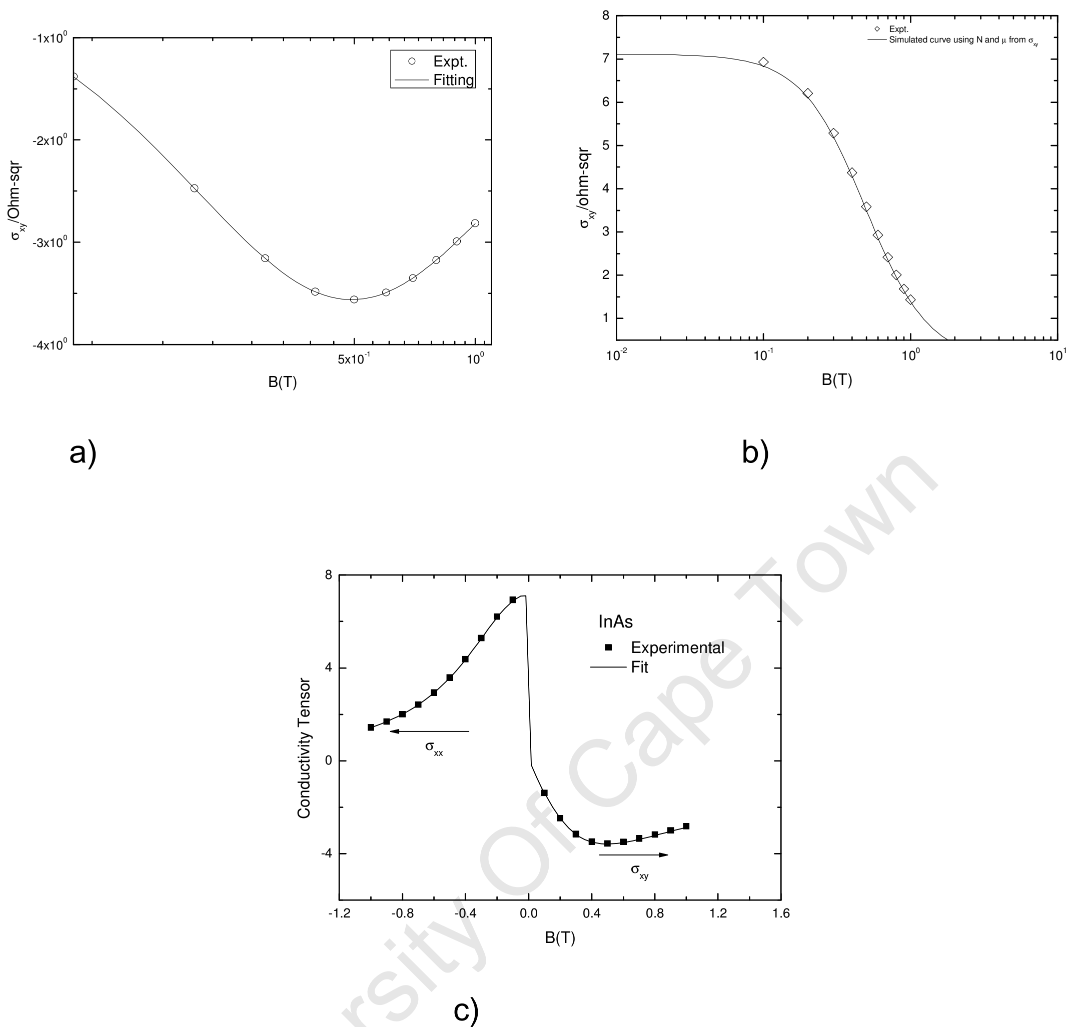

Fig.6.34: Sheet Conductivity Tensors for InAs, a) the transversal b) longitudinal and c) the combined fit.

University of Cape Town

The curve in Fig. 6.34 a) shows the fitting of experimental data to the transversal sheet conductivity tensor (Eqn. 3.88). From the fit it can be established that the material is N-type with sheet carrier density of $(2.18 \times 10^{19} \pm 2.33 \times 10^{16})$ m^{-2} and a mobility of (2.03 +/- 0.02) m^2/V-s. These parameters were substituted back into the expression of the longitudinal conductivity tensor (Eqn. 3.87) to generate the curve given in Fig. 6.34 b). As can be seen from the plots the experimental result and the fit are in very good agreement. The fit from the combined conductivity tensor is presented in Fig. 6.34 c). For the sake of convenience the longitudinal conductivity is plotted on the negative field axis. As demonstrated in the curve,

the fitting is excellent and parameters satisfying both components of the conductivities were extracted as follows. The carriers are electrons with a sheet density of ($2.23 \times 10^{19} \pm 5.89 \times 10^{16}$) m^{-2} with mobility of (2.00412 ± 0.00662) $m^2/V\text{-}s$. The two sets of results agree with 1% and 2% difference in mobility and sheet carrier concentration respectively.

To prove that InAs is a material with a single carrier type, the reduced conductivity tensor was applied, as described in chapter three. The experimental results for the transverse and longitudinal components of the reduced conductivity tensor are plotted in Fig. 6.35.

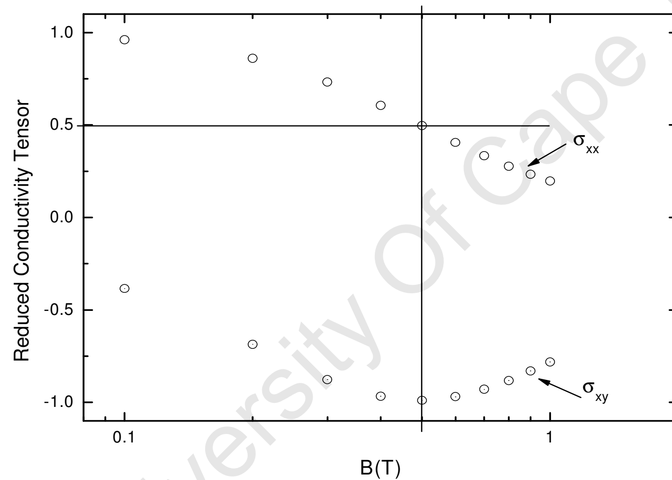

Fig.6.35: The reduced conductivity tensor for InAs.

University Of Cape Town

When the transverse component of the reduced conductivity tensor takes its extremum value, which is the maximum for hole and the minimum for electrons, the corresponding value for the longitudinal component at the same field as acquires a value equal to ½, then the material is said to be single charge carrier. The plot for the InAs given in Fig. 6.35 verifies this condition and hence it can be said that it is a single carrier type material.

6.5.2 Wafers and metal grade silicon

The field dependent magnetoresistivity measurement or Hall effect measurement is the best way of characterization of materials specifically when more than one carrier type is expected [17]. In this work emphasis is given to silicon in its different forms such as wafer, metallurgical chunk, pellets and printed layers. Layers are printed from the ink made of intrinsic, metallurgical, P-type and N-type silicon powder. Three sets of pellets were produced from powders produced via two routes. The P and N type pellets were prepared from the powder produced by high energy milling. A third pellet, denoted P883, was prepared from a phosphorous doped silicon nano powder produced by thermal catalytic pyrolysis [18]. The result from each form of sample will be presented and compared.

University of Cape Town

Before presenting the experimental result, the expected response for silicon was simulated as indicated in Fig. 6.36. The literature value for the intrinsic carrier mobilities at room temperature were used to simulate both holes and electrons. The critical magnetic field which is related to the mobilities is beyond the operation limit of our system which is 1T.

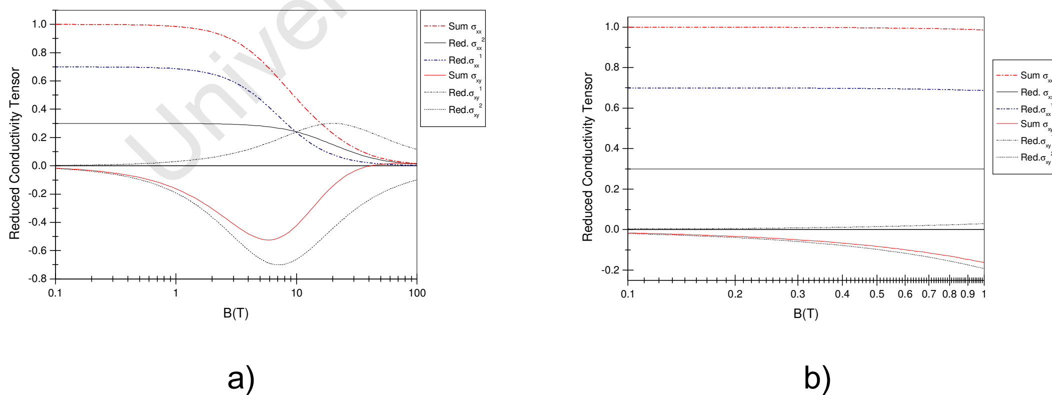

Fig.6.36: Simulated reduced conductivity tensor for silicon at room temperature, for a) the full range of magnetic fields, and b) the range accessible in these measurements.

Figure 6.36 a) shows the nature of the curve over wide range of magnetic field. This suggests that the characteristic field would be above 5 T. Hence direct

reading of the result from the graph is not possible. The expected form of the accessible data is that shown in Fig. 6.36 b). Hence all the results have to be determined from fitting the experimental data to the standard equation of conductivity tensor.

P type wafer: This wafer was supplied by Siltronix AG, Germany. According to the manufacturer's product specification, this wafer is highly boron doped with a resistivity of 0.0008 - 0.001 Ωcm. The wafer has a thickness of between 250 and 300 μm, for which we took 275 μm for the data analysis purpose. A sample with van der Pauw geometry was prepared from this wafer with dimensions of approximately 1 cm x 1 cm x 0.275 mm. The bulk resistivity measurement determined with the HMS yielded ($7.647 \times 10^{-6} \pm 4 \times 10^{-9}$) Ωm which confirms the values stated in the specification. The data captured for the variable field measurement was fitted to the combined conductivity tensor (Fig. 6.37). From the fitting the presence of two carrier types was observed as shown in table 6.12.

Table 6.12 : Summary of the results for the P type silicon wafer.

Carrier Type	Carrier density [m^{-3}]	Mobility [m^2/V-s]
Hole	$2.55 \times 10^{26} \pm 3.88 \times 10^{24}$	$0.00320 \pm 4.23 \times 10^{-5}$
Electron	1.32×10^{21}	9.39×10^{-6}

The contribution of electrons is insignificant when compared to that the holes, but it does indicate the presence of a second carrier type.

University Of Cape Town

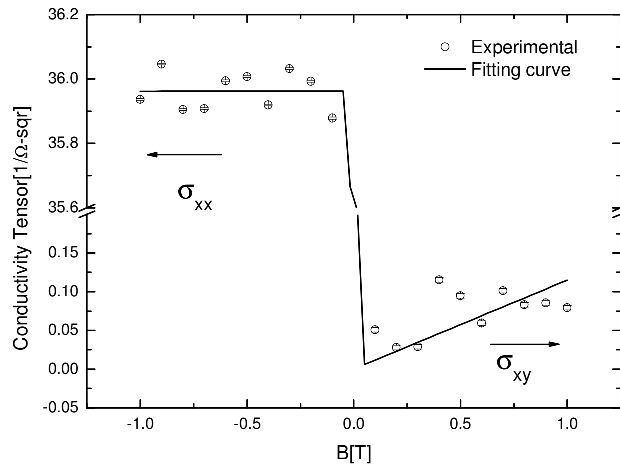

Fig.6.37: The conductivity tensor for P type silicon wafer.

University of Cape Town

***N type wafer*:** This was also supplied by Siltronix GA, Germany. According to the specification from the supplier the resistivity of this wafer is greater than 300 Ωcm, which we experimentally determined to be about 25 kΩcm. It is a phosphorous doped material with a thickness between 250 and 300 μm. For analysis purposes we assumed its thickness to be 275 μm. From the resistivity measurement it can be inferred that this material is lightly doped. A sample with Van der Pauw geometry was prepared from this wafer with dimensions of approximately 1 cm x 1 cm x 0.275 mm. A variable field Hall effect measurement was conducted on the sample and the result was fitted to the combined conductivity tensor as shown in Fig. 6.38.

Table 6.13: summary of the result for the N type silicon wafer.

Carrier Type	Carrier density [m^{-3}]	Mobility [m^2/V-s]
Hole	(2.61 ± 0.54) x 10^{17}	0.067 ± 0.009
Electron	(3.6 ± 1.0) x 10^{16}	0.198 ± 0.023

From table 6.13 we observe that two carriers do exist with comparable concentrations. Even if the hole concentration appears to be higher than that of the electrons, their mobility is much lower. Over the magnetic field interval used for the measurement, the carriers with higher mobility, in this case electrons dominate and the material will exhibit N-type conductivity.

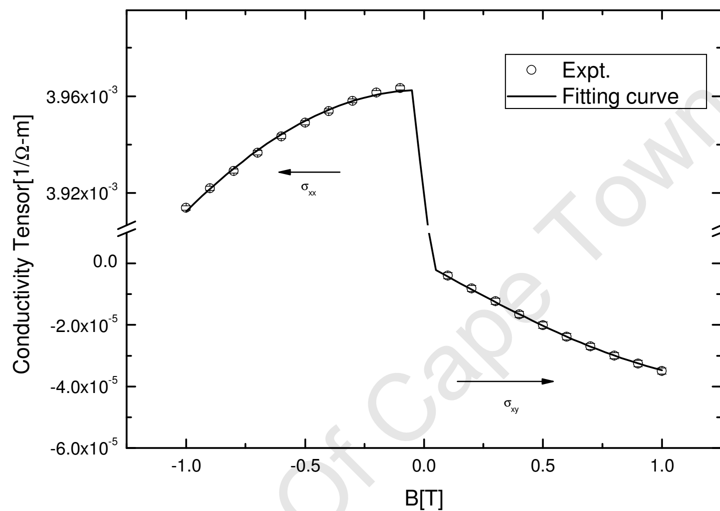

Fig.6.38: Two carrier fitting for N-type silicon wafer

When the result is fitted to a single carrier type, the carriers are determined to be electrons with density of (2.577 ± 0.03) x 10^{18} m^{-3}, with a mobility of (9.55 ± 0.13) x 10^{-3} m^2/V-s. This result is consistent with the average value obtained from the Hall effect measurement using the standard software.

M-si granule: A chunk of metallurgical silicon with fairly rectangular shape was used for variable field measurement. The same fitting procedure was conducted to the experimental results. We have applied one carrier and two carrier models to fit the data. The best fit result is for a two carrier model which indicates the presence of two hole carriers but with different concentration and mobilities as summarized in table 6.14.

University Of Cape Town

Table 6.14: Carriers in the M-si granule.

Carrier Type	Sheet carrier density [m^{-2}]	Mobility [m^2/V-s]
Hole-1	$(4.12 \pm 0.04) \times 10^{21}$	$(2.90 \pm 0.03) \times 10^{-3}$
Hole-2	$(6.57 \pm 0.56) \times 10^{14}$	67 ± 41

The second carrier has a mobility which is very high, but with a concentration which is much lower than the dominant carrier. The second carrier may not necessarily be attributable to silicon since this material is unintentionally highly doped with various impurities.

6.5.3 Compressed powders

The pellets: The three pellets produced and characterized had an average diameter of about 8 mm and thickness of 1mm. The distances between the metal contact tips were also about 1 mm. All the samples satisfy conditions for the Van der Pauw geometry and the measurement was performed accordingly. The data from each sample was fitted to the combined conductivity tensor for single and multicarrier models. The parameters extracted from the fitting are as tabulated in table 6.15.

Table 6.15: Summary of electrical parameters from pellets.

Pellet	carrier Type	Sheet carrier density [m^{-2}]	Mobility [m^2/V-s]
P	electron	$(1.079 \pm 0.001) \times 10^{18}$	$(1.673 \pm 0.001) \times 10^{-5}$
	hole	1.99×10^{13}	7.38×10^{-5}
N	electron	$(3.14 \pm 0.02) \times 10^{16}$	$(1.17 \pm 0.01) \times 10^{-4}$
	hole	2.40×10^{14}	3.54×10^{-6}
P883	electron	$(1.08 \pm 0.02) \times 10^{14}$	$(9.97 \pm 0.05) \times 10^{-2}$
	hole	$(2.23 \pm 0.02) \times 10^{15}$	$(2.18 \pm 0.01) \times 10^{-2}$

University Of Cape Town

From the results the existence of the second carrier can be noted even if its contribution to the overall properties of the sample is not significant. The response of the N and P883 pellets was as expected, maintaining their dominant carrier type. But pellet P, showed a completely opposite carrier type with the holes as minority carriers.

6.6 Field dependent studies of screen printed layers

For this work screen printing of samples has merits and demerits. The merits are that the technique helped us to produce reliable and reproducible samples. The demerits of the technique are that oil based inks are not screen printable. The main problem encountered was ink instability. As a result acrylic based inks were the only usable option. Consequently salt doped silicon inks were not considered at this stage.

In the field dependent studies, there are contributions from the powder, binder, solvent, the environment and the substrate. Therefore it is imperative to apply the magnetoresistivity/conductivity technique to study the electrical properties of such complex materials. This helped to determine and subtract the contribution coming from background. The dominant background contribution is assumed to come from the paper substrates. The analysis which was conducted on paper substrate showed that, in dry condition, it contributes electrons as carriers with sheet carrier density of ($3.66 \times 10^{10} \pm 1.28 \times 10^{9}$) m^{-2} with a mobility of (0.009 ± 0.001) m^2/V-s. This value was taken as a background correction factor for all the subsequent measurement of silicon layers printed on paper substrate. Therefore all the results that are extracted from the fitting represent the composite system of silicon powder and binder.

The data points in the variable field measurement were an important factor to decide the number of carrier types for the fitting or to define the parameters.

University of Cape Town

Including the paper, at least two carrier types were obtained for most of the samples. In those samples for which the third carriers were determined, their concentration was too low to make a meaningful contribution. Only a few fitted curves will be presented here, whereas the rest will be presented in **Appendix E**. The results are summarized and presented in table 6.16, where N_1 and N_2 are sheet carrier concentrations and μ_1 and μ_2 are their corresponding mobilities.

Table 6.16: summary of the results from samples with Marchem acrylic binder.

Average Quantity for sheet quantity	P- Layers	N- Layers
$N_1(m^{-2})$	$(7.37 \pm 2.44) \times 10^{12}$	$(4.18 \pm 1.92) \times 10^{12}$
$N_2(m^{-2})$	$(2.24 \pm 2.24) \times 10^{8}$	$(2.51 \pm 2.51) \times 10^{7}$
$\mu_1(m^2/V\text{-}s)$	$(2.38 \pm 0.90) \times 10^{-3}$	$(3.33 \pm 0.95) \times 10^{-3}$
$\mu_2(m^2/V\text{-}s)$	4.13 ± 0.63	3.85 ± 1.06

When compared with the result from either the wafers or from the pellets, the carrier concentration dropped significantly because there is a constricted current path, in the sense since that the layer is formed through a network of individual silicon particles of irregular shapes. Among other factors, the flow of current is controlled by the effective contact area between the particles. The carrier types for both P- and N-type samples turned out to be holes, which was unexpected for the N-type material. This sign reversal may be attributed to either the reaction between the Marchem acrylic ink and silicon, or impurities in the silicon. In relative terms, however, comparing the result from the P-and N-type material, the N-type is more N-type, since its hole density is lower than the P-type material. In both cases the contribution of the second carrier is small.

University Of Cape Town

7 Discussion

Synthesis and characterization of nanoparticulate silicon for device applications were the main objectives of this work. Silicon nanoparticles were obtained from different sources: from commercial suppliers and produced in house. The application of high energy milling was one of the successes achieved for easy and mass production of silicon nanopowder.

As outlined in the introduction, the ultimate objective is to mass produce working electronic devices by applying print technology. The production of printable ink from inorganic semiconductor material can also be regarded as a success achieved during the course of this work. The ink formulation and printability were first tested with hand printing on the working substrates. Later these inks were applied to screen printing in which it was established that generally hand printable inks were not screen printable. The oil based inks, for example, were good for hand printing but were unstable when applied to screen printing. Ink separation and screen blockage were the major challenges with oil based ink. While experimenting to achieve screen printable inks, a significant number of samples were characterized that were produced manually. Eventually applying acrylic emulsion as a binder enabled us to establish a screen printable ink. But certain features of the experiment which were possible with oil based ink were not possible with acrylic based ink. This was noticed for doping silicon with inorganic salts. Maybe because of the possible chemical reaction between the salt and the components of the ink, or the interaction between the surfactants and the particles, the doping experiment was not successful with acrylic based ink. Since screen printing ensures the production of reliable and reproducible samples, the focus was given to the material characterization, halting the doping experiments, until the appropriate ink formulation is attained.

University of Cape Town

From the synthesis of the nanopowder for milled silicon, the average particle or cluster size was determined to be above 100nm. This size is relatively large according to the standard definition “nano” in nanoscience and technology. But such intermediate size has its own merit in that the powder exhibits the properties of its bulk counterpart. Unique behaviours which are attributed to quantum effects (e.g. quantum confinement) will not be a problem with particles in this size range. Besides, particles with such sizes can form printable inks for screen printing and other methods such as ink jet.

TEM micrographs were used to determine the particle size distribution, which is described by a lognormal distribution. From the lognormal fitting the average sizes of the powder were determined to vary between 130 and 160 nm for milled powders. Even for the intrinsic silicon, the average size was around 51 nm. Our expectation of these materials was therefore that they would not respond differently to their bulk counterparts.

University Of Cape Town

X-ray diffraction measurements conducted on all powders revealed that the crystallite size is of the order of tens of nanometers. Scherrer’s method was applied to the (111) peak to determine the crystallite sizes. For the intrinsic silicon it was determined as (26.24 ± 0.03) nm, whereas for metallurgical silicon milled for 180 minutes it was (30.59 ± 0.07) nm. The FWHM of the first peak was observed to increase with milling time. An inverse relation between the crystallite size and the FWHM, means that longer milling time results in smaller crystallite sizes. The impact the particle sustains during the milling process resulted in structural deformation at the microscopic level. As a result lattice relaxation was observed with milling time with an approximate change in lattice spacing of 0.05% after 5 Hrs milling.

From the SAXS measurement the radius of gyration, which is a measure of crystallite size, yielded the same order of magnitude as the result determined

from XRD via Scherrer's method. When compared, the crystallite sizes determined from the XRD and SAXS measurements, are smaller than the average particle sizes determined from TEM. This can be explained by the particles being polycrystalline, supporting the result obtained from electron and X-ray diffraction.

The results from different techniques, Raman spectroscopy and XRD measurement, showed that the materials remained crystalline after milling. This was further confirmed by electron diffraction. In X-ray diffraction the silicon oxide phase was not clearly observed, except possibly for a weak intensity in particles milled for short times, observed around $2\theta=23^{o}$. Raman spectroscopy was applied to study other powders in addition to those studied with XRD. These were powders produced by low energy milling. The Raman spectra of the two sets of powder had different characterstics. Firstly fluorescence, which was observed in low energy milled powders, was not observed in high energy milled powders. Secondly the low frequency band which was observed in the high energy milled powder was not seen in the low energy milled powders. For the low energy milled powder the oxygen content seems to increase with milling time, but such a trend was not observed for high energy milled powder. Different phases of silicon oxides such as coesite, stishovite and tridymite were observed. In powders produced with both zirconia and steel milling media, a stishovite phase accompanied the fluorescence, which suggests the formation of thick oxide layers. The trend was that fluorescence increases with milling time implying the formation of thicker oxide. In high energy milled powders a coesite-like phase was observed, with little or no fluorescence. This suggests the formation of a thin or no oxide layer. Coesite, as a first step in the process of oxidation, typically occurs in the first 2-5 nm [1]. The absence of optical phenomena which compete with the free movement of charge in the high energy milled powder is a bonus for the electrical performance of devices produced from such powders. As a result powder from high energy milling is the material of choice for device applications.

University of Cape Town

In general the observed oxide phases of silicon are formed at high pressure or/and temperature, suggesting that the rise in internal temperature accompanied by high impact energy could contribute to their formation.

The printed layers were characterized for their surface profile, network formation between particles and their electrical properties. In the process of ink formulation the introduction of binders was deliberate, to achieve a particle-particle interconnection and particle-substrate adhesion. The micrographs from scanning electron microscopy result showed the clustering of the particles and further clustering of clusters. It was hoped to verify this effect with SAXS measurements, but unfortunately the q range available did not allow this. However, information on the shape and size of the particles, which was consistent with what has been determined by other techniques, was determined. The intrinsic silicon was determined to be more homogeneous in shape than the milled powders. This was learned from the calculated polydispersivity index (PDI). Beaucage's unified theory was applied for the SAXS analysis and compared with the result from GNOM package for free standing layers. Similar results were obtained from both techniques, and further analysis was carried out only with the unified method.

University of Cape Town

Electrical characterization mainly utilized Hall effect measurements. The effect of doping silicon with inorganic salts was studied with a home built Hall measurement system using hand printed layers. Changes in the electrical properties were observed for the salt-silicon composite. To discuss the mechanism of the doping effect it would be appropriate to revisit the term doping in a chemical context. The doping here is different to the usual definition in Semiconductor Physics (Chapter 2) in which atomic replacement takes place. Here doping refers to a surface phenomenon on the silicon particle. There are two possible models which explain the possible cause for the change of carrier type as the salt is introduced, both of which involve the charge balance on the whole particle. In the first model, a cation is adsorbed to the surface of the silicon

particle which was initially neutral. In the process the particle loses an electron to the adsorbing cation or gains a free hole. The process is demonstrated in Fig.7.1.

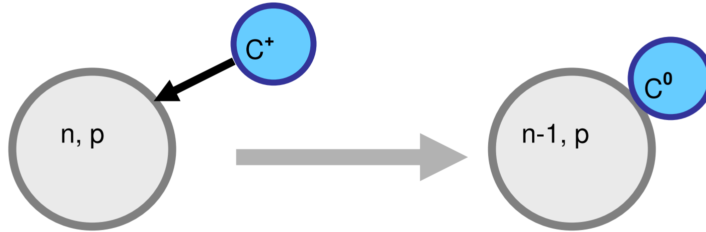

Fig.7.1: A cation is adsorbed on the particle and neutralised thereby gaining an electron. Hence the particle loses an electron or gains a free hole.

University Of Cape Town

The second model could be explained in terms of the anions. As demonstrated in Fig.7.2, an anion is adsorbed on the particle while maintaining its charge. This causes charge build up which prompts the particle to lose its excess charge to a spectator cation. The cation gains an electron which comes from the particle and hence the particle gains free hole.

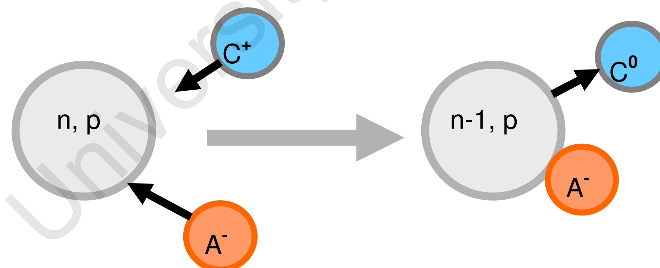

Fig.7.2: Anion adsorbing on the surface of the particle with a spectator cation. While maintaining the charge balance, the silicon particles gain a free hole.

The micrographs of Fig.7.3 show elemental mapping of 10% NaCl doped intrinsic silicon using a 120 keV TEM. Figure 7.3 a) shows the standard TEM image of the silicon, whereas Fig.7.3 b) is the elemental map of the chlorine. As can be seen clearly, chlorine is adsorbed onto the silicon nanoparticles avoiding the

surrounding matrix. This is consistent with the second model presented above to explain the process of carrier type reversal. Anions are adsorbed onto the particle while maintaining their charge state. But from the principle of conservation of charge, the particles must have opposite charge to the adsorbed ions, and hence become P-type.

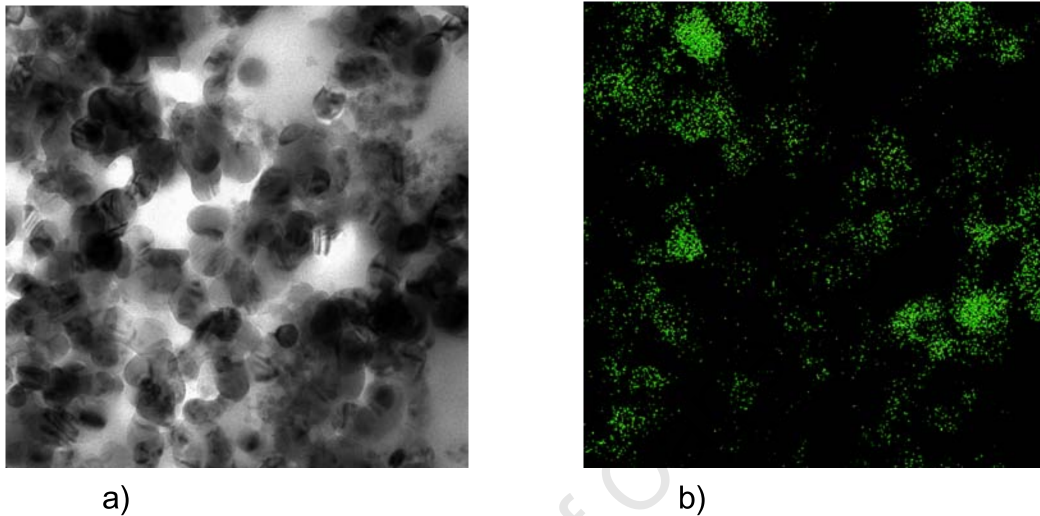

a) b)

Fig.7.3: a) TEM image of i-Si doped with 10%NaCl, b) Elemental map of the distribution of Cl.

University Of C

With the acrylic based ink, which was basically formulated for the screen printing, doping was not possible. For layers produced with acrylic binder, sign reversal of the Hall effect for N-type silicon was observed. The possible explanation for this may be due to the reaction that takes place between the acrylic binder and the active material. The data sheet of the binder indicates the presence of phosphate ions, which may result in unintentional doping causing the dominant carrier type to be reversed from N-type to P-type. However, if we compare the densities of each carrier type, the N-type material remains relatively N-type (less P-type) compared to the P-type material. The surfactant and ingredients in the acrylic of screen printable silicon ink possibly react with the dopant salt. As a result, apart from the printability of the ink, the sign reversal observed, deterred the idea of doping silicon ink with acrylic binder.

Characterization of hand printed layers from all types of silicon ink with the home built Hall effect system produced results in which the carrier type was maintained for each material. The intrinsic silicon responded as if it was an N-type material with electrons as majority carriers. In principle for an intrinsic material equal numbers of electrons and hole are expected. Due to the fact that electrons are more mobile than holes, they dominate and the material behaves as if it is N-type. In all cases the sheet resistivity was very high which influenced the Hall voltage and thereby influencing the determination of the Hall mobility. The high resistivity is observed because of the low particle packing density. It is only possible for the current to follow a percolation path between points. The contribution of defects from grain boundaries may also contribute to the resistivity as defect sites are known as traps of free carriers.

The results from field dependent Hall effect measurements indicated the existence of multicarrier transport in the printed layers. Different sources can contribute to the different carriers observed. While it is possible for the silicon alone to exhibit multiple carriers, the contributions from the other ink ingredients and the substrate cannot be ruled out. The results for silicon wafers, both P and N, showed them to have both holes and electrons as carriers. The N-type sample which was lightly doped was demonstrated to have a larger hole concentration than electrons, but the mobility for the holes (0.0671 m^2/Vs) is considerably smaller than for the electrons (0.1983 m^2/Vs). As a result electrons dominate and influence the Hall coefficient to acquire negative sign. The values of mobility are with in acceptable range for silicon that spans between 0.05 and 0.005 m^2/Vs for holes and between 0.15 and 0.009 m^2/Vs for electrons [2] depending on dopant level [3]. Similarly for P-type material, the mobility value for the majority hole carrier is with in the accepted interval. For the second carriers, electrons, the mobility was too small to influence the Hall coefficient. Consequently the sign of Hall coefficient is determined by the dominant hole carriers.

University of Cape Town

For the metallurgical granule due to the presence of grain boundaries, there is a formation of band bending that significantly reduces carrier mobility and traps which reduce carrier concentration. The carrier mean free path in comparison with the grain size also affects the mobility. The analysis for this sample revealed the presence of two types of hole carriers. The mobility for the dominant component is (2.90 ± 0.03) x 10^{-3} m^2/Vs, which is an acceptable value for polycrystalline silicon [4]. As discussed in chapter 3.5, the transport mechanism in disordered systems is not fully understood. Hence one should be careful in considering these values as drift mobilities. However they do give good indication because particles are large enough for drift inside single particle.

The result for the compressed powders and the printed layers are different from the wafers and the granules as powder is involved. XRD, SAXS and Raman spectroscopy proved that the individual particles are polycrystalline. Apart from the description given above for grain boundaries, other factors are present which influence the carrier density and mobility. The main factor is the particle density for which charge mobility is determined under the principle of percolation theory. Others are the way the particles form a network, and the contact area between particles that apparently depends on the shapes of the particles. Hence the influences come from grain-grain and particle-particle contacts. In all cases the best fit to data was determined for the two carrier model, with of course one dominant carrier type. The mobility for the N-type powder was (1.17 ± 0.01) x 10^{-4} m^2/Vs which is less than that of polycrystalline silicon. Likewise in the P-type pellet the mobility corresponding to the dominant carrier type was (1.673 ± 0.001) x 10^{-5} m^2/Vs. The P883 pellet manifested a mobility for the dominant carrier type as 2.18 ± 0.01) x 10^{-2} m^2/Vs. This mobility is close to the single crystalline value which may indicate that the particles in P883 powder are single crystalline. The carrier concentration for the printed layers was lower than for the pellets which may be attributed to the particle packing density - less dense means less carrier density. When additionally an insulating binder is included in the composite, there

University of Cape Town

is a possibility to create spatially distributed conducting islands (particles or clusters) in an insulating medium between which hopping is the possible means for charge transfer. Under such charge transport the anomalous Hall effect can be observed. Although in the printed layers a low carrier concentration was obtained, the dominant carrier mobility was between 0.2 and 0.3 m^2/Vs, which is comparable or better than the mobility of some organic semiconductors [5].

Both the impedance analysis and simple IV measurement showed the presence of a capacitive component in device structures. The origin of the capacitive effective can be explained the following way. When two such particles come in contact or close proximity, they will form a particle-insulator-particle structure, which is identical to a simple capacitor structure that is observed in the electrical measurement. But for a given device there are thousands and thousands of such structures making series and parallel networks, with the electrical measurement revealing the resultant value. A thin oxide layer may also contribute to the capacitive property as would any point contact between conducting particles. The non ohmic but symmetric IV characteristic curve, Fig. 6.31, also shows the presence of capacitance for which, at low operating voltage, charge transport is dominated by an inverse charge accumulation current. As the applied voltage increases in magnitude the charge is accumulated until it breaks down and for any further increase in applied voltage the current increases rapidly. From the impedance measurement, three resistors and two capacitors values determined for each of the structures. As the Cole-Cole plot was independent of the bias voltage direction these capacitors are likely to be interfacial capacitances and not a depletion layer. Their formation is at the interface between metal and particle and between particles. Two resistors accompany capacitors whereas the third resistor represents the contact resistance to the device. The presence of capacitors increases the resistivity and also limits the mobility.

University of Cape Town

In all cases the mobility for these materials is comparable to amorphous silicon and conducting polymers. Hence there is a prospect for device application by improving the carrier concentration which can be achieved by improving the particle packing density. The choice of binder material may be also a factor to be investigated further to improve the electrical responses.

University Of Cape Town

8 Conclusions

As stated at the outset, the main objective of this work was to develop simple techniques to produce and characterise materials for electronic and optoelectronic applications. This was successfully achieved during the course of this study. For this purpose nanoparticulate silicon powder was produced from different sources using different methods. Structural studies using XRD and electron diffraction verified that milled the powders remained crystalline. TEM observations indicated that the particle size distribution is lognormal with a median size of about 150 nm, whereas XRD, using Scherrer's method, confirmed a crystallite size of about 40 nm, reducing with milling time. Comparing these results it is obvious that the milled silicon nanoparticles are polycrystalline, as indicated by electron diffraction. The same trends were observed from SAXS analysis.

For the first time, we have formulated printable semiconducting inks from nanoparticulate silicon. Oil based inks were applicable for manual printing, whereas acrylic inks can generally be used for all kinds of printing. Electrical characterisation with a home built system revealed that particles milled from P- and N-type silicon retained their carrier type in oil-based inks but with a drastic reduction in carrier concentration. This result can be attributed to percolation transport through a loose particle network.

Doping nanoparticulate silicon with inorganic salts was successfully demonstrated, with a complete reversal of carrier type. Intrinsic silicon, which is nominally an N-type material, exhibited P-type behaviour after adding salts to it. The effect was observed with both sodium chloride and magnesium chloride. Sodium chloride, which is less hygroscopic than magnesium chloride, was found to be the better material for doping. Sodium chloride was then used to dope metallurgical silicon to form a PN diode. Unintentional doping was also observed

University Of Cape Town

with acrylic based inks, but detailed experiments could not be performed because of the adverse effect of doping on the stability of the acrylic emulsion. More work with regard to the ink chemistry is needed to be able to accurately control the doping level in acrylic based inks.

A combined model to simultaneously fit the transverse and longitudinal components of magnetoconductivity tensor was developed and applied successfully. This is a general model that can be used to study materials with single or multiplecarrier types. The model was used study changes in the electrical properties of silicon in different forms throughout the production process: as wafers, compressed powders and printed layers. The majority carrier type was maintained in most cases except for screen printed layers of acrylic inks containing N-type material. The mobilities of charge carriers in the printed layers were comparable with amorphous silicon and organic semiconductors, even though the carrier density was low. Future work needs to concentrate on improving the number of percolation paths by increasing the packing density of the particles in the final printed layer.

More information on the interparticle connections were obtained from IV and impedance spectroscopy measurements which demonstrated the capacitive effects present in the printed layers. The simplest equivalent circuit was found to be a series connection of two parallel RC elements and a series resistance. The two capacitors originate at the interface between the metal and the layers, and between the particles. The absence of thick oxide layers around high energy milled silicon nanoparticles, as proven by Raman spectroscopy, makes this contact capacitance small, presenting an opportunity to use it for device applications such as solar cells and transistors. Currently functional devices such as transistors [1] and solar cells [2] are being developed.

University of Cape Town

References

Chapter 1

[1] F.E. Kruis, A. Goossens, H. Fissan, *J. Aerosol Sci.* **27** (1996) 165

[2] S. Tamir, S. Berger, *Appl. Surf. Sci.* **86** (1995) 514

[3] S.V.N.T. Kuchibhatla, A.S. Karakoti, D. Bera , S. Seal, *Prog. in Mater. Sci.* **52** (2007) 699

[4] M. Härting, J. Zhang, D.R. Gamota, D.T. Britton, *Appl. Phys. Lett.* **94** (2009) 193509

[5] D.T. Britton, M. Härting , *Pure & Appl. Chem.* **78** (2006) 1723

Chapter 2

[1] H. Shirakawa, *Synthetic Metals* **69** (1995) 3

[2] J.D. Patterson, B.C. Bailey, *Solid State Physics: Introduction to the theory*, Springer, Berlin, 2007

[3] I.I. Hanna, E.H. Sondheimer, *Proc. R. Soc. London A* **239** (1957) 247

[4] J. Orton, *The Story of Semiconductors*, Oxford University Press, New York, 2004

[5] S.M. Sze, *Physics of Semiconductor Devices* 2nd edition, Willey, New York, 1981

[6] K. Seeger, *Semiconductor Physics An Introduction*, 6th edition, Springer, Berlin, 1997

[7] C.J. Tung, R.H. Ritchie, *Phys. Rev.* B **16** (1977) 4302

[8] D. Shoenberg, in *Electrons at the Fermi Surface in Solid State Science: Past, Present and Predicted* (edited by D. L Weaire, C. G. Windsor), Adam Hilger, Bristol, 1987

[9] C. Kittel, *Introduction to Solid State Physics*, 8th edition, Wiley, Massachusets, 2005

University of Cape Town

[10] T. Wenckebach, *Essentials of Semiconductor Physics*, Wiley, Chichester, 1999

[11] D. Kondo, K. Sakamoto, M. Shima, W. Takeyama, K. Nakamura, K. Ono, Y. Kasukabe, M. Oshima, *Phys. Rev.* B **70** (2004) 233314

[12] A. Goetzberger, J. Knobloch, B. Voss, *Crystalline Silicon Solar Cells*, Wiley, Chichester, 1998

[13] H. Eren, *Wireless Sensors and Instruments*, CRC Press, Boca Raton, 2006

[14] M.R. Scriba, C. Arendse, M. Härting, D.T. Britton, *Thin Solid Films* **516** (2008) 844

[15] B. Fickett, G. Mihalik, *J. Cryst. Growth* **225** (2001) 580

[16] R. Tsu, J.C. Lofgren, *J. Cryst. Growth* **227-228** (2001) 21

[17] K. Fujiwara, Y. Obinata, T. Ujihara, N. Usami, G. Sazaki, K. Nakajima, *J. Cryst. Growth* **266** (2004) 441

[18] S.S. Talukdar, M.T. Swihart, *Aerosol Sci.* **35** (2004) 889

[19] N.W. Ashcroft and N.D. Mermin, *Solid State Physics*, Holt, Rinehart and Winston, New York, 1976

[20] C.J. Philips, *Phys. Rev.* **125** (1962) 1931

[21] B. Bouhafs, H. Aourag, *Solid State Comm*. **96** (1995) 245

[22] J. Singleton, *Band Theory and Electronic Properties of Solids*, Oxford University Press, New York, 2001

[23] B.G. Streetman, Solid State Electronic Devices, 4th edition, Prentice Hall, New Jersey, 1995

[24] B.V. Zeghbroeck, http://ecee.colorado.edu/~bart/book/book/chapter2/ch2_6.htm, accessed 6 Aug.2009

[25] R.A. Street, *Hydrogenated amorphous silicon*, Cambridge University Press, New York, 1991

[26] K. Tanaka, E. Maruma, T. Shimada, H. Okamoto, *Amorphous Silicon*, Wiley, Chichester, 1999

University of Cape Town

[27] M.F. Thorpe, D. Weaire, *Phys. Rev. Lett.* **27** (1971) 1581

[28] D. Weaire, M.F. Thorpe, *Phys. Rev*. B **4** (1971) 2508

[29] W.A. Harrison, *Pure & Appl. Chem.* **61** (1989) 2161

[30] M.F. Thorpe, D. Weaire, R. Alben, *Phys. Rev.* B **7** (1973) 3777

[31] D.A. Drabold, J. Dong, *J. Non- Cryst. Solids* **227-230** (1998) 153

[32] N.F. Mott, E.A. Davis, *Electronic Processes in Non-Crystalline Materials*, 2nd edition, Clarendon Press, Oxford, 1979

[33] S. Halindintwali, PhD Thesis, University of the Western Cape, 2005

[34] C.Q. Sun, *Prog. in Solid State Chem.* **35** (2007) 1

[35] Z. Zhong, C. Yang, C. M. Lieber, in *Nanosilicon*, edited by V. Kumar, Elsevier, London, 2007

[36] D.L. Staebler, C.R. Wronski, *Appl. Phys. Lett.* **31** (1977) 292

[37] P. Kumar, F. Zhu, A. Madan, *Int. J. Hydrogen Energy* **33** (2008) 3938

[38] A. Madan, *Surface & Coat. Technol.* **200** (2005) 1907

[39] C.H. Lee, A. Sazonov, A. Nathan, *Appl. Phys. Lett.* **86** (2005) 22106

[40] A.D. Yoffee, *Adv. in Phys.* **42** (1993) 173

[41] D.S. English, L.E. Pell, Z. Yu, P.F. Barbara, B.A. Korgel, *Nano Letters,* **2** (2002) 681

[42] M.A. Pinault, J. Barjon, T. Kociniewski, F. Jomard, J. Chevallier, *Physica* B, **401-402** (2007) 51

[43] D.C. Look, D.C. Reynolds, C.W. Litton, R.L. Jones, D.B. Eason, G. Cantwell, *Appl. Phys. Lett*. **81** (2002) 1830

[44] S.M. Sze, K.K. Ng, *Physics of Semiconductor Devices*, 3rd edition, Wiley, New Jersey, 2007

[45] D.A. Fraser, *The Physics of Semiconductor Devices, Oxford University* Press, Oxford, 1977

[46] L. Solymar, D. Walsh, *Electrical Properties of Materials, 6th edition*, Oxford University Press, Oxford, 1998

[47] U.K. Mishra, J. Singh, *Semiconductor Device Physics and Design,* Springer, Dordrecht, 2008

University of Cape Town

Chapter 3

[1] S.M. Sze, Kwok K. NG, *Physics of semiconductor Devices*, 3rd edition, Wiley, New Jersey, 2007

[2] B.G. Streetman, Solid State Electronic Devices, 4th edition, Prentice-Hall, New Jersey, 1995

[3] D.A. Neamen, *Semiconductor Physics and Devices: Basic Principles*, 3rd edition, Mc Graw Hill, New York, 2003

[4] J. Singleton, *Band Theory and Electronic Properties of Solids*, Oxford University Press, New York, 2001

[5] M. Balkanski, R.F. Wallis, *Semiconductor Physics and Applications*, Oxford University Press, New York, 2000

[6] C. Kittle, *Introduction to Solid State Physics*, 8th edition, Wiley, Massachusetts, 2005

[7] K. Seeger, *Semiconductor Physics, An Introduction*, 6th edition, Springer-Verlag, Berlin, 1997

[8] P.W. Anderson, *Phys. Rev.* **109** (1958) 1492

[9] N. Mott, *Rep. Prog. Phys*. **47** (1984) 909

[10] H.C. Kang, *J. Non-Cryst. Solids* **261** (2000) 169

[11] N. Mott, M. Pepper, S. Pollitt, R.H. Wallis, C.J. Adkins, *Proc. R. Soc. London* A **345** (1975) 169

[12] B.I. Halperin, J.S. Langer, *Phys. Rev.* B **4** (1971) 2612

[13] N.F. Mott and E. A. Davis, *Electronic Processes in Noncrystalline Materials*, 2nd edition Clarendon Press, Oxford, 1979

[14] P.G. Le Comber, W.E. Spear, *Phys. Rev. Lett*. **25** (1970) 509

[15] C. Godet, J.P. Kleider, *J. Mater. Sci.: Mater. Electron.* **17** (2006) 413

[16] N. Mott, *Conduction in Non-Crystalline Materials*, 2nd edition, Oxford University Press, New York, 1993

[17] P. Sheng, *Phys. Rev*. B **21**(1980) 2180

University Of Cape Town

[18] S. Washburn, R.A. Webb, *Rep. Prog. Phys.* **55** (1992) 1311

[19] Y. Yi , PhD Thesis, Georgia Institute of Technology, 2004

[20] N. Agrait, A.L. Yeyati, J.M. van Ruitenbeek, *Phys. Rep*. s **377** (2003) 81

[21] T. Ando, H. Matsumura, T. Nakanishi, *Physica* B **323** (2002) 44

[22] E.H. Hall, *Amer. J. Math.* **2** (1879) 287

[23] Lakeshore 7500/9500 Series Hall System User's Manual, Lakeshore Cryotronics Inc

[24] D.C. Look, *Electrical characterization of GaAs Materials and Devices*, Wiley, New York, 1989

[25] T. Bronger, R. Carius, *Thin Solid Films* **515** (2007) 7486

[26] L.J. van der Pauw, *Philips Res. Repts*. **20** (1958) 220

[27] S.S. Li, *Semiconductor Physical Electronics*, 2nd edition, Springer, New York, 2006

[28] T. Plackowski, M. Matusiak, *Supercond. Sci. Technol*. **12** (1999) 610

[29] E.H. Putley, *The Hall Effect and Related Phenomena*, Butterworths, London, 1960

[30] G.Y. Logvenov, M. Hartmann, R.P. Huebener, *Phys. Rev*. B **46** (1992) 11102

[31] R. Fletcher, A.J. Friedman, M.J. Stott, *J. Phys. F: Metal Phys*. **2** (1972) 729

[32] L.J. van der Pauw, *Philips Res. Reports* **13** (1958) 1

[33] P. Blood, J.W. Orton, *Rep. Prog. Phys.* **41** (1978) 11

[34] D.K. Schroder, *Semiconductor Material and Device Characterization*, 3rd edition, Wiley, New Jersey, 2006

[35] Y. Sun, J. Shi, Q. Meng, *Semicond. Sci. Technol*. **11** (1996) 805

[36] R.A. Street, *Hydrogenated Amorphous Silicon*, Cambridge University Press, New York, 1991

[37] W.A. Beck, J.R. Anderson, *J. Appl. Phys*. **62** (1987) 541

[38] D.L. Leslie-Pelecky, D.G. Seiler, M.R. Loloee, *Appl. Phys. Lett*. **51** (1987) 1916

University Of Cape Town

[39] J. Lindemuth, B. Dodrill, J. Meyer and I. Vurgaftman, Extended Abstract of a paper presented at CS-MAX, San Jose, CA, November 11-13, IOP publishing Ltd. 2002

[40] A.C. Beer, Solid State Physics, Suppl. 4, *Galvanomagnetic Effects in Semiconductors*, edited by F. Seitz and D. Turnbull, Academic Press, New York, 1963

[41] J.R. Meyer, C.A. Hoffman, F.J. Bartolit, D.A. Arnold, S. Sivananthan J.P. Faurie, *Semicond. Sci. Technol*. **8** (1993) 805.

[42] G. Du, J. R. Lindemuth, B.C. Dodrill, R. Sandhu, M. Wojtowicz, M.S. Goosky, I. Vurgaftman, J.R. Meyer, *Characterizing Multi-Carrier Devices with Qualitative Mobility Spectrum Analysis,* http://www.lakeshore.com/pdf_files/systems/Hall_Data_Sheets/IPRM%20Paper.pdf, accessed on 02 April 2009

[43] J.S. Kim, D.G. Seiler, W.F. Tseng, *J. Appl. Phys*. **73** (1993) 8324

[44] J.S. Kim, D.G. Seiler , J.R. Ehrstein . *J. Appl. Phys*. **80** (1996) 4425

[45] J.S. Kim, D.G. Seiler, L. Colombo, M.C. Chenz, *Semicond. Sci. Technol*. **9** (1994) 1696

[46] J.M. Holender, G.J. Morgan, *Phil. Mag.* **35** (1992) 225

[47] L. Friedman, *J. Non-Cryst. Solids* **6** (1971) 329

[48] J. Singh, *J. Mater. Sci.: Materials in Electronics* **14** (2003) 689

[49] N.F. Mott, *Phil. Mag.* B **63** (1991) 3

[50] J.Y.W. Seto, *J. Appl. Phys*. **46** (1975) 5247

[51] C.R.M. Grovenor, *J. Phys. C: Solid State Phys*. **18** (1985) 4079

[52] W.E. Taylor, N.H. Odell, H.Y. Fan*, Phys. Rev*. **88** (1952) 867

[53] J.W. Orton, M.J. Powell, *Rep. Prog. Phys.* **43** (1980) 1263

[54] T. Weis, R. Lipperheide, U. Wille, *J. appl. Phys.* **92** (2002) 1411

[55] Y. Nasuno, M. Kondo, A. Matsuda, *J. Appl. Phys.* **78** (2001) 2330

[56] X.Y. Chen, W.Z. Shen, Y.L. He, *J. Appl. Phys.* **97** (2005) 024305

[57] P.S. Clarke, J.W. Orton, A.J. Guest, *Phys. Rev.* B **18** (1978) 1813

University of Cape Town

[58] E. M. Purcell, *Electricity and Magnetism, Berkeley Physics Course*, Vol. 2, 2nd edition, McGraw-Hill, Massachusetts,1985

[59] E. Barsoukov, J.R. Macdonald, *Impedance Spectroscopy Theory, Experiment, and Applications*, John Wiley and Sons, New Jersey, 2005

[60] H. De Waard, D. Lazarus, *Modern Electronics*, Addison-Wesley, Massachusetts, 1966

[61] K.S. Cole, R.H. Cole, *J. Chem. Phys.* **9** (1941) 341

[62] K. Prabakar, S.K. Narayandass, D. Mangalaraj, *Mater. Sci. & Eng.* B **98** (2003) 225

[63] C.K. Alexander, M.N. O. Sadiku, *Fundamentals of Electric Circuits*, 3rd edition, Mc Graw-Hill, 2005

Chapter 4

[1] C.C. Koch, *Dekkar Encyclopedia of Nanoscience and Nanotechnology*, Marcel Dekkar, New York, 2004

[2] M.S. El-Eskandarany, *Mechanical Alloying for Fabrication of Advanced Engineering Materials*, William Andrew Publisher, New York, 2001

[3] P.R. Soni, *Mechanical Alloying*, Cambridge International Science Publishing, Cambridge, 2001

[4] D.T. Britton, M. Härting, *Pure & Appl. Chem.* **78** (2006) 1723

[5] C.L. De Castro, B.S. Mitchell, Synthesis, *Functionalization and Surface Treatment of Nanoparticles*, Edited by M. –I. Baraton, American Scientific Publishers, 2002

[6] C. Suryanarayana, *Mechanical Alloying and Milling*, Marcel Dekker, New York, 2004

[7] C.C. Koch, *Rev. Adv. Mater. Sci*. **5** (2003) 91

[8] C. Suryanarayana, *Prog. In Mater. Sci*. **46** (2001) 1

[9] www.orange32.com, accessed on 26 Dec. 2008

University of Cape Town

[10] G. Lengwiler, www.silkscreenhistory.com, accessed on 26 Dec. 2008

[11] J. Savage, *The deposition Process-Equipment*, in Handbook of Thick Film Technology, edited by, P.J. Holmes and R.G. Loasby, Electrochemical Publications, Ayr, 1976

[12] Gwent Electronic Materials, www.g-e-m.com/index.html, accessed 15 June 2009

[13] G.T. -Munizaga , G.V.B. –Canovas, *J. Food Engineering* **67** (2005) 147

[14] M.A. Rao, *Rheology of Fluid and Semisolid Foods, Principles and Applications*, Aspen Publisher, Maryland, 1999

[15] A.Ya. Malkin, *Rheology Fundamentals*, ChemTec, Ontario, 1994

[16] R. Tahery, H. Modarress, J. Satherley, *Chemical Engineering Science* **60** (2005) 4935

[17] A.R. Henn, *Biophysical Chem.* **105** (2003) 533

[18] H. Tavana, A.W. Neumann, *Adv. in Colloid and Interface Sci.***132** (2007) 1

[19] C.N.C. Lam, R. Wu, D. Li, M.L. Hair, A.W. Neumann, *Adv. in Colloid and Interface Sci.* **69** (2002) 169

[20] T. Bronger, R. Carius, *Thin Solid Films* 515 (2007) 7486

Chapter 5

[1] M.J. Buerger, *X-Ray Crystallography*, Wiley, New York, 1958

[2] B.D. Cullity, *Elements of X-ray diffraction*, Addison-Wesley, Reading, Massachusetts 1956

[3] P. Coppens, *X-ray Charge Densities and Chemical Bonding*, Oxford University Press, New York, 1997

[4] N.W. Ashcroft, N.D. Mermin, *Solid State Physics*, Harcourt, Orlando, 1976

[5] A. Guinier, *The Rigaku Journal* **16** (1999) 1

[6] M. Lambert, *Acta. Cryst.* A **57** (2001) 1

[7] D.W. Schaefer, K.D. Keefer, *Phys. Rev. Lett.* **56** (1986) 2199

University of Cape Town

[8] P.W. Schmidt, *J. Appl. Cryst*. **24** (1991) 414

[9] C. Riekel, *Nucl. Inst. and Mater. in Phys. Research* B **199** (2003) 106

[10] Y. Wang, T. Kamiyama, K. Suzuki, *Mater. Sci. & Eng.* A **217/218** (1996) 94

[11] G. Porod, in *Small Angle X-ray Scattering* (edited by O. Glatter, O. Kratky), Academy Press, London, 1982

[12] A. Guinier, G Fournet, *Small-Angle Scattering of X-rays*, Wiley, New York, 1955

[13] E. Gianotti, G. Berlier, K. Costabello, S. Coluccia, F. Meneau, *Catalysis Today* **126** (2007) 203

[14] G. Beaucage*, http://www.eng.uc.edu /~gbeaucag/Classes/Analysis/ Chapter8.pdf,* accessed on 30 Nov 2008

[15] P.R. Laity, R.E Cameron, *Powder Technology* **188** (2008) 119

[16] D.W. Schaefer, *Science* **243** (1989) 1023

[17] D.W. Schaefer, B. C. Bunker, J. P. Wilcoxon, J. S. Rowlinson, R. C Ball, D. J. Tildeseley. *Proc. R. Soc. London A* **423** (1989) 35

[18] G. Beaucage, *J. Appl. Cryst.* **28** (1995) 717

[19] G. Beaucage, H.K. Kammaler, S.E. Pratsinis. *J. Appl. Cryst.* **37** (2004) 523

[20] Brazilian National Laboratory of Synchrotron Light, www.lnls.br , accessed on 20 July 2008

[21] H.C.N. Tolentino, A.Y. Ramos, M.C.M. Alves, R.A. Barrea, E. Tamura, J.C. Cezar, N. Watanabe, *J. Synchrotron Rad.* **8** (2001) 1040

[22] I. Polikarpov, G. Oliva, E.E. Castellano, R.C. Garratt, P. Arruda, A. Leite, A. Craievich, *Nucl. Inst. & Meth.* A **405** (1998) 159

[23] A.F. Craievich, *Mater. Research* **5** (2002) 1

[24] A.S. Zarghani, S.F.K. Bozorg, A.Z. Hanzaki, *Mater. Sci. & Eng. A* **500** (2009) 84

[25] G.F. Roomans, A. Dragomir, *Electron Microscopy methods and Protocols*, 2nd edition, edited by J. Kuno, Human Press, New Jersey, 2007

University of Cape Town

[26] J.I. Goldstein, D.E. Newbury, P. Echlin, D.C. Joy, A.D. Roming, Jr., C. Fiori, E. Lifshin, *Scanning Electron Microscope and X-ray Microanalysis*, 2nd edition, Plenum Press, New York, 1992

[27] D.C. Joy, in *Electron Microscopy: Principles and Fundamentals* (edited by S. Amelickx D. van Dyck, J. van Lauduyl, G. van Tendeloo), VCH, Weinheim, 1997

[28] R.F. Egerton, Physical Principles of Electron Microscopy: An introduction to TEM, SEM and AEM, Springer, New York, 2005

[29] Leica Stereoscan S440i SEM Operation Manual

[30] Transmission Electron Microscope Leo 912 OMEGA Operation Manual

[31] S. Amelickx, in *Electron Microscopy: Principles and Fundamentals* (edited by S. Amelickx D. van Dyck, J. van Lauduyl, G. van Tendeloo), VCH, Weinheim 1997

[32] P.W. Hawkes, E. Kasper, *Principles of Electron Optics*, Vol.1, Academic Press, London, 1989

[33] P.J. Goodhew, F.J. Hamphreys, *Electron microscopy and Analysis*, 2nd edition, Taylor & Francis, London, 1988

[34] C.V. Raman, K.S. Krishnan, *Nature* **121** (1928) 501

[35] J.R. Baena, B. Lendl, *Current Opinion in Chem. Bio.* **8** (2004) 534

[36] W.R. Browne, J.J. McGarvey, *Coordination Chem. Rev.* **251** (2007) 454

[37] E. Smith, G. Dent, *Modern Raman Spectroscopy: A practical Approach*, Wiley, Chichester, 2005

[38] K.J. Laidler, J.H. Meiser, B.C. Sanctuary, *Physical Chemistry*, 4th edition, Houghton Mifflin, Boston, 2003

[39] N.B. Colthup, L.H. Daly, S.E. Wiberley, *Introduction to Infrared and Raman Spectroscopy*, 3rd edition, Academic Press, Boston, 1990

[40] R.L. Frost, *Spectrochemica Acta* Part A **71** (2009) 1788

[41] M.O. Carl, R. Krupke, *Phys. Rev. Lett*. **100** (2008) 127401

[42] R. L. McCreery, Raman Spectroscopy for Chemical Analysis, Wiley, New York, 2000

University of Cape Town

[43] Operation manual advantage 532 Raman Spectroscopy
[44] A. Finnemore, BSc Honours Project, University of Cape Town, 2007
[45] HMS operation manual, Lakeshore Cryotronics Inc
[46] HP 4192A LF Impedance Analyzer Manual, Hewlett Packard, Tokyo, 1986

Chapter 6

[1] Digimize image analysis software, www.digimizer.com accessed on 20 Sep.2008
[2] J.H. Parker,Jr., D.W. Feldman, M. Ashkin, *Phys. Rev*. **155** (1967) 712
[3] Z. Iqbal, S. Veprek, *J. Phys*. C **15** (1982) 377
[4] RRUFF Database, www.rruff.info accessed 12 Oct. 2008
[5] A. El Goresy, L Dubrovinsky, T.G. Sharp, M. Chen, *J. Physics and Chem. of Solids* **65** (2004) 1597
[6] F.L. Galeener, R.A. Barrio, E. Martinez, R.J. Elliott, *Phys. Rev. lett.* **53** (1984) 2429
[7] B. Boizot, S. Agnello, B. Reynard, R. Boscaino, G. Petite, J*. Non-Cryst. Solids* **325** (2003) 22
[8] G. Beaucage, *Phys. Rev*. E **70** (2004) 031401
[9] G. Beaucage, H. K. Kammler, S.E. Pratsinis, *J. Appl. Cryst.* **37** (2004) 527
[10] D.T. Britton, E.A. Odo, G. Goro Gonfa, E.O. Jonah, M. Härting, *J. Appl. Cryst.* **42** (2009) 448
[11] D.I. Svergun. A. Semenyuk, GNOM small angle scattering data analysis software, http://www.embl-hamburg.de/ExternalInfo/Research/Sax/gnom.html
[12] Hind. A. Ahmed, Postgraduate Diploma Project, African Institute of Mathematical Sciences, 2006
[13] D.T. Britton, M. Harting, *Pure & Appl. Chem.* **78** (2006) 1723
[14] J. Lindemuth, Lakeshor Cryotronics Inc, private communication

University Of Cape Town

[15] A. Rose, *Phys. Rev.* **97** (1955) 1538

[16] D. Johnson, Scribner Associates, Inc.

[17] J.S. Kim, D.G. Seiler, W.F. Tseng, *J. Appl. Phys.* **73** (1993) 8324

[18] M.R. Scriba, D.T. Britton, C. Aredendse, M.J. van Staden, M Härting, *Thin Solid Films* 517 (2009) 3484

Chapter7

[1] H. Hwang, P. Chen, J. Lin, *Chinese J. Physics* **30** (1992) 899

[2] S.M. Sze, K.K. Ng, *Physics of Semiconductor Devices 3rd edition*, Wiley, New Jersey, 2007.

[3] J.W. Orton, M.J. Powell, *Rep. Prog. Phys.* **43** (1980) 81

[4] W.C. Ya, L.X. Dong, Z.S. Yun, L. Juan, M.Z. Guo, X.S. Zhen, Z. Fang, *Chinese Phys.* B **18** (2009) 1237

[5] H.E. Katz, *J. Mater. Chem.* **7** (1997) 369

Chapter 8

[1] M. Härting, J. Zhang, D.R. Gamota, D.T. Britton, *Appl. Phys. Lett*. **94** (2009) 193509

[2] D.T. Britton, M. Härting , *Pure & Appl. Chem.* **78** (2006) 1723

University Of Cape Town

Appendices

A: The measurement steps for Van der Pauw structure.

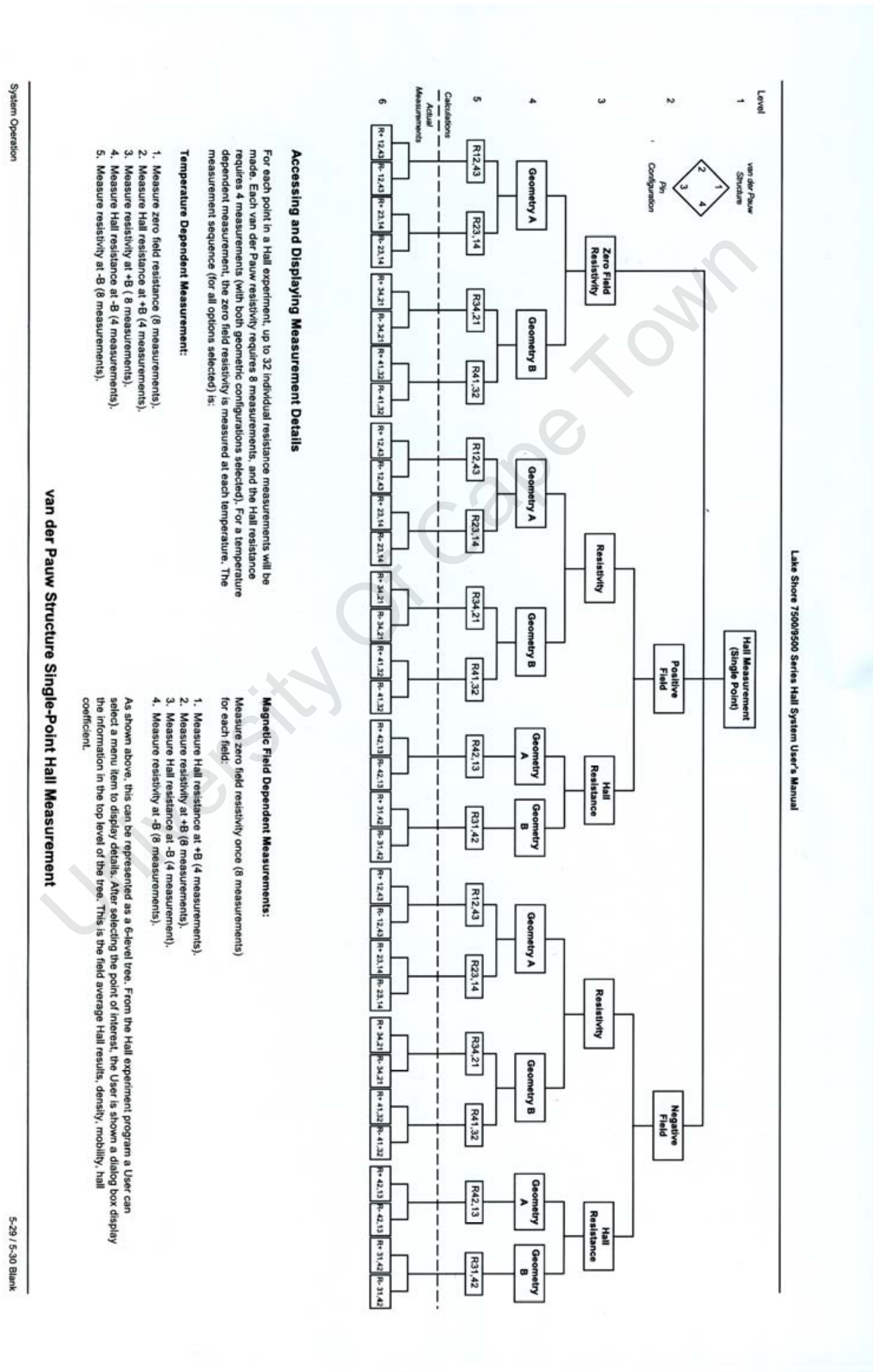

Accessing and Displaying Measurement Details

For each point in a Hall experiment, up to 32 individual resistance measurements will be made. Each van der Pauw resistivity requires 8 measurements, and the Hall resistance requires 4 measurements (with both geometric configurations selected). For a temperature dependent measurement, the zero field resistivity is measured at each temperature. The measurement sequence (for all options selected) is:

Temperature Dependent Measurement:

1. Measure zero field resistance (8 measurements).
2. Measure Hall resistance at +B (4 measurements).
3. Measure resistivity at +B (8 measurements).
4. Measure Hall resistance at -B (4 measurements).
5. Measure resistivity at -B (8 measurements).

Magnetic Field Dependent Measurements:

Measure zero field resistivity once (8 measurements) for each field:

1. Measure Hall resistance at +B (4 measurements).
2. Measure resistivity at +B (8 measurements).
3. Measure Hall resistance at -B (4 measurement).
4. Measure resistivity at -B (8 measurements).

As shown above, this can be represented as a 6-level tree. From the Hall experiment program a User can select a menu item to display details. After selecting the point of interest, the User is shown a dialog box display the information in the top level of the tree. This is the field average Hall results, density, mobility, hall coefficient.

van der Pauw Structure Single-Point Hall Measurement

University of Cape Town

B: The magnetoconductivity tensor fitting equation

```
y=1.602E-19/2*((1-erf(x/0.01))*(sqrt(N1^2)*M1/(1+M1*M1*x^2)+sqrt(N2^2)*M2/(1+M2*M2*x^2)+sqrt(N3^2)*M3/(1+M3*M3*x^2))+(1+erf(x/0.01))*x*(N1*M1*M1/(1+M1*M1*x^2)+N2*M2*M2/(1+M2*M2*x^2)+N3*M3*M3/(1+M3*M3*x^2)))
```

C: Raman shift for Silicon oxide families

silicon oxide	**peak position(1/cm)**
melanophlogit	179
quartz	213
melanophlogit	225.49
melanophlogit	273.72
opal	313.68
coesite	326.87
quartz	356.81
tridymite	357
melanophlogit	364.47
quartz	395.1
tridymite	402
cristobalite	418.51
tridymite	420
opal	425.48
coesite	428.57
melanophlogit	439.39
tridymite	450
coesite	466.31
quartz	467.23
opal	486.48
coesite	522.23
opal	550.51
stishovite	587

University of Cape Town

melanophlogit	599
quartz	697.56
melanophlogit	729.94
stishovite	749
opal	782.76
tridymite	783
cristobalite	784.87
coesite	790
melanophlogit	807.63
tridymite	830
coesite	840
melanophlogit	894.78
stishovite	961
opal	962.3
melanophlogit	977.06
coesite	1040
coesite	1075
tridymite	1075
cristobalite	1075.1
opal	1076.2
melanophlogit	1107.66
quartz	1162.9
coesite	1170
melanophlogit	1183.34
cristobalite	1212.2
melanophlogit	1239.29

University Of Cape Town

D: IV measurement for M silicon

I IV for M si linseed oil & chloroform

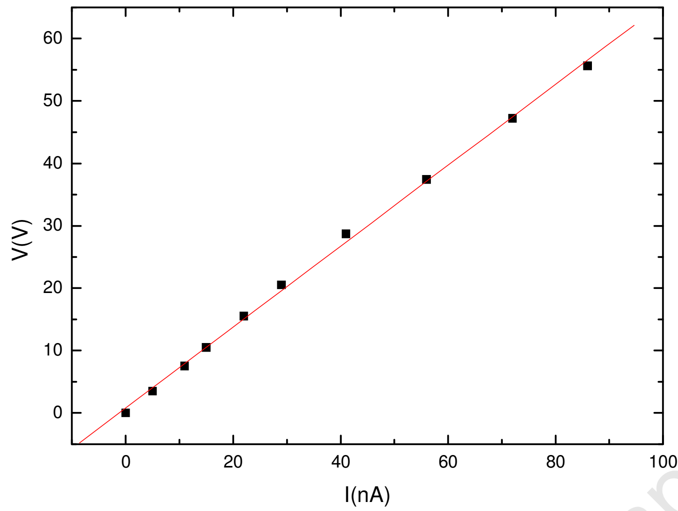

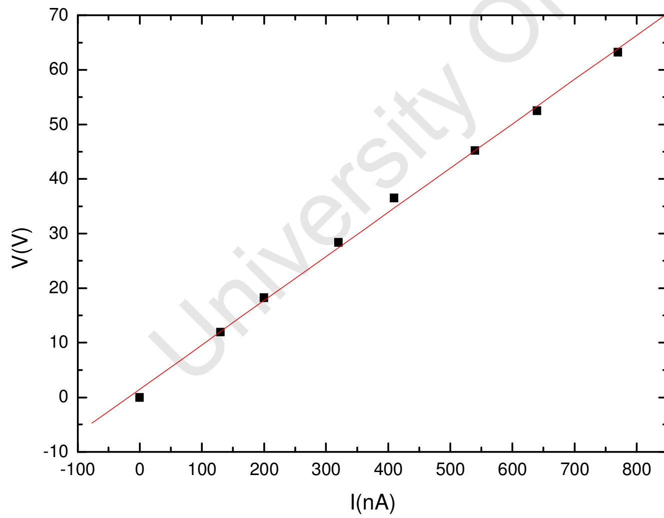

University Of Cape Town

II IV for M-Si in linseed oil and chloroform (2%NaCl)

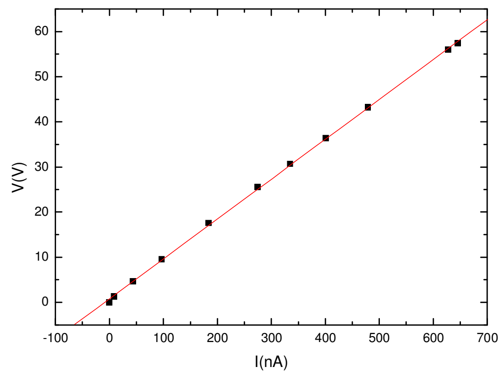

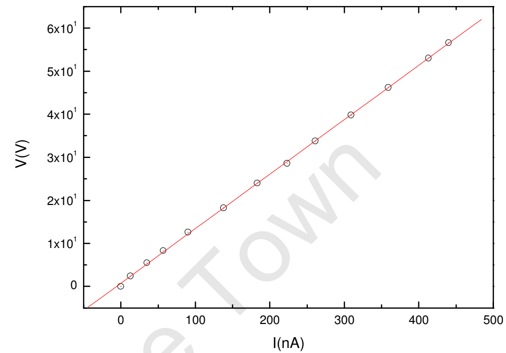

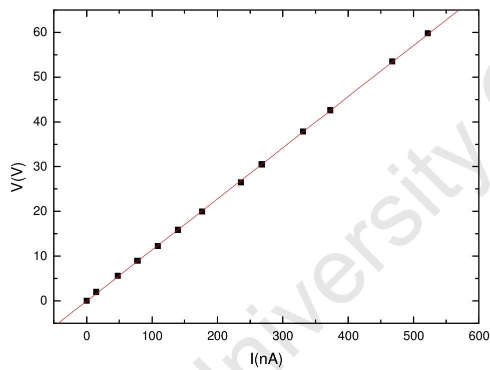

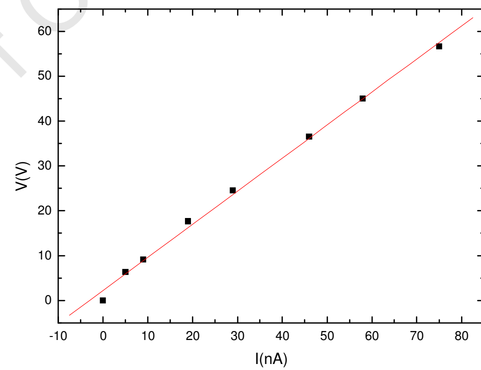

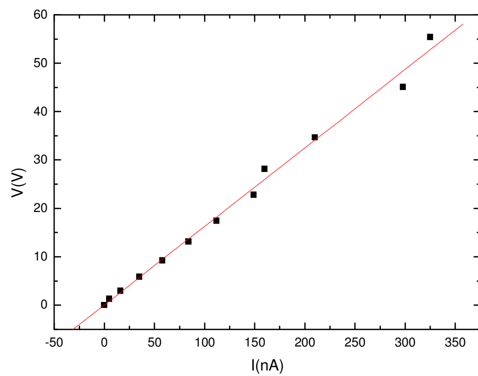

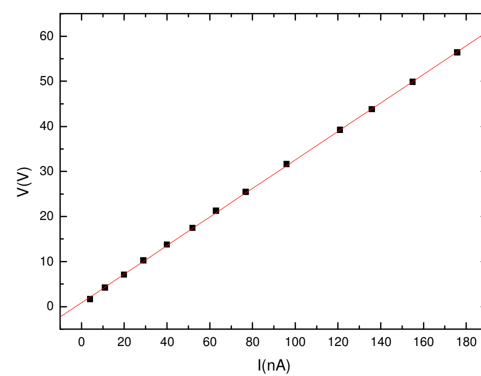

University Of Cape Town

III IV for M-Si in linseed oil and Chloroform

6%NaCl

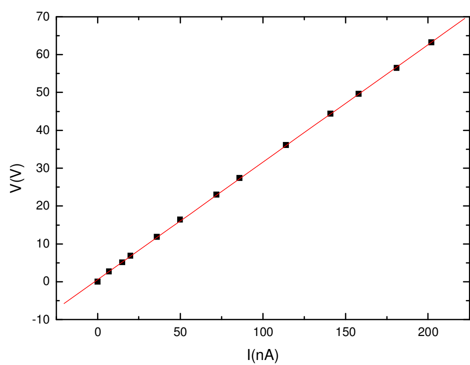

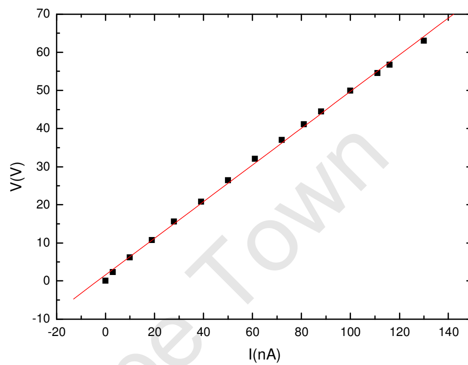

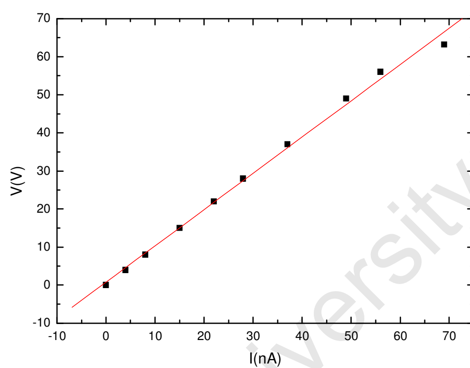

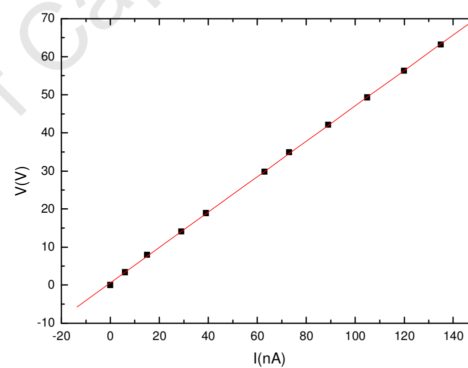

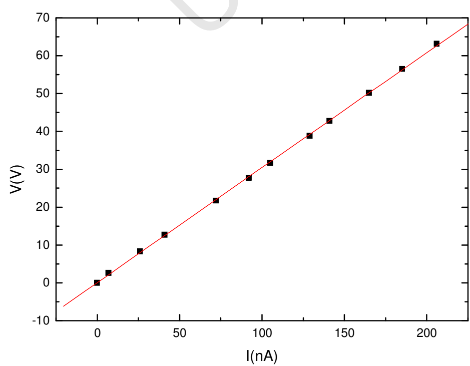

University Of Cape Town

IV IV for M-si in linseed oil and chloroform

8%NaCl

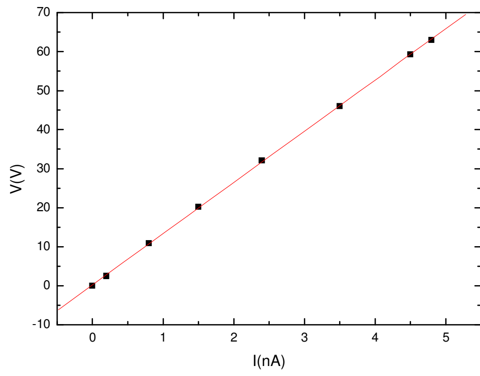

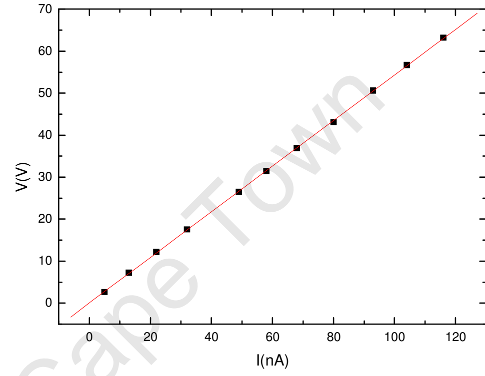

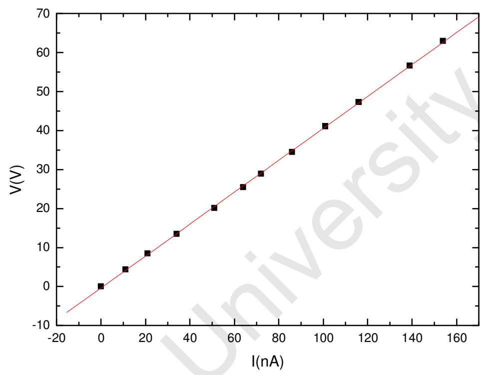

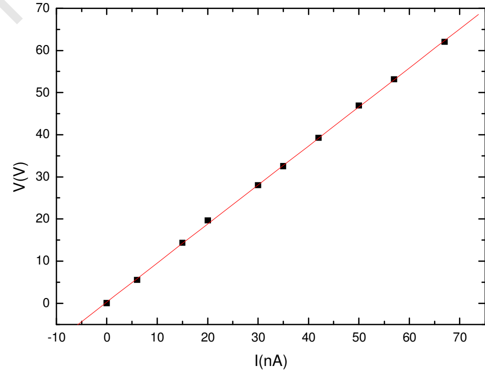

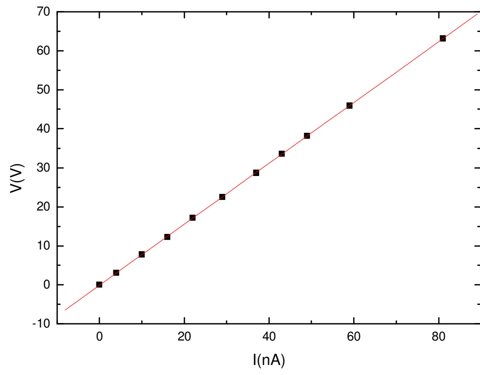

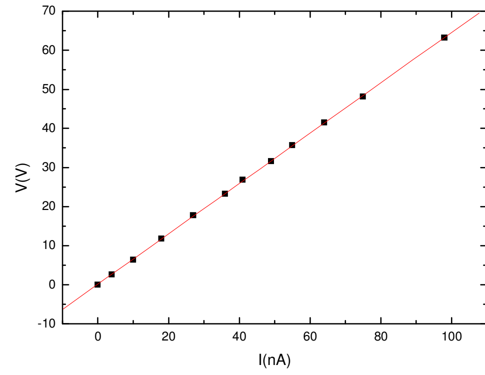

University Of Cape Town

V IV for M-Si in linseed oil and chloroform

10%NaCl

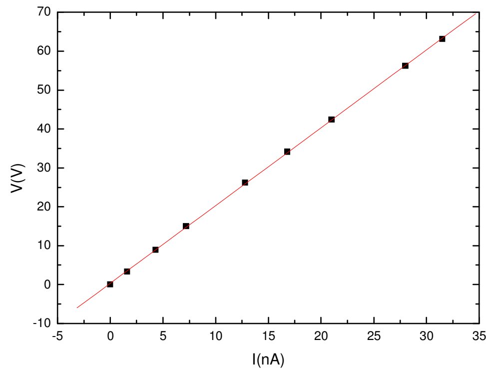

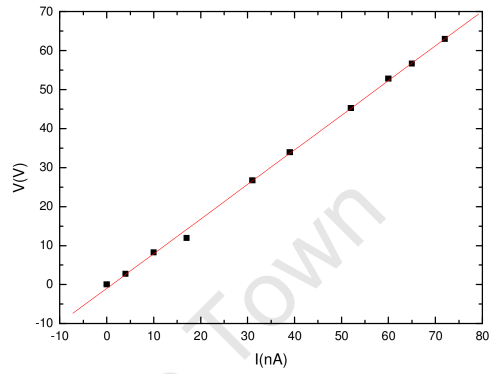

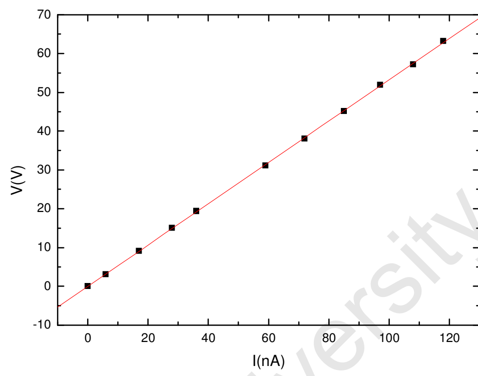

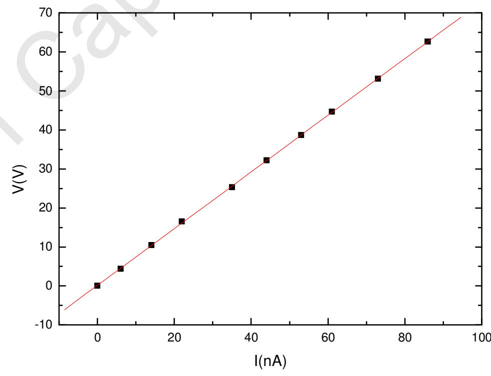

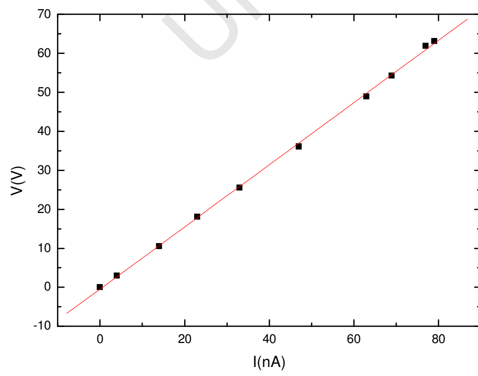

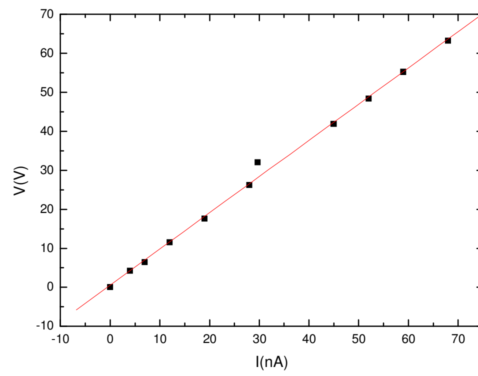

University of Cape Town

E: Few curves for conductivity tensor fit. Solid line is the fit whereas the points are experimental values.

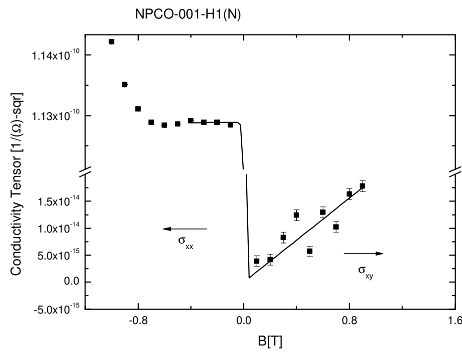

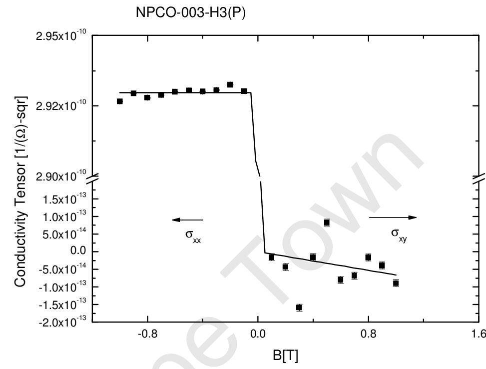

University Of Cape Town

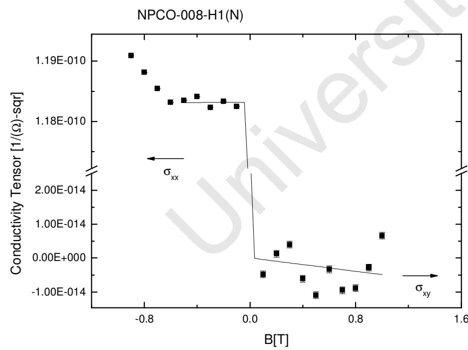

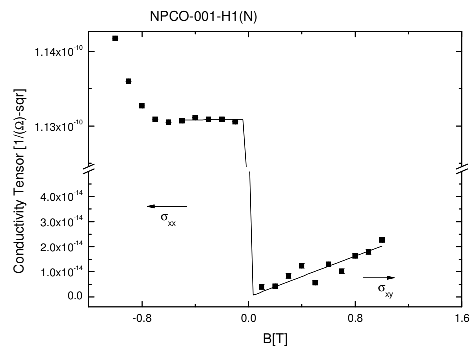

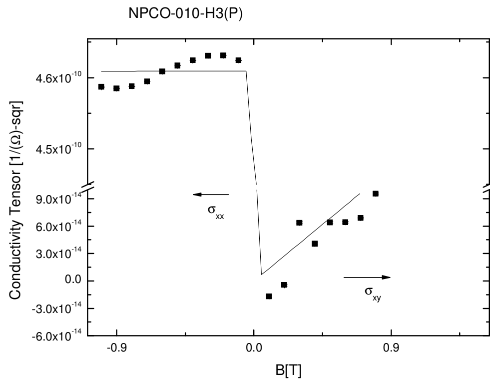

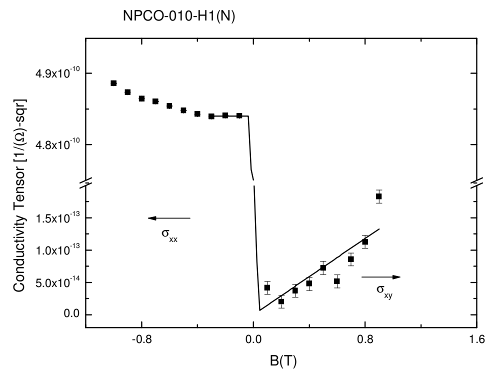

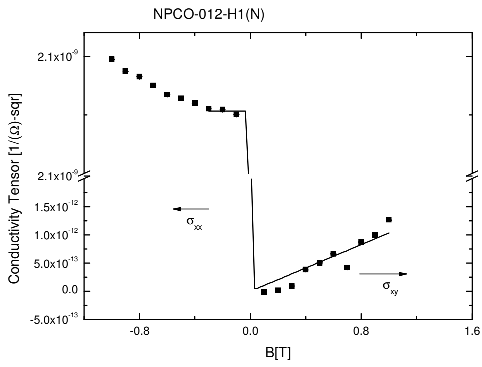

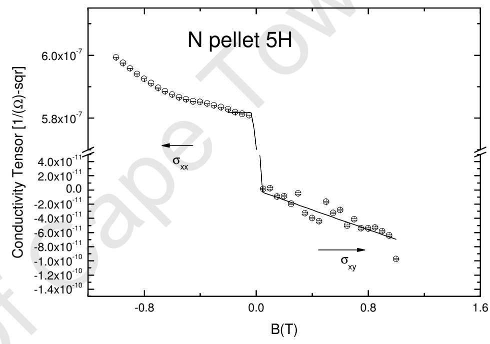

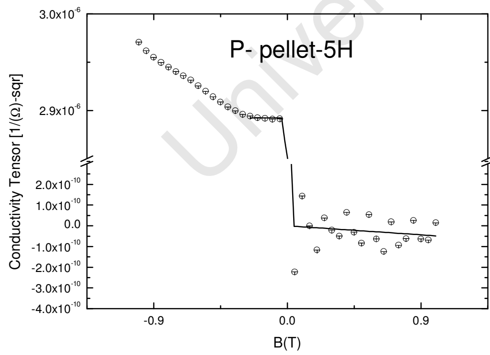

University Of Cape Town